ABSTRACT

Title of Dissertation:	APPLICATIONS OF INTENSE MID-INFRARED LASER-PLASMA INTERACTIONS
	Daniel Capson Woodbury, Doctor of Philosophy, 2020
Dissertation directed by:	Professor Howard Milchberg, Department of Physics

Intense laser-plasma interaction, generally characterized by focused laser intensities exceeding ~1 TW/cm^2, is a major pillar of plasma physics and nonlinear optics with broad applications, including high energy charged particle and photon sources, the generation and study of high energy density physics conditions, fusion energy sources, remote detection techniques, and self-guided nonlinear propagation. For many important applications, longer wavelength lasers provide favorable scaling for laser-plasma interactions, and in several cases enable entirely new phenomena. In this dissertation we present experimental and computational results for three laser-plasma-based applications using ultrashort mid-infrared (mid-IR or MIR) and long-wave-infrared (LWIR) laser pulses. In the first laser wakefield acceleration (LWFA) experiment at mid-IR wavelengths, we demonstrate acceleration of electron bunches driven by relativistic self-focusing collapse of mid-IR laser pulses in near-critical

density gas jet targets, and compare scaling of bunch charge and energy to those from common near-infrared systems. Second, we demonstrate that single-electron-seeded avalanche breakdown driven by picosecond mid-IR lasers is an ultrasensitive technique for measuring extremely low plasma densities in gases. We use this technique in two applications. First, we first demonstrate standoff detection of radioactive materials, with avalanche measurements enabling determination of source location and estimates of the radioactivity level. We then use the technique to measure ionization yield induced by an auxiliary laser in atmospheric pressure range gases over 14 orders of magnitude, a record range achievable with no other technique we are aware of. Finally, we present theory and simulations of nonlinear propagation of high power MIR and LWIR multi-picosecond pulses in air, demonstrating that self-guided propagation at moderate intensity is mediated by an ensemble of discrete avalanche plasmas seeded by aerosols.

APPLICATIONS OF INTENSE MID-INFRARED LASER-PLASMA INTERACTIONS

by

Daniel Capson Woodbury

Dissertation submitted to the Faculty of the Graduate School of the
University of Maryland, College Park, in partial fulfillment
of the requirements for the degree of
Doctor of Philosophy
2020

Advisory Committee:
Professor Howard Milchberg, Chair
Professor Ki-Yong Kim
Professor Phillip Sprangle
Professor Adil Hassam
Dr. Jared Wahlstrand

Dedication

For Tonya.

Acknowledgements

I first gratefully acknowledge Professor Howard Milchberg, who has helped me become a better researcher and writer, even if it took several rounds of mistakes and revisions to get there. Howard's incredible dedication passion for physics has driven the impressive research capability in our lab, but he has also fostered a supportive environment for his students and my family. I would also like to thank Professor Scott Bergeson, for providing excellent undergraduate mentorship, and introducing me to both optics and basic plasma physics.

I'd like to thank all of the students I have worked with over the course of this work. In particular, Robert Schwartz has persevered through difficult and sometimes confusing experiments while working around my constrained schedule, and Linus Feder put blood, sweat, tears, a 10-day hospital stay and a double cast into our work in Vienna. I also thank Andrew Goffin, Ela Rockafellow, Anastasia Korolov, Bo Miao, and Fatholah Salehi for their contributions to my work. Andrew Goers and George Hine were incredibly helpful when I started out in the lab, and were always willing to give advice and direction. I have also enjoyed many discussions and helpful hints (and borrowed optics) from Sina Zahedpour, Ilia Larkin, and Scott Hancock, and look forward to work that Matthew Le, Jaron Shrock and Lucas Railing will add to our group. Jared Wahlstrand was a great help in my studies on ionization, as well as early experiments on avalanche. I'm indebted to Josh Isaacs and his adviser, Phil Sprangle, for their work on avalanche simulations, and for helping me articulate unique approaches to picosecond avalanches and their effect on propagation.

During the past five years, I've also had many opportunities to collaborate with researchers from other labs on several rewarding experiments. I thank Valentina

Shumakova and Claudia Gollner for their hard work in making the LWFA experiment at TU Wien a success and teaching me about the OPCPA system, as well as Audrius Pugzlys, Ignas Astrauskas and Andrius Baltuska for extensive help installing the laser. I also thank Jinpu Lin and John Nees; Ki-Yong Kim and Dogeun Jang; and Jennifer Elle and Alexander Englesbe.

I am deeply indebted to the Krell Institute and its staff, and the many opportunities afforded me through the DOE NNSA SSGF fellowship. I have benefited immensely from the program and its annual review, and look forward to giving back. I would also like to thank Adam Harvey-Thompson, Chris Jennings, Jeff Fein, Matthias Geissel, and Kyle Peterson at Sandia National Laboratories for support and direction during internships, and helping to guide me towards research in laser plasma interactions and high energy density physics.

Throughout my program, I have been grateful for support from many friends in the area, particularly J. T. Wiser, Bryan Hardy, and Wade Jacobsen and their families, who provided fellowship at church and, at times, sorely needed babysitting.

And finally; I cannot express here how incredibly grateful I am for my family. Work on experiments over the past 5 years has been alternately stressful, intriguing, disappointing, and exhilarating, and it has required a lot not only of me, but also of them and their time. Chloe and Maya help me remember many joys of life, including the joy of learning things for the very first time. Finishing the dissertation was always going to be a difficult task, but I never could have expected a worldwide emergency, shuttered daycares, simultaneous work from home schedules, and a remote defense: I would not have been able to do it without Tonya. We did it!

This work was supported by the Department of Energy National Nuclear Security Administration Stewardship Science Graduate Fellowship program, which is provided under grant number DENA0003864.

Table of Contents

List of Figures

Chapter 1: Introduction

1.1 Motivation and outline of the dissertation

Intense laser matter interactions, under one definition, can be characterized by laser electric fields and accelerated charged particle energies which are of the same order as atomic fields in bound systems, or fields which lead to nonlinear responses of free electrons and ions in unbound systems. Equating the quiver energy of an electron or proton in a focused laser field with either atomic potentials (~10 eV) or the particle's rest mass (~500 keV or ~1 GeV) defines relevant intensities over an extremely broad range from 10^{12}-10^{22} W/cm^2 for optical and infrared (λ=0.4-10 μm) laser wavelengths. These intensities, in turn, span a wide range of applications such as low order harmonic generation [1], filamentation and supercontinuum generation [2,3], high field THz [4-6], RF [7] and high harmonic generation [8], laser-plasma sources from extreme ultraviolet (EUV) to gamma rays [9-12], creation and characterization of high-energy density (HED) states of matter [13-15], and acceleration of charged particles such as electrons [16-18], ions [19], and positrons [20] to relativistic energies.

To date most laser architectures for high intensity applications have relied on solid-state gain media in the near infrared (NIR, λ=0.8-1.5 μm), limiting experiments to these wavelengths or their harmonics in the visible and ultraviolet. The quadratic increase with wavelength of parameters such as the ponderomotive energy and free electron polarizability have made the recent advances in short pulse mid infrared (mid-IR or MIR, λ~3-8 μm) and long wave infrared (LWIR, λ~8-15 μm) systems

particularly exciting, with promising results for several of the applications listed above [21-35]. The experiments and simulations described in this dissertation [36-40] explore new physics made possible by intense mid-IR and LWIR laser pulses: laser wakefield acceleration, avalanche based detection of ultralow electron and weakly-ionized plasma densities, and high-power laser self-guiding enabled by avalanche ionization.

The remainder of the dissertation is organized as follows. The rest of this chapter reviews the wavelength scaling of important laser-matter interaction parameters, as well as their effect in laser-wakefield acceleration and avalanche ionization. Chapter 2 describes our mid-IR laser system. Chapter 3 presents results from the first laser wakefield acceleration (LWFA) experiments with a mid-IR driver, along with particle-in-cell simulations. Chapter 4 presents a new concept, in which avalanche ionization is repurposed as a means for ultrasensitive detection of extremely low charge densities in gases. In the first application of avalanche, it is used to sensitively detect the presence of radioactive material. Chapter 5 describes the second application of avalanche detection: measurement of multiphoton and tunneling ionization yields in atmospheric pressure gases over a record 14 orders of magnitude, a result particularly germane to high power atmospheric self-guiding of LWIR pulses. Armed with this more complete understanding of laser-induced ionization in gases, Chapter 6 presents simulations of LWIR pulse guiding that show that essential role of discrete plasma breakdown sites. Chapter 7 summarizes the dissertation and discusses ongoing and future work.

1.2 Wavelength dependence of key parameters in laser-matter interactions

1.2.1 Linear focusing

The lowest order beam-like mode of the electromagnetic field of wavelength $\lambda\ (= 2\pi/k)$ in the paraxial approximation has the Gaussian electric field and intensity profiles

$$\mathbf{E}(r,z) = \mathbf{E}_0 \left(\frac{w_0}{w(z)}\right)^{1/2} \exp\left(-\frac{r^2}{w^2(z)}\right) \exp\left(\frac{ikr^2}{2R(z)}\right) \exp(i\tan^{-1}(z/z_0)) \exp(ikz)$$

$$I(r,z) = I_0 \frac{w_0}{w(z)} \exp\left(-\frac{2r^2}{w^2(z)}\right) \propto |\mathbf{E}(r,z)|^2\,, \tag{1.1}$$

where r is the radial coordinate from the propagation axis and z is longitudinal coordinate. The beam's z–dependent field amplitude $1/e$ radius (and intensity $1/e^2$ radius) is $w(z) = w_0(1 + \left(\frac{z}{z_0}\right)^2)$, where w_0 is the field $1/e$ (and intensity $1/e^2$) radius at the narrowest part of the beam (beam waist, $z = 0$). The characteristic diffraction distance for $I \to I_0/2$ in a background medium of refractive index n_0 is $z_0 = \pi n_0 w_0^2/\lambda$, the Rayleigh range. The field's phase front radius of curvature is $R(z) = z(1 + \left(\frac{z_0}{z}\right)^2)$ and the phase advance owing to converging and diverging phase fronts (the "Gouy phase") is $\Delta\Phi_{Gouy} = \tan^{-1}(z/z_0)$. A beam of initial $1/e^2$ diameter D launched at $z = -f$ has a beam waist ($z = 0$) of $w_0 = 2\lambda \tan(f/D)\,(\pi n_0)^{-1} \cong 2\lambda f/(\pi n_0 D)$ for $f \gg D$ and "f/number" given by f/D. This models focusing of a parallel beam of diameter D over a focal length f, for which a pulse of peak power P_0 yields a peak intensity $I(r = 0, z = 0) = I_0 = 2P_0/(\pi w_0^2)$. Thus for fixed P_0 , the

beam waist area (focal spot area) scales as $w_0^2 \propto \lambda^2$, the focal volume $V \sim 2z_0(\pi w_0^2) \propto \lambda^3$, and the peak intensity $I_0 \propto \lambda^{-2}$.

Since several parameters discussed below show a $I\lambda^2$ dependence, at first glance it would appear that the larger focal spot would lead to invariant behavior (constant $I\lambda^2$) at longer wavelengths for fixed focal geometry. However, we note that (i) achieving the same value of $I\lambda^2$ over a larger area ($\propto \lambda^2$) or volume ($\propto \lambda^3$) can be strongly beneficial for applications, (ii) the peak pulse intensity in some applications, such as relativistic and nonrelativistic filamentation, is set not by linear focusing conditions but rather by nonlinear effects, strongly favoring long λ for some applications, and (iii) some basic processes are favored or disfavored at long λ; for example, multiphoton ionization is strongly disfavored, a fact put to crucial use in several experiments of this dissertation.

1.2.2 Nonlinear optics and self-focusing

In linear optics, a uniform isotropic propagation medium responds to the applied electric field $\mathbf{E}$ according to $\widetilde{\mathbf{P}} = \chi\widetilde{\mathbf{E}}$, where $\widetilde{\mathbf{P}}(\mathbf{r}, \omega)$ and $\widetilde{\mathbf{E}}(\mathbf{r}, \omega)$ are the Fourier transforms of the polarization and electric field, $\chi^{(1)} = \chi^{(1)}(\omega)$ is the medium's linear frequency-dependent electric susceptibility, and $\varepsilon(\omega) = 1 + 4\pi\chi^{(1)}(\omega)$ is the linear dielectric function. For nonmagnetic materials, as we consider here, the permeability is $\mu = 1$, and so the linear refractive index is $n_0(\omega) = \sqrt{\mu\varepsilon} = \sqrt{\varepsilon} = \sqrt{1 + 4\pi\chi^{(1)}(\omega)}$. Strongly driven bound electrons in atoms and molecules, however, can exhibit a nonlinear response to the field. For a medium with a near-

instantaneous response, we can write $\mathbf{P}(\mathbf{r},t) = \chi(\mathbf{E}(\mathbf{r},t))\mathbf{E}(\mathbf{r},t)$, for a linearly polarized complex field $\mathbf{E}(\mathbf{r},t)$ with carrier frequency ω_0 and bandwidth $\Delta\omega/\omega_0 \ll 1$, where now χ depends on $\mathbf{E}$. For cases where $|\mathbf{E}|/E_{atom} \ll 1$, for a typical atomic binding field E_{atom}, we can expand $\mathbf{P}$ as a perturbation series $\mathbf{P}(\mathbf{r},t) = \chi^{(1)}\mathbf{E}(\mathbf{r},t) + \chi^{(3)}|\mathbf{E}|^2\mathbf{E}(\mathbf{r},t) + \cdots$ for a centrosymmetric medium (so even terms are zero) and lowest order terms at the central frequency ω_0. The term $\chi^{(3)}|\mathbf{E}|^2\mathbf{E}(\mathbf{r},t)$ is responsible for self-phase modulation and self-focusing. Grouping terms gives a lowest order effective susceptibility $\chi(\mathbf{E}) = \chi_{eff} = \chi^{(1)} + \chi^{(3)}|\mathbf{E}|^2$ and index of refraction $n_{eff} = \sqrt{1 + 4\pi(\chi^{(1)} + \chi^{(3)}|\mathbf{E}|^2)} \approx n_0 + n_2 I$, defining the nonlinear refractive index n_2, for $I(\mathbf{r},t) = (n_0 c/8\pi)|\mathbf{E}|^2$. For ω_0 far from atomic resonances, $n_2 > 0$ in general. The effect of such a positive, instantaneous nonlinearity is shown in Fig. 1.1. The increased refractive index at the intensity envelope peak decreases the local phase velocity $v_p = c/n_{eff}$, causing inward curving of the pulse wave fronts: self-induced focusing. Self-phase modulation (SPM) also occurs: the effective propagation phase on axis near the beam waist is $\Phi(r = 0, z, t) = (\omega_0/c)(n_{eff}z - ct)$, giving an effective frequency shift $\Delta\omega(t) = -\partial\Phi/\partial t - \omega_0 = -(\omega_0 n_2/c)z\,\partial I/\partial t$. Thus the leading edge of the pulse (where $\partial I/\partial t > 0$) red shifts and the trailing edge (where $\partial I/\partial t < 0$) blue shifts.

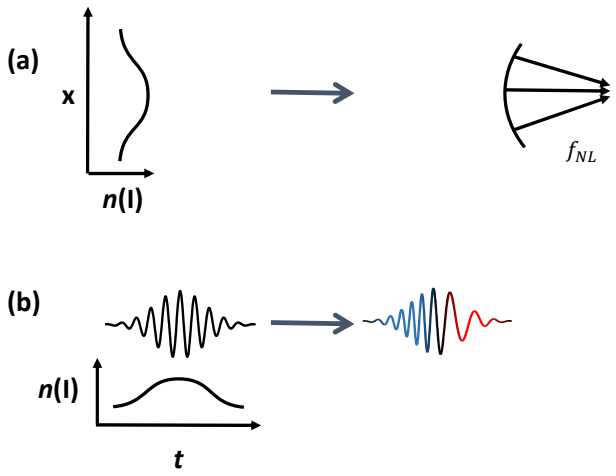

Figure 1.1. Schematic showing (a) self-focusing and (b) self-phase modulation

If the inward phase front curvature from self-focusing exceeds in magnitude the outward curvature from diffraction, a pulse will undergo self-focusing collapse. To estimate the threshold for this process, we set the nonlinear phase accumulated over a distance $|z/z_0| \ll 1$ near the beam waist to the Gouy shift: $kn_2Iz = \tan^{-1}(z/z_0) \approx z/z_0$, giving critical power $P_{cr} \sim I\pi w_0^2$, or

$$P_{cr} = \frac{\alpha\lambda^2}{n_0 n_2} \tag{1.2}$$

where the factor α is introduced to allow for a range of initial beam profiles. Detailed analysis gives values of $\alpha \approx 0.15$ for a Gaussian beam and $\alpha \approx 0.148$ for a Townes beam profile, a self-similar collapse profile that has the lowest possible P_{cr} [41]. Above P_{cr} the pulse will continuously self-focus until collapse is arrested by some defocusing mechanism, such as ionization of the medium [42] or group velocity dispersion of the wide spectrum generated by SPM [43]. In particular, filamentation or self-guiding of

femtosecond pulses in air is the result of the interplay of self-focusing, diffraction, and plasma-induced refraction [2,3].

An important point from Eq. (1.2) is that $P_{cr} \propto \lambda^2$, so that the required threshold power for self-focusing collapse quickly increases with λ. Since pulses which greatly exceed P_{cr} are subject to the transverse modulational instability and beam breakup into multiple filaments, there has been interest in filamentation at longer wavelengths in order to increase the high power throughput in a single high intensity channel [21-23,44-47]. This will be further discussed in Chapter 6. We note that filamentation has been described extensively elsewhere [2,3], and will not give a detailed overview here.

1.2.3 Ponderomotive energy and ponderomotive force

While electron motion in a non-uniform laser field (such as a beam) is primarily oscillatory, this fast motion over the beam intensity gradients leads to drift motion driven by an effective drift force, as we now show following Ref. [48]. Consider spatially varying electromagnetic fields defined by $\mathbf{E} = \mathbf{E}(\mathbf{r})\cos(\omega t)$ and $\mathbf{B} = \mathbf{B}(\mathbf{r})\cos(\omega t)$. A point charge q of mass m moving non-relativistically is accelerated by the Lorentz force

$$m\dot{\mathbf{v}} = q\left(\mathbf{E} + \frac{\mathbf{v}}{c} \times \mathbf{B}\right). \tag{1.3}$$

We consider perturbation expansions of electron velocity and position $\mathbf{v} = \mathbf{v}_0 + \mathbf{v}_1 + \mathbf{v}_2 + \cdots$ and $\mathbf{r} = \mathbf{r}_0 + \mathbf{r}_1 + \mathbf{r}_2 + \cdots$ in the small parameter $|\mathbf{v}|/c$, with the charge initially at rest ($\mathbf{v}_0 = 0$) at $\mathbf{r}_0 = 0$. To first order, the motion is dictated entirely by $\mathbf{E}$:

$$\mathbf{v}_1 = \frac{q\mathbf{E}(\mathbf{r}_0)\sin(\omega t)}{m\omega}, \tag{1.4a}$$

$$\mathbf{r}_1 = -\frac{q\mathbf{E}(\mathbf{r}_0)\cos(\omega t)}{m\omega^2} \quad . \tag{1.4b}$$

We now consider the second order equation of motion, including $\mathbf{B}$ and a Taylor expansion of $\mathbf{E}$ around the initial charge position, $\mathbf{r}_0 = 0$:

$$m_e\dot{\mathbf{v}}_2 = q\left((\mathbf{r}_1\cdot\nabla)\mathbf{E}(\mathbf{r}_0)\cos(\omega t) + \frac{\mathbf{v}_1}{c}\times\mathbf{B}(\mathbf{r}_0)\cos(\omega t)\right). \tag{1.5}$$

To find the drift force, we insert Eqs. (1.4a-b) into Eq. (1.5), and use $\cos(\omega t)\,\mathbf{B}(\mathbf{r}) = -(c/\omega)\sin(\omega t)\,\nabla\times\mathbf{E}(\mathbf{r})$ from Maxwell's equations. To find slow drift motion, we cycle-average the rapid oscillation, $\langle\sin^2(\omega t)\rangle = \langle\cos^2(\omega t)\rangle = 1/2$, giving

$$m\langle\dot{\mathbf{v}}_2\rangle = -\frac{q^2}{2m\omega^2}\left[(\mathbf{E}(\mathbf{r}_0)\cdot\nabla)\mathbf{E}(\mathbf{r}_0) + \mathbf{E}(\mathbf{r}_0)\times\left(\nabla\times\mathbf{E}(\mathbf{r}_0)\right)\right]. \tag{1.6}$$

Applying the identity $\mathbf{A}\times(\nabla\times\mathbf{A}) = \frac{\mathbf{1}}{\mathbf{2}}\nabla|\mathbf{A}|^2 - (\mathbf{A}\cdot\nabla)\mathbf{A}$ then leads to the cycle-averaged drift force, or "ponderomotive force"

$$\mathbf{F}_\mathrm{p} \equiv\ m\langle\dot{\mathbf{v}}_2\rangle = -\frac{q^2}{4m\omega^2}\nabla|\mathbf{E}(\mathbf{r})|^{\mathbf{2}} = -\nabla\left(\frac{q^2|\mathbf{E}(\mathbf{r})|^{\mathbf{2}}}{4m\omega^2}\right) = -\nabla U_p \ , \tag{1.7}$$

where $U_p(\mathbf{r}) = e^2E^2/4m_e\omega^2 \propto \lambda^2$ is the so-called "ponderomotive energy" for an electron, for $E = |\mathbf{E}(\mathbf{r})|$. U_p is also equal to the relativistic cycle-averaged kinetic energy $\langle K\rangle = m_ec^2\langle\gamma - 1\rangle \approx e^2E^2/4m_e\omega^2 \cong 0.093\ I\ [\mathrm{TW/cm^2}](\lambda[\mu\mathrm{m}])^2$ through third order in $|\mathbf{v}|/c$. The ponderomotive force $\mathbf{F}_\mathrm{p}$ acts to expel charges from areas of high intensity. While the direction of this force is the same for positive and negative charges, ions will feel a force smaller by a factor of m_e/m_i, leading to charge separation discussed in the context of laser wakefield acceleration in Sec. 1.3 below.

An example of the role played by the ponderomotive energy is in high harmonic generation (HHG). In HHG, an electron is liberated via tunneling ionization from an atom during a laser cycle, with its orbit then classically driven by the field to recombine with its parent atom, radiating its excess kinetic energy as a high energy photon with cutoff energy $\hbar\omega_{max} = \chi_p + 3.17U_p$, scaling with U_p [8], where χ_p is the atom's ionization potential. Since the drive intensity I for HHG is limited by the amount of plasma generation and phase slippage between the drive beam and its harmonics, moving to longer λ at fixed I has favored harmonic generation to $\hbar\omega_{max}\sim$ keV energies [30].

A useful dimensionless field quantity is the normalized vector potential, $\boldsymbol{a} = e\mathbf{A}/m_e c^2$, where $\mathbf{A}$ is the vector potential describing the electromagnetic field. If $\mathbf{A}_0$ is the peak vector potential, we define $a_0 = e|\mathbf{A}_0|/m_e c^2 \approx 8.5 \times 10^{-10}\sqrt{I\lambda^2}$ for I in W/cm^2 and λ in μm For $a_0 \ll 1$, relativistic effects are neglectable, but otherwise must be considered. It is worth noting that $a_0^2 = 4U_p/m_e c^2$, so that relativistic effects must be considered when the non-relativistic ponderomotive energy is a non-negligible fraction of the electron rest energy.

1.2.4 Strong field ionization

The atoms and molecules in common dielectric media have ionization energies χ_p ranging from 8-15 eV, as compared to optical photon energies of $\hbar\omega\sim$0.1–2 eV in the visible and infrared. Thus, single photon ionization is not possible, and ionization

occurs through multiphoton (MPI), tunneling, or collisional ionization as summarized in Fig. 1.2.

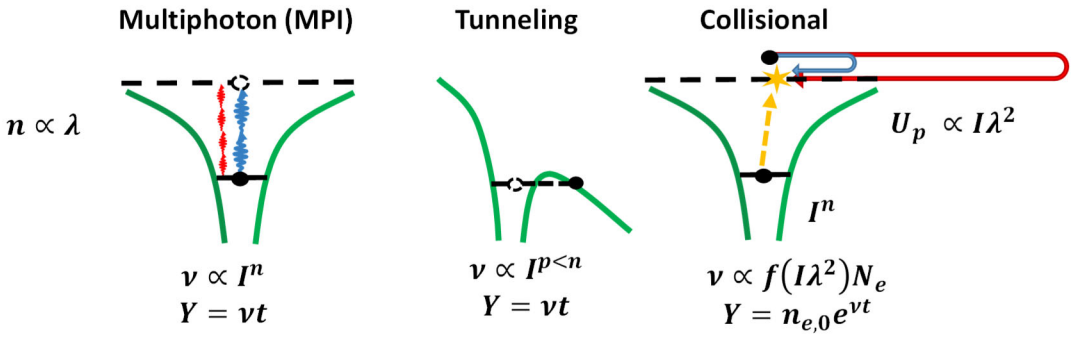

Figure 1.2. Overview of ionization mechanisms for high intensity, non-resonant laser pulses, and the scaling of associated ionization rate ν and ionization yield Y as function of time t. The green line indicates the atomic potential. Electrons (black dot) can be released through (a) absorption of n laser photons for $n = \mathrm{Int}(\chi_p/\hbar\omega)$ photons needed to exceed ionization potential χ_p of the target species, (b) tunneling through the field-distorted Coulomb barrier, or (c) ionizing collisions from laser accelerated free electrons, with rate ν proportional to existing free electron density N_e, which leads to exponential growth from an initial number of electron seeds $n_{e,0}$.

Multiphoton and tunneling ionization describe two limits of the same process, with the transition between them described by the Keldysh parameter $\gamma_K = \sqrt{\chi_p/2U_p}$ for ionization potential χ_p and ponderomotive energy U_p defined above [49]. For $\gamma_K \gg 1$, ionization is in the MPI regime, with a rate $\nu = \sigma(\omega)\, I^n$, where σ is a frequency dependent coefficient and $n = \mathrm{Int}(\chi_p/\hbar\omega)$ is the integer number of photons needed to exceed χ_p. Since the ionization rate represents the probability of an atom absorbing n photons simultaneously, it is strongly suppressed for longer wavelengths with lower energy photons. For $\gamma_K \lesssim 1$, the atomic potential is sufficiently distorted by the applied laser electric field that the electron can tunnel through the barrier, and the ionization rate scales as $\propto I^{p<n}$. Figure 1.3 plots ionization rate vs. I for $\lambda = 1$ μm and $\lambda = 4$ μm [50]. For $\lambda = 1\ \mu$m, the rate initially increases as I^{10} as predicted by $n = \chi_p/\hbar\omega$ before

transitioning to tunneling, while for $\lambda = 4\ \mu$m the rate is in the tunneling regime throughout.

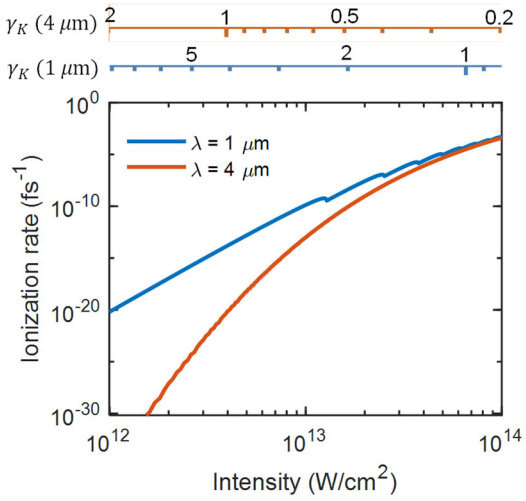

Figure 1.3. Calculated [50] ionization rate of O_2 at $\lambda = 1\ \mu$m (blue) and $\lambda = 4\ \mu$m (red). For $\lambda = 1\ \mu$m, the rate initially increases as I^{10} as predicted by $n = \chi_p/\hbar\omega$ before transitioning to tunneling, while for $\lambda = 4\ \mu$m the rate is in the tunneling regime throughout, as shown by the values of γ_K for each wavelength, top.

As intensity continues to increase, the atomic binding potential becomes sufficiently distorted and suppressed that the electron no longer sees a potential energy barrier and is directly ionized within one cycle of the optical field. Equating the peak of the distorted atomic potential with the valence electron's ionization energy for an ion core of charge state Z gives

$$I_{OB} = \frac{c}{128\pi e^6}\frac{\chi_p^4}{Z^2} \cong 4\times 10^9 \frac{\left(\chi_p\ [\mathrm{eV}]\right)^4}{Z^2}\frac{\mathrm{W}}{\mathrm{cm}^2} \tag{1.8}$$

as an intensity threshold for "over-the-barrier" ionization. Note that I_{OB} is independent of λ, but the time to achieve the peak field (a half cycle) is longer for longer λ.

Up to this point, we have considered ionization produced by laser irradiation of an isolated atom. In gas and condensed media targets, additional ionization can occur through collisional ionization, whereby existing free electrons gain sufficient energy to ionize nearby neutral species upon impact. In contrast with the other ionization processes, the rate of collisional ionization of an atom or ion is proportional to the number of already liberated electrons in the laser field, with the free electron population increasing exponentially when collisional and diffusive losses are overcome by laser heating. This is the so-called cascade or avalanche ionization process, which is clearly dependent on the atomic/molecular density of the target. A detailed description of avalanche ionization is given at the end of this chapter. Another density-dependent process, excitation-induced dephasing (EID) [51-54], has been proposed as a mechanism for enhanced ionization at moderate intensities. While the rate itself is predicted to be nearly independent of wavelength, its effect on experiments would be more evident at long λ as discussed in Chapter 5.

1.2.5 Nonlinear optics in plasma

The dielectric function of a collisionless cold plasma is $\varepsilon(\omega) = 1 - (\omega_p/\omega)^2$, giving the linear refractive index

$$n(\omega) = (1 - (\omega_p/\omega)^2)^{1/2} = (1 - N_e/N_{cr})^{1/2} \quad , \qquad (1.9)$$

where $\omega_p = \sqrt{4\pi N_e e^2/m_e}$ is the plasma frequency for electron density N_e, and $N_{cr} = m\omega^2/4\pi e^2 = 1.1 \times 10^{21}/(\lambda[\mu\text{m}])^2\ \text{cm}^{-3}$ is the critical density. Here, it is understood that the free electron polarizability far exceeds that of ions (in the ratio

m_i/m_e). A laser pulse with carrier frequency ω_0 (and bandwidth $\Delta\omega/\omega_0 \ll 1$) traveling through such a plasma has phase and group velocities

$$v_p = \frac{c}{n(\omega_0)} \ , \qquad v_g = [(\partial k/\partial\, \omega)_{\omega=\omega_0}]^{-1} = \ [(\partial(\omega n/c)/\partial\, \omega)_{\omega=\omega_0}]^{-1} = cn(\omega_0). \tag{1.10}$$

For many laser interaction experiments, linear pulse propagation in plasmas near or above N_{cr} is important for processes including resonance absorption and simple reflection [55,56].

As discussed in Sec. 1.2.3, once the normalized vector potential no longer satisfies $a_0 \ll 1$ we must consider relativistic electron dynamics in the laser field which, in turn, affects the plasma refractive index according to

$$n = \left(1 - \frac{\omega_{p0}^2}{\gamma\omega^2}\right)^{\frac{1}{2}} \approx n_0 + \frac{1}{4n_0}\frac{N_e}{N_{cr}}a_0^2 \approx n_0 + n_{2,rel}(\lambda)I$$
$$n_{2,rel}(\lambda) = \frac{r_0^3}{2\pi^2 e^2 c} N_e \lambda^4 \tag{1.11}$$

where $\omega_{p0}^2 = 4\pi N_e e^2/m_e$, $\gamma \cong \gamma_\perp = \sqrt{1 + a_0^2} \cong 1 + \frac{1}{2}a_0^2$ to leading order, $n_0 = (1 - (\omega_{p0}/\omega)^2)^{1/2}$, $r_0 = e^2/m_e c^2 \approx 2.8 \times 10^{-13}$ cm is the classical electron radius, and we take $\frac{N_e}{N_{cr}} \ll 1$. While, to leading order, the relativistic nonlinear correction to the refractive index of plasma is proportional to I, similar to a dielectric medium, the λ^4 wavelength sensitivity (for fixed I and N_e) strongly favors long λ pulses. Note that while linear focusing limits $I\lambda^2$ in the focus (or beam waist) to be constant for fixed power and focusing geometry, as discussed in Sec. 1.2.1, nonlinear focusing can remove this constraint on I. Using Eq. (1.7), the critical power for relativistic self-

focusing in subcritical density plasmas is $P_{cr} \approx 17\, N_{cr}/N_e$ GW [57,58]. Nonlinear self-focusing in plasmas enables initially modest intensity beams ($a_0 \ll 1$) to achieve the relativistic intensities ($a_0 \gtrsim 1$) necessary for laser-plasma particle acceleration (discussed below) as well as support relativistic self-guiding at high intensity over multiple Rayleigh lengths.

Since P_{cr} is a measure of the transition to relativistic laser plasma physics, the ratio N_{cr}/N_e sets parameters for the types of targets needed. For near-infrared lasers ($\lambda \sim 1$ μm), $N_{cr} \sim 10^{21}\mathrm{cm}^{-3}$. This lies between typical gas (10^{19} cm^{-3}) and solid (10^{23} cm^{-3}) densities, suggesting targets such as complex aerogels [59], very high pressure and/or cryogenically cooled gas jets [60-63], or plasma generated from a solid target by a controlled pre-pulse [64]. In the MIR to LWIR, on the other hand, $N_{cr} \sim 10^{18} - 10^{20}\ \mathrm{cm}^{-3}$ can be achieved with moderate density gas targets. This has strong advantages for the design of gas jets or gas flow targets where a high repetition rate laser interaction is desirable.

1.3 Laser wakefield acceleration

A plane electromagnetic wave with multiple optical cycles will symmetrically accelerate and decelerate charges over the length of the pulse such that there is no net energy gain in the absence of collisions or other broken symmetries [65]. For an optical beam, however, charges are accelerated away from the high intensity region by the ponderomotive force $\mathbf{F}_\mathrm{p} = -\nabla U_p$, which in the relativistic regime is given by $\mathbf{F}_\mathrm{p} = -mc^2\nabla\langle\sqrt{1+\mathbf{a}\cdot\mathbf{a}} - 1\rangle$, for normalized vector potential $\mathbf{a}$. For a focused optical pulse

in plasma, the ponderomotive force excites a wake behind the pulse as electrons are expelled from the laser axis, as shown in Fig. 1.4, and for sufficiently high intensity, can completely evacuate the local wake of electrons ("blow-out") [66-68]. The electrostatic field in these wakes can reach the "wave breaking" field, $\sqrt{2\omega/\omega_p}E_0 = \sqrt{2\omega/\omega_p}cm_e\omega_p/e \cong 96(N_{cr}/N_e)^{1/4}\sqrt{N_e[\mathrm{cm}^{-3}]}$ V/m, above which electron orbits are dephased from the oscillating wake [17]. For typical target plasma densities $\sim 10^{18}\ cm^{-3}$, field gradients up to $E_0 \sim 100$ GV/m are achievable, spurring strong worldwide interest and activity in "laser-wakefield acceleration" (LWFA), a leading concept for next generation accelerators [16-18,61-62,66-94]. In comparison, conventional accelerators using metallic structures are limited by damage thresholds to field gradients on the order of ~100 MV/m [95,96].

Plasma waves are most efficiently excited for pulse lengths matched to the size of the trailing wake, namely $c\tau \sim \lambda_p/2 = \pi c/\omega_p$ in the so-called resonant acceleration regime. Pulses much longer than $c\tau \sim \lambda_p/2$ will experience feedback from the refractive effect of the plasma waves, leading to self-modulation and breakup of the beam into 'pulselets' spaced at $2\pi c/\omega_p$ (also understood as stimulated Raman scattering) [69-71]. Electron acceleration in this regime is called self-modulated laser wakefield acceleration (SM-LWFA), the process important to Ch. 3 of this dissertation. Under SM-LWFA, electrons are continually injected into multiple wake 'buckets', experiencing acceleration and deceleration, and leading to exponential spectra of the accelerated beam [61,62,72-74]. In LWFA, electrons can be injected into the

accelerating structure in several ways. For large amplitude plasma waves, background plasma electrons can dephase from the wave and be injected into the accelerating structure ("wave breaking") [73,75-76]. For a long enough laser pulse, this injection can be laser-assisted [77]. Electrons can also be injected at gas profile discontinuities and gradients [76,78,79], through ionization of high charge states of plasma ions at the peak of the pulse or with a secondary pulse [80-83], by coupling an electron bunch from another accelerator into the plasma wave structure [84-85], or with colliding pulses [87,88]. In 2004, several groups made an important advance by resonantly exciting plasma wakes in the "blow-out" regime with a pulse strong enough to drive wave breaking only in the first plasma oscillation; charge loading ('beam loading') of the wake truncated subsequent wake dynamics and resulted in quasi-monoenergetic, low divergence beams [89-91]. An extensive review of the physics of laser wakefield acceleration and various schemes for controlling injection, energy, charge, and beam quality is given in [17,18].

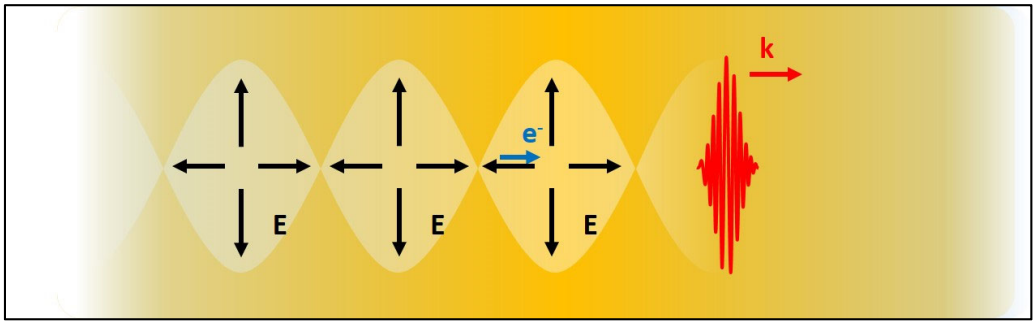

Figure 1.4. Schematic of LWFA. A laser pulse (red) propagating along **k** expels electrons due to the ponderomotive force, setting up plasma density oscillations in its wake (yellow). The charge separation between electrons and nearly stationary ions leads to a strong electric field (black arrows) which accelerates electrons (blue) behind the laser pulse. Used with permission from [92].

To gain insight into the wavelength scaling of LWFA, we note that the dynamics of a collisionless, fully-ionized plasma can be fully described by Maxwell's equations and the relativistic Lorentz force equation. Neglecting collisions is an excellent approximation for LWFAs, since collision times greatly exceed the laser pulse duration at typical plasma densities ($N_e/N_{cr} \ll 1$) [17]. Normalizing all parameters as follows

$$\widetilde{x_i} = \frac{x_i \omega_{p0}}{c}, \quad \tilde{t} \to \omega_{p0} t, \quad \widetilde{N_e} \to \frac{4\pi e^2 N_e}{m_e \omega_{p0}^2}, \quad \tilde{\mathbf{E}}, \tilde{\mathbf{B}} \to \frac{e\mathbf{E}, \mathbf{B}}{mc\omega_{p0}}, \quad \tilde{\mathbf{v}} \to \frac{\mathbf{v}}{c}, \qquad (1.12)$$

produces the following dimensionless equations for the fields and particles:

$$\tilde{\boldsymbol{\nabla}} \cdot \tilde{\mathbf{E}} = \widetilde{N_e} - \widetilde{N_{e0}}, \qquad (1.13a)$$

$$\tilde{\boldsymbol{\nabla}} \cdot \tilde{\mathbf{B}} = 0, \qquad (1.13b)$$

$$\tilde{\boldsymbol{\nabla}} \times \tilde{\mathbf{E}} = -\partial \tilde{\mathbf{B}} / \partial \tilde{t}\,, \qquad (1.13c)$$

$$\tilde{\boldsymbol{\nabla}} \times \tilde{\mathbf{B}} = \tilde{\mathbf{j}} + \partial \tilde{\mathbf{E}} / \partial \tilde{t}, \qquad (1.13d)$$

$$\frac{\mathrm{d}}{\mathrm{d}\tilde{t}} (\gamma \tilde{\mathbf{v}}) = \left(\tilde{\mathbf{E}} + \tilde{\mathbf{v}} \times \tilde{\mathbf{B}}\right), \qquad (1.13e)$$

where $\widetilde{N_e} - \widetilde{N_{e0}}$ is the normalized charge density perturbation (assuming stationary ions), and $\tilde{\mathbf{j}}$ is the normalized current $\widetilde{N_e} \int \tilde{\mathbf{v}} f(\tilde{\mathbf{v}}, t) \mathrm{d}\tilde{\mathbf{v}}$ integrated over the electron velocity distribution. Equations (1.13a-e) are self-similar even as ω_{p0} is varied. In particular, an increase in λ by a factor α while keeping $N_e/N_{cr} = \omega_{p0}^2/\omega^2$ fixed implies self-similarity—similar wake dynamics and electron acceleration to the same final kinetic energy K —for modified laser intensity $I \to I/\alpha^2$, spot size $w_0 \to w_0 \alpha^2$, pulse length $\tau \to \alpha\tau$, pulse energy $\varepsilon_l \to \alpha \varepsilon_l$ over an acceleration distance $L \to \alpha L$,

while leaving pulse power $P \propto Iw_0^2$ and $a_0 \propto I\lambda^2$ unchanged. In this scaled system, there will be an increase in accelerated charge $n_a \propto N_e x_i^3 \rightarrow \alpha n_a$, but no net change in accelerator efficiency Kn_a/ε_l. This follows the semi-empirical scaling presented in [68] for the nonlinear "blow-out" regime after noting that $N_e \propto \lambda^{-2}$ for fixed N_e/N_{cr}. In practical terms, this means that any optimized LWFA in a pre-ionized target driven by a $\lambda = 4\ \mu$m mid-IR laser will achieve the same final energy and efficiency as one driven by a $\lambda = 800$ nm laser with a 5× smaller energy and pulse length; there will be an increase in charge for the mid-IR driver, but at the cost of an increase in driver energy.

Given this predicted invariance, wavelength scaling studies for LWFA focus either on a breakdown of the assumptions in the above scaling, or technical advantages offered by mid-IR drivers. In the first case, ionization dynamics of neutral species or high charge states of plasma ions near the peak of the pulse at different wavelengths can affect the excitation of the wake or the injection of electrons [93,94]. In the second case, we note achieving critical density is far easier in the MIR/LWIR, while the increased bubble size for all N_e/N_{cr} regimes simplifies wake diagnostics or external injection. We discuss these considerations further in Chapter 3.

1.4 Avalanche breakdown

We now examine how laser-driven avalanche breakdown—central to Chapters 4-6 of this dissertation—depends on wavelength scaling through the single photon energy, multiphoton ionization rates, normalized pulse length $\omega\tau$ (number of cycles), and electron ponderomotive energy. While the physics and applications discussed in

Sections 1.2-1.3 have been extensively studied, there are novel aspects of mid-IR driven picosecond breakdowns that are essential for the work in this dissertation. As such, we will review the basics of avalanche ionization in greater detail.

Laser-induced "sparks" were observed soon after the invention of the laser [97-99], and immediately attracted significant interest. Ionization in gases for which the ionization potential greatly exceeded the photon energy initially surprised observers and spurred the development of multiphoton ionization theory [100-101] and the more complete Keldysh theory of strong field ionization [49,102]. Researchers developed a consensus that laser induced breakdown was (i) seeded by multiphoton ionization of the target gas or contaminants [103] followed by (ii) collisional heating and exponential electron density growth (avalanche ionization) and saturation [99,104-109]. From the perspective of understanding and applying the avalanche part of the process (as we do in this dissertation), the available visible and near-IR laser drivers of the time were not ideal, because the strong intensity sensitivity of MPI seeding affected the exponential phase of free electron growth. Simulations of free electron population growth rates were complicated by the need to account for elastic and inelastic electron-neutral collisions and laser-atom interactions, for which rates where not well known. As well, scaling from well-characterized experimental studies for microwave and DC discharges [110-111] was complicated by the new multiphoton effects [106].

Here we show that the combination of increased ponderomotive energy and suppressed MPI rates at mid-IR laser wavelengths, together with 10-100 ps pulse durations, makes possible a precise, quantitative understanding of laser driven

avalanche, enabling its application to measurements of ultralow, transient electron densities, and avalanche growth rates. Throughout the remaining discussion, we will discuss avalanche breakdowns in ambient (1 atm) air, but the general principles can be applied to other gases and pressures after adjusting collision rates for species and density dependence.

1.4.1 Electron heating

If the peak quiver energy of an electron ($2U_p$) is greater than the ionization potential χ_p of atoms or molecules in the surrounding gas, it can directly ionize these neutrals collisionally. However, even for $2U_p < \chi_p$, repeated dephasing elastic collisions driven by the oscillating laser field can heat an electron sufficiently to drive such ionization. Averaging over many collisions ($\tau \gg 1/\nu_e$) gives a classical collisional heating rate per electron

$$W_{coll} = \frac{e^2E^2}{2m_e\nu_e}\frac{1}{\omega^2/\nu_e^2 + 1} \tag{1.14}$$

from the Drude-Lorentz plasma model [108]. The elastic collision frequency is $\nu_e = \nu_{en} + \nu_{ei}$, with contributions from electron-neutral and electron-ion collisions. During the formative stage of breakdowns in neutral gases, $\nu_{en} \gg \nu_{ei}$. For laser frequencies $\omega \gg \nu_e$ in atmospheric range gases, Eq. (1.9) reduces to $W_{coll} \sim 2U_p\nu_e \propto I\lambda^2$. In atmospheric pressure air, where $\nu_{en} \sim 2 - 4$ ps^{-1} over a broad energy range [112,113], wavelengths up to $\lambda \sim 300$ μm ($f \sim 0.4$ THz) show a λ^2 increase in heating.

For high frequency collisions typical in solids, where $\nu_{en} \sim 1$ fs^{-1} and $\omega < \nu_e$, the electron energy gained over a time $\tau_e = 1/\nu_e$ is $= e^2E^2/2m_e\nu_e^2 = (\omega/\nu_e)^2\ 2U_p$,

much less than the peak quiver energy $2U_p$ in a field cycle. The heating rate is then wavelength-independent ($\propto I$) for approximately $\lambda > 300$ nm. This picture also applies for $\lambda \gg 300$ μm in air.

1.4.2 Breakdown threshold

During breakdown evolution, laser-induced electron heating is offset by energy losses to inelastic collisions and to thermal diffusion. Inelastic collisions include excitation of rovibrational and electronic states, molecular dissociation, and ionization. As well, the avalanche growth rate ν_i in electron number—determined by electron heating—is offset by losses at rate ν_{loss} from attachment, recombination, or diffusion out of the focal volume. For a long drive pulse ($\tau \gg$ ns), neglecting diffusion and assuming $\omega \gg \nu_e$, this indicates a breakdown threshold

$$I_t \propto \frac{\alpha}{p(\text{atm})\lambda(\mu\text{m})^2} \tag{1.15}$$

for a constant α set by the loss mechanisms, and where we note that $\lambda^2 p \propto 2U_p \nu_{en}$, the heating rate per electron [107]. Extrapolating from work done in air at microwave frequencies [106,110] suggests $\alpha = 0.3$ TW/cm^2, in reasonable agreement with theory [106,114] and experiment [111,115-117] on laser breakdowns. However, deviation from the threshold in (1.15) was observed for breakdowns seeded by dust or aerosols [118-120], or from single and multi-photon effects in the NIR/visible as discussed below [121-124].

Even above I_t, exponential growth seeded by individual electrons will only be "experimentally detectable", such as with plasma imaging or conductivity

measurements, if the number of electrons $n_f = n_0 e^{\nu_i \tau}$ after a pulse of length τ has grown by a factor of $n_f/n_0 \sim 10^8$-10^{10} from initial number n_0. This indicates an effective "time limited" breakdown threshold set by $\nu_i(I) \geq \ln(n_f/n_0)/\tau$. Simplistically assuming $\nu_i \propto 2U_p \nu_{en}$ and taking $n_f/n_0 \sim 10^8$ leads to a modified form of Eq. (1.15),

$$I_t' = \frac{\alpha}{p\lambda^2\tau} \approx \frac{800\ \mathrm{TW/cm^2}}{p\ [\mathrm{atm}]\ (\lambda\ [\mu\mathrm{m}])^2\ \tau\ [\mathrm{ps}]}, \tag{1.16}$$

where the numerical value of α here assumes that only 10% of heating is spent on ionization of air for $\tau < 1$ ns breakdowns, based on empirical rate data for N_2 [111]. Comparing with experimental results in Chapters 4-5 and theoretical rates in Chapter 6 indicates this expression is reasonably accurate (within 2 ×) for pulses from ~10 ps-1 ns. Eventually the relationship breaks down, since the collisional ionization rate in air does not continue to increase as electron heating (and electron velocities) rise, but peaks at $\nu_{i,max} \sim 4.7$ ps^{-1} for ~300 eV electron energies before declining at higher energies [112,113].

This maximum growth rate indicates a full breakdown in atmospheric air from a single seed ($n_f/n_0 \approx 10^8$) requires a pulse longer than ~4 ps, and that an interaction with a pre-existing weakly-ionized plasma in air must last longer than $\sim \nu_{\mathrm{i,max}}^{-1} \sim \nu_{en}^{-1} \approx$ 250 fs in order to observe substantial collisional heating or electron density growth.

1.4.3 Single and multi-photon effects

The λ^{-2} threshold dependence in Eqs. (1.15) and (1.16) inherently assumes that breakdown heating, losses, and semi-equilibrium electron velocities are determined

uniquely by the quiver energy, and that the discrete photon energy has no effect, as appropriate for microwave (classical) avalanche breakdown. Early theoretical work on laser-induced avalanche established that treating the field classically and quantum mechanically gave equivalent results if the average kinetic energy of plasma electrons exceeded the photon energy $\hbar\omega$ [99,105,106]. Near threshold, the average electron energy is a few eV [106,110,114], such that microwave theory readily applies for photon energies $\hbar\omega \leq 1$ eV ($\lambda > 1\ \mu$m). At shorter wavelengths, applying a quantum Boltzmann approach predicts peaks in the distribution function at multiples of the photon energy [106]. In addition, while microwave theory treats neutral electronic excitations as a loss, these excited states can contribute to ionization through multiphoton processes [106,125]. Both effects increase ionization rates, such that experiments observed deviations from the classical breakdown threshold in the NIR, with a peak threshold in the visible and declining thresholds at shorter wavelengths [121–124]. Separate from these modifications to the breakdown rate, shorter wavelengths also increase the initial number of seed electrons through direct multiphoton/tunneling ionization of the background gas. At an extreme limit, ultraviolet lasers can exhibit breakdown which appear to be driven entirely by multiphoton ionization, particularly when enhanced by resonances with molecular excited states [126–127]. These overlapping frequency dependent effects prevented unambiguous measurements of laser–induced avalanche growth rates.

If avalanche is envisioned for measuring an existing low density of free electrons or negative ions, additional MPI–generated seeds will mask the desired

signal. In particular, free electron and negative ion densities are predicted to be $<10^7$ cm^{-3} near a strong radioactive source, and $\sim 10^2$–10^4 under background conditions ([128–130], Chapter 4). First experiments on radioactive detection using avalanche ionization with a near-infrared source ($\lambda = 800$ nm, 200 ps, ≥ 1 TW/cm^2) showed no sensitivity to radioactive seeding [131], as opposed to successful radiation detection with avalanche presented in Chapter 4. Calculations [50] for these conditions in the NIR (1 TW/cm^2) indicated that multiphoton ionization of O_2 generated electron densities of $\sim 10^{11}$ cm^{-3} within the first 10 ps of the pulse, reliably seeding a stable avalanche breakdown during the remainder of the 200 ps pulse. By comparison, tunneling ionization of O_2 for the mid–IR laser used in this dissertation is an extremely low probability process, with calculated liberated electron densities of <1 cm^{-3} for a 50 ps, ≤ 3 TW/cm^2 pulse [39,50].

1.4.4 Spatial growth

Electrons generated during avalanche breakdown are necessarily local to the original seed electron, but will spread out by diffusion. Simple electron diffusion gives a characteristic plasma radius of

$$r_d = \sqrt{\frac{2\tau k_B T_e}{m_e \nu_{en}}} \approx 0.3\sqrt{\tau[\text{ps}]\, T_e\, [\text{eV}])}\ \mu\text{m} \qquad (1.17)$$

for pulse duration τ, an electron temperature T_e, and an electron-neutral collision rate of about $\nu_{en} \sim 4$ ps^{-1}. This estimate is an upper bound, since electron motion is further constrained by space charge from the nearly stationary ions (ambipolar diffusion) once the Debye length $\lambda_D = (k_B T/4\pi n_e e^2)^{1/2}$ is of the same order as the diffusion length

[132]. For the experiments in this dissertation, typical diffusion radii range from 2-30 μm for 10-100 eV plasma driven by 5-100 ps pulses. An initial low density of electrons will avalanche to create local regions of high electron density surrounded by neutral air unless the seed electrons are close enough for breakdowns to overlap, namely if $N_e > 1/r_d^3$, or ~10^9–10^{11} cm^{-3}.

Breakdowns driven by nanosecond pulses, on the other hand, undergo ion heating and significant hydrodynamic motion [133] largely avoided by picosecond breakdowns. In nanosecond pulse breakdowns, the outward-directed ionization shock front, hydrodynamic expansion, and thermal diffusion lead to ~mm size breakdowns [107], comparable in size to the laser focal volume, eliminating the possibility of discrete breakdown sites.

The discrete, countable nature of picosecond avalanche sites provides a far more quantitative picture of avalanche breakdown, allowing determination of both growth rates and initial seed density and benchmarking of simulation results, as we show in Chapters 4-6. While recent work with microwave breakdowns showed similar sensitivity to low electron densities near a radioactive source [134], that method could not achieve our precision in initial seed measurements due to microsecond pulse lengths. As such, picosecond MIR and LWIR sources provide a unique combination of pulse length and MPI suppression for driving discrete avalanches.

Chapter 2: UMD high energy ultrashort mid-IR laser system and diagnostics

2.1 Introduction to high energy ultrashort mid-infrared systems

After the development of the laser, achievable peak pulse powers quickly increased as new advances, such as Q-switching, were implemented. However, power densities above ~1 GW/cm^2 inside laser amplifiers lead to nonlinear phase distortion, self-focusing (in the same process discussed in Sec. 1.2.2) and laser damage. This limited peak powers to $\lesssim$ 1 TW, and then only in large aperture amplifiers. In chirped pulse amplification (CPA), this peak power limitation was circumvented by temporally stretching the pulse to be amplified, reducing its peak power during amplification, and then re-compressing it after amplification [135], enabling orders of magnitude higher output peak power. Figure 2.1 shows this process schematically. The key idea is the use of frequency dispersing elements that impose a longer optical path length for blue frequencies than red (positive dispersion) to stretch the pulse, followed after amplification by negative dispersion to compress the pulse. The broad near-infrared (NIR) gain spectrum of Ti:Sapphire (Ti:Al_2O_3) crystals, developed soon after CPA, enables short (5-40 fs) high energy (mJ-J) pulses. Ti:Sapphire is the dominant gain medium for high intensity, short pulse lasers, with pulse powers reaching several petawatts (PW =10^3 TW) [136,137]. Other solid state gain media used for high energy short pulses, such as Nd:glass or Yb:YAG, provide different options in energy, pulse length (longer than Ti:Sapphire) and footprint; these are limited to NIR wavelengths

λ~1 μm. Extending short pulse operation to the mid-IR ($\lambda \sim 3-8\ \mu m$) has been complicated by the lack of well-developed gain media. Recently, there have been demonstrations of femtosecond pulse oscillation and amplification in chalcogenide doped Cr and Fe (Cr:ZnS(e) [138,139], Fe:ZnSe [140,141]) as well as fibers doped with Tm, Ho, or Er [142,143], along with advances in pump lasers for these gain media [144,-146]. These lasers, however, still in active development, have only recently achieved TW-level operation. High pressure λ~10 μm CO_2 amplifiers, while able to amplify short pulse high power pulses, have a modulated gain spectrum (from CO_2 molecule rotational states) that produces a train of multi-picosecond pulses not well-suited to many experimental applications.

The primary route to achieving high energy femtosecond pulses in the mid-infrared has been the use of optical parametric chirped pulse amplifiers (OPCPA), which can naturally support wide bandwidths with proper phase matching, and which do not depend on conventional gain material in the mid-IR. The following sections give an overview of this process and its implementation in our laser system.

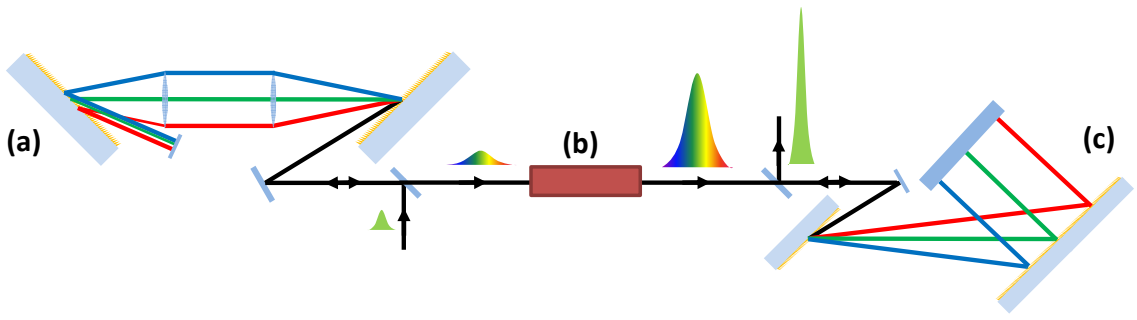

Figure 2.1. Concept of chirped pulse amplification (CPA), with example of (a) positive and (c) negative dispersion elements, applied before and after (b) amplification of the pulse.

2.2 Optical parametric amplification

An optical parametric amplifier (OPA) operates by overlapping an intense pump beam and a seed beam in a nonlinear crystal whose nonlinear optical response mediates energy transfer between them parametrically (i.e. leaving the energy state of the material unchanged). Pump photons are down-converted into a signal photon in the seed beam and an accompanying idler photon [147,148]. The generated idler frequency is dictated by energy conservation, while effective amplification is limited by dispersion, namely

$$\omega_p = \omega_s + \omega_i, \tag{2.1a}$$

$$k_p = k_s + k_i. \tag{2.1b}$$

for pump (p), signal (s) and idler (i) frequencies ω and wave numbers $k_m = 2\pi n(\omega_m)/\lambda_m$ for frequency dependent index $n(\omega_m)$. Since many nonlinear crystals are also birefringent, the second condition can be met by using beams with different polarizations with respect to the optical axis, and then tuning the angle between propagation and optical axes for optimal phase matching. Since this optimal angle is different for different frequencies in the pulse bandwidth, non-optimized frequencies will experience a phase mismatch $\Delta k = k_p - k_s - k_i$. After a distance $L_k = \pi/\Delta k$, the signal and pump beam will slip out of phase, resulting in attenuation rather than amplification of the signal and idler pulses. This phase walk-off, together with deterioration of the pump beam profile, dictate the use of multiple, thin ($L < L_k$) crystal stages for amplification.

By pumping with widely available NIR solid state lasers and using a broadband NIR signal beam, it is possible to generate broadband mid-IR idler pulses which can be compressed to femtosecond durations. In an OPCPA,, as in conventional CPA sources, seed pulses are stretched to picosecond to nanosecond durations to avoid material damage in the amplification chain, followed by compression of the signal and/or idler pulses.

2.3 UMD mid-IR TW laser design

All experiments in this thesis were performed with a hybrid OPA/OPCPA (AmpLight [149]) mid-IR laser system in the Intense Laser-Matter Interactions Lab at the University of Maryland, shown schematically in Fig. 2.2. The laser produces ~25 mJ, ~90 fs pulses at center wavelength λ=3.9 μm. The master oscillator for the system is a monolithic Yb:KGW oscillator and regenerative amplifier (Pharos, Light Conversion), which produces 1 mJ, 274 fs pulses centered at λ=1024 nm at a 6 kHz repetition rate. Approximately ~1/3 of the ~30 nJ, 87 MHz repetition rate oscillator output is split off to directly seed a Nd:YAG pump laser (EKSPLA), which produces three beams with a combined output of 1 J (λ=1064 nm, 20 Hz). A few μJ of the regenerative amplifier output is focused into an YAG crystal, generating supercontinuum (SC) extending out to λ~1.5 μm through self-phase modulation. This seed beam is then amplified in three KTA (potassium titanyl phosphate) OPA stages using the remainder of the Yb:KGW laser output as the pump, generating 500 mW (80 μJ; 6 kHz) of near infrared signal. The pump delay and crystal angle are optimized for

slightly different spectral ranges in each stage, such that the final output spans λ~1.4–1.5 μm.

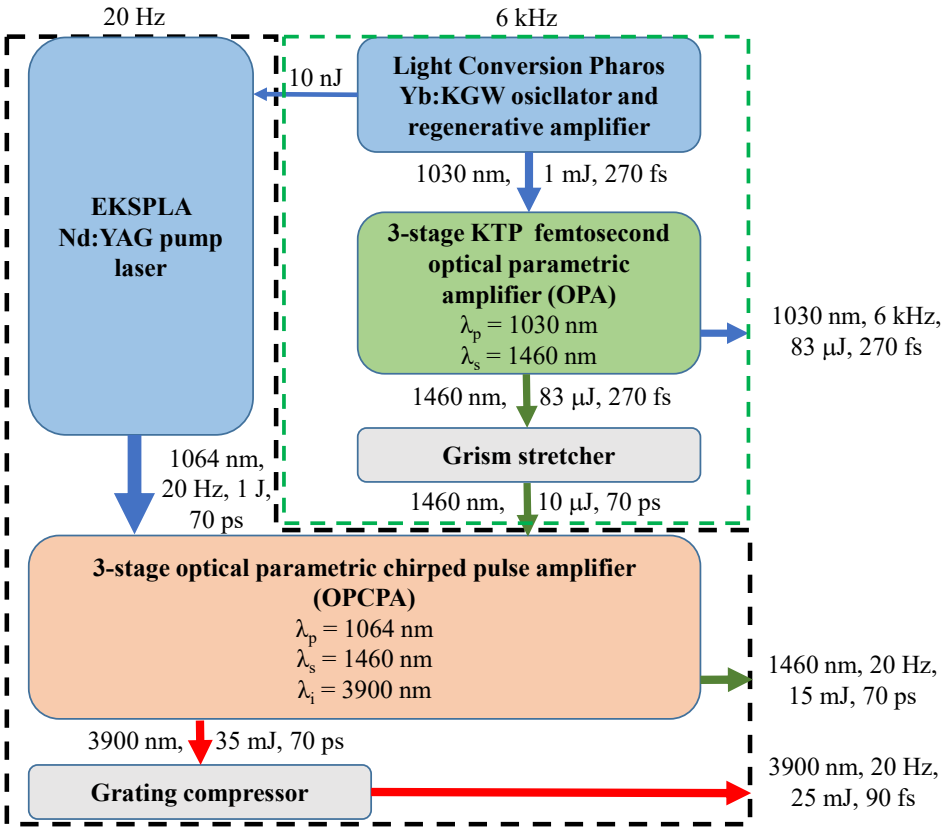

Figure 2.2. Block diagram of the UMD mid-IR laser system used for experiments in this dissertation.

While the CPA stretching/compression scheme presented in Figure 2.1 considers dispersion compensation for a single beam, the final amplified idler beam in the OPCPA has an inverse chirp, or frequency-time relationship, relative to the stretched signal beam, since $\omega_i(t) = \omega_p(t) - \omega_s(t)$. Since amplified beams are most readily compressed by a simple two-grating Treacy-style compressor shown in Fig. 2.1, achieving correct dispersion on the idler beam requires the use of a custom grism (grating + prism) stretcher for the signal beam [149]. The cross correlation wavelength

(sum frequency generation as a function of delay) of the stretched pulse, produced by mixing the signal beam with a small remainder of the 274fs, λ=1024 nm pump pulse from the OPA, is shown on the left scale of Fig. 2.3. The relation Eq. (2.1 a) then permits determination of the chirp of the stretched seed pulse, and from it the mid-IR signal pulse (right scale) generated in the OPCPA.

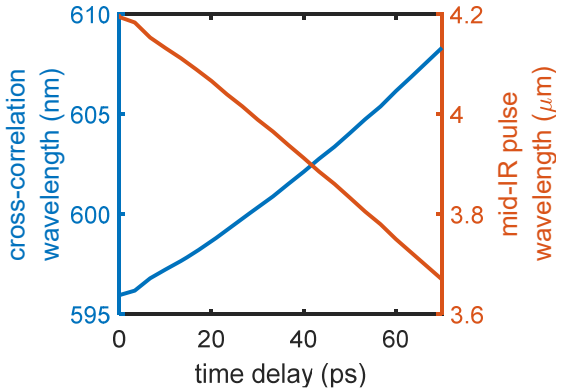

Figure 2.3. Measurement of pulse chirp (time-wavelength correspondence). Left, chirp for a cross correlation of the OPA pump (λ=1024 nm) and the stretched signal pulse, $\omega_x(t) = \omega_{p,OPA} + \omega_s(t)$. Right, chirp of the generated mid-IR pulse from the λ=1064 nm OPCPA pump, calculated as $\omega_i(t) = \omega_{p,OPCPA} - \omega_s(t)$. Lower time delay corresponds to the leading edge of the pulse.

The OPCPA portion of the mid-IR laser system is composed of three large aperture KTA (potassium titanyl arsenate) crystals for amplifying this signal beam. Three Nd:YAG pump beams (λ=1024 nm), with energies 50, 250 and 700 mJ, are each relay imaged through a vacuum relay tube from the final rod face of their amplifier chain onto the face of each crystal, minimizing diffraction of the pump beam profiles. In the first amplifier stage, the signal beam is amplified to ~1 mJ, while the mid-IR idler beam is discarded. After the second stage, the 25 mJ signal beam is discarded, with a small portion monitored with a near-IR spectrometer to calculate the spectrum

of the corresponding idler beam. The 10 mJ idler beam is then amplified to ~35-40 mJ in the last crystal with a non-collinear pump. To avoid optical damage, the beam is telescoped to a ~1 cm beam size before being compressed with a pair of 240 l/mm gratings. Due to losses on mirrors and grating efficiency, the final output pulse is 25-30 mJ at 20 Hz, with a pulse length of 87 fs, giving a peak power of ~0.3 TW. Experiments performed by Shumakova *et al*. with this same OPCPA laser design demonstrated efficient nonlinear self-broadening and self-compression to ~30 fs pulse widths by passing the beam through YAG plates or CaF_2 lenses, resulting in peak power ~1 TW [24]. Similar pulse compression has also been observed for extended, high intensity propagation in air [25]. Simulations in Chapter 3 envision possible future experiments driven with these compressed pulse parameters. Laser output in all experiments was measured with a pyroelectric power meter. Collecting a portion of the beam from a CaF_2 wedge reflector and imaging onto a PbSe photodetector indicates ~4% shot-to-shot energy fluctuations.

In addition to the mid-IR beam generated in the system, a small portion (~83 μJ) of the OPA pump is available as a probe or auxiliary pump beam. Likewise, the leftover near-infrared signal generated in the OPCPA (~15-20 mJ, 70 ps) is easily accessible as a secondary probe or heater beam.

2.4 SHG-FROG pulse measurement

Achieving the highest power and intensity requires measurement and optimization of the pulse length, for which we used scanning second harmonic generation frequency-resolved optical gating (SHG-FROG) [150], equivalent to a

spectrally resolved autocorrelation. The technique works by splitting the pulse and then recording the spectra produced from overlapping the two beams at a small angle in a nonlinear material, with a variable delay τ between the pulses. The full spectral-temporal trace recorded, $I(\omega,\tau) \propto \left|\int_{-\infty}^{\infty} E(t-\tau)\,E(t)\exp(-i\omega t)dt\right|^2$, allows algorithmic reconstruction of the pulse temporal profile by iteratively searching for a simulated or "retrieved" pulse that reproduces this spectral-temporal trace. An example trace and reconstructed temporal profile using our SHG-FROG device with a 0.2 mm $AgGaS_2$ crystal is shown below in Fig. 2.5. The 87 fs pulse FWHM is close to the 79 fs Fourier transform limit, which determines the shortest possible pulse for a measured spectrum. The mid-IR spectrum determined from the NIR signal spectrum is overlaid on the retrieved spectrum, and it is both significantly wider and smoother. This indicates both poor resolution in the NIR spectrometer, as well as possible spectral changes in the MIR beam due to a decrease in KTA transparency above $\lambda \sim 4$ μm and a varying spectral efficiency of gratings and other optics [149].

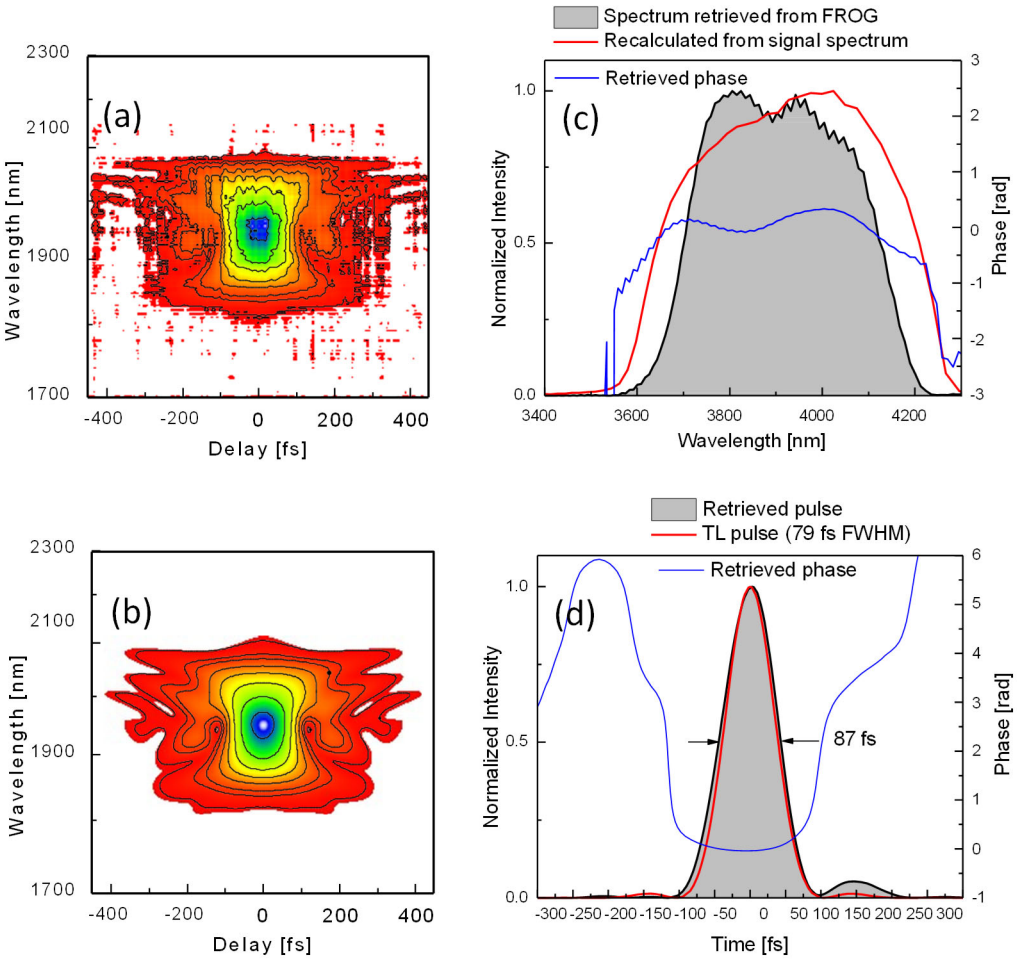

Figure 2.4. Spectral traces (a) recorded by SHG-FROG measurement, and (b) retrieved by algorithm. The retrieved pulse shows amplitude and phase for (c) the spectral field $E(\omega) = |E(\omega)|e^{i\varphi(\omega)}$ and (d) temporal field $E(t) = |E(t)|e^{i\Phi(t)}$, and has an 87 fs FWHM duration, close to the 79 fs transform limit for the same spectrum. The spectrum calculated from NIR signal diagnostics is shown for comparison in (c), indicating spectral changes through amplification and compression.

2.5 Focal spot measurements

Measuring focal spots of mid-infrared laser beams is complicated by poor detector pixel resolution on mid-IR cameras and the lack of mid-IR imaging objectives. Sufficiently large focal spots were recorded directly with a FLIR InSb detector array, which has pixel size $d_{pixel} = 15$ μm, indicating reasonable measurements for

$w_0 \sim 75 - 150\ \mu m \gg d_{pixel}$. However, since the InSb detector array exhibited nonlinearity that reduced detector sensitivity even for counts well below single pixel saturation, care needed to be taken to pre-attenuate the beam to avoid overestimating the beam spot size. The InSb nonlinearity led to incorrect intensity measurements in [37], as noted in a follow-up experiment [38]. For smaller focal spots, a knife edge was scanned through the attenuated focal spot while tracking the transmitted energy collected on a photodiode. Assuming a symmetric 2-D Gaussian spot, the fraction of energy transmitted F versus knife-edge displacement x allows extraction of the spot size w_0 of the beam from $F(x) = \int_0^x dx' \int_{-\infty}^{\infty} dy' \exp[2(-x'^2 + y'^2)/w_0^2]$. Measured spot sizes were typically $\sim 1.3 \times$ the diffraction limit. Changes in beam mode structure from the OPCPA system, or aberrations introduced by low $f/$number focusing optics occasionally decreased beam quality, necessitating focal spot measurements on a regular basis. Implementation of a deformable mirror (DM) increased the peak intensity (as measured with improvement in second harmonic generation efficiency [151]). A DM will be incorporated in a future system upgrade.

2.6 Mid-IR imaging spectrometer

As discussed in Sec. 2.3, the NIR signal spectrum is useful for determining, through Eq. (2.1a), the mid-infrared spectrum of the laser output. To capture mid-IR spectra from experimental interactions, a dedicated mid-IR spectrometer is needed. Most commercially available mid-IR spectrometers use a multi-shot scanning technique and a single pixel detector. In order to measure the mid-IR spectrum in a

single-shot, we paired an imaging spectrometer (Horiba microHR) with an InSb cryo-cooled camera (IRCameras IRC800) to construct a unique, highly sensitive, single shot mid-IR spectrometer, shown in Fig. 2.5.

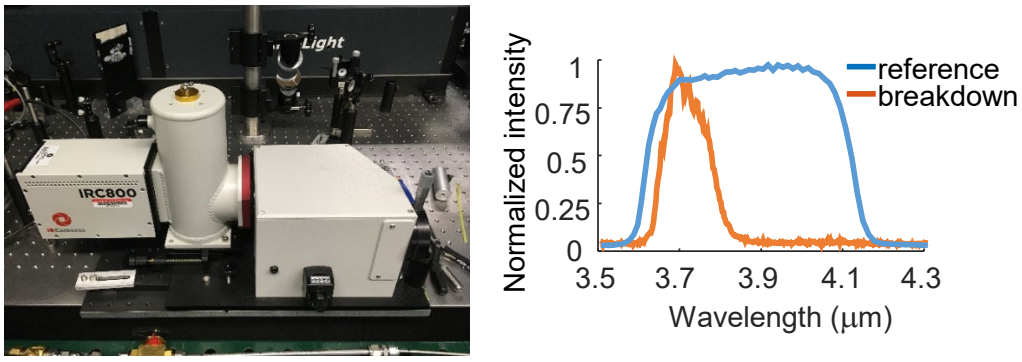

Figure 2.5. Left, single shot mid-IR imaging spectrometer. Right, spatially integrated spectrum of the chirped mid-IR pulse (reference) and an example of a spectrum backscattered from an avalanche breakdown site.

Bypassing the OPCPA compression gratings allows use of the chirped ~70 ps mid-IR pulse for avalanche ionization as discussed in Chapters 4 and 5. The spectrum of this high energy picosecond pulse is shown in Fig. 2.5 (b) ("reference"). Together with the cross correlation in Fig. 2.3, this result indicates a nearly top-hat temporal profile, with a ~50 ps FWHM and ~10 ps rising and falling edges. Since the pump pulse is positively chirped, backscatter spectra collected from avalanche breakdowns enabled detailed temporal measurements of breakdown evolution.

Chapter 3: Laser wakefield acceleration with mid-IR laser pulses

3.1 Relativistic self-focusing

Relativistic nonlinearities in mid-IR laser-plasma interaction are enhanced by both the increased normalized vector potential, which scales as $a_0 \propto \sqrt{I\lambda^2}$, and from a decrease in the critical plasma density as $N_{cr} \propto \lambda^{-2}$. At long wavelengths, achieving reproducible near-critical density targets with tunable profiles is greatly simplified, since exploding solid targets, aerogels or complex pressure-boosted gas jets can be replaced by simpler gas jets pulsed at high repetition rates or run continuously. For electron density N_e approaching N_{cr}, laser pulses experience lowered thresholds for relativistic self-focusing, onset of parametric instabilities, and enhanced absorption and coupling to plasma oscillations [55], which in turn enable such schemes as magnetic vortex acceleration of plasma ions [152,153].

In laser wakefield acceleration (LWFA) of electrons [16-18], relativistic self-focusing has long been used to both increase the laser intensity and promote self-guided propagation for extended interaction lengths [17,18]. As discussed in Sec. 1.2.5, the optical nonlinearity responsible for self-focusing arises from the relativistic corrections to the plasma refractive index in the intense laser field. Above a critical power threshold, $P_{cr} \sim 17\, N_{cr}/N_e\ (GW)$ [57,58] relativistic self-focusing overcomes diffraction and the pulse can collapse. For self-focusing in uniform plasma occurring in less than the Rayleigh range z_0, the collapse distance is given approximately by the self-focusing scale length $\ell_{sf} = z_0(P/P_{cr})^{-1/2}$ for phase fronts converging due to nonlinear phase picked up over this length. Collapse is arrested by plasma "blow-

out"—where electrons are expelled by the pulse to form a highly nonlinear plasma wake—and subsequent injection of background electrons into the wakefield can accelerate them to relativistic energies [16–18]. Laser plasma acceleration experiments relying on self-focusing have usually required large, multi-terawatt lasers.

Recently we demonstrated that very high density, cryogenically cooled gas jets [63] enable near-critical density laser-plasma interaction for Ti:Sapphire lasers at λ=0.8μm, lowering the threshold for relativistic self-focusing and allowing sub-terawatt pulses to drive highly nonlinear plasma waves in the self-modulated laser wakefield (SM-LWFA) regime [61,62]. In this chapter, we present the first experiment demonstrating laser wakefield acceleration with femtosecond mid-IR laser pulses (λ=3.9μm) in a similar setup [36]. We study electron acceleration in gas jet targets from a few percent of N_{cr} to greater than $2N_{cr}$, and perform a detailed scan of the power and length thresholds for acceleration. We also capture images of the self-focusing process with a synchronized optical λ=650nm probe, for which all the plasmas studied are well below critical density.

3.2 Experimental setup and diagnostics

Experiments were conducted with the hybrid OPA/OPCPA laser system [149], using ~25 mJ, ~100 fs pulses at λ=3.9 μm at a repetition rate of 20 Hz. The experimental setup is shown in Fig. 3.1. The laser was focused with an off-axis *f*/5 paraboloid to a 30 μm FWHM spot size, as determined by a knife edge scan. Due to losses on routing mirrors, the maximum pulse energy on target was 23 mJ, corresponding to a peak vacuum intensity ~2×10^{16} W/cm^2 and a normalized vector potential of $a_0 \sim 0.5$. The

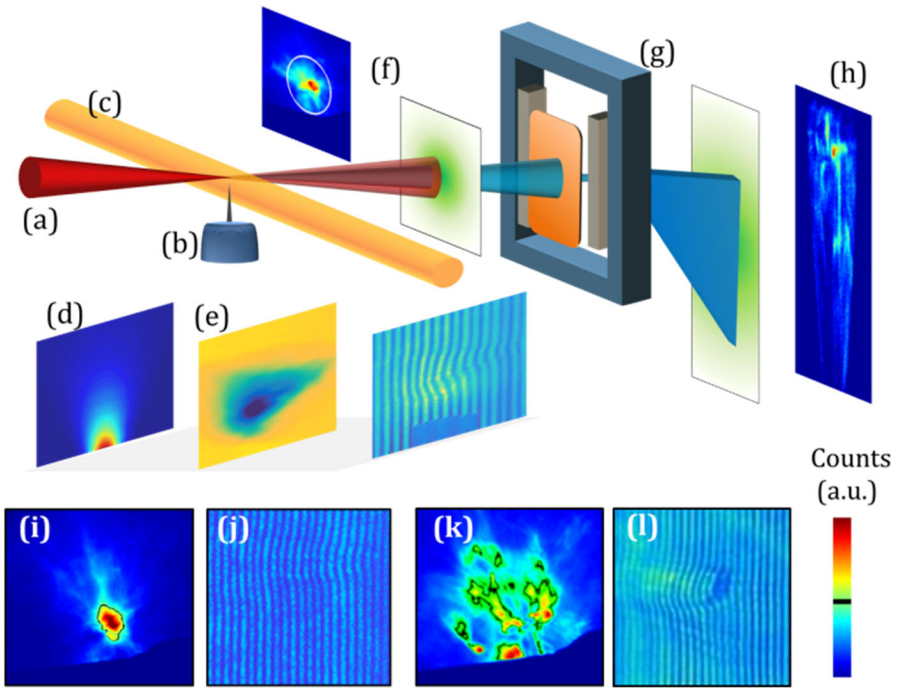

Figure 3.1. Top, Schematic of experiment. Mid-IR (λ =3.9 μm, 105 fs, 10-23 mJ) laser pulses (a) are focused on to the output of a 150 μm orifice gas jet backed at high pressure (b). A synchronized 650 nm probe (c) allowed extraction of both neutral gas densities (d) and plasma induced phase (e). Electron beam profiles (f) were collected by imaging a Lanex screen to a low noise detector. A removable electron spectrometer (g) selected a portion of the beam and dispersed it with a dipole field onto a Lanex screen to capture electron spectra (h). Bottom, example electron beam profiles and interferograms at $P/P_{cr} =$ 4 (i, j) and $P/P_{cr} = 10$ (k, l), where the latter images show relativistic multi-filamentation. Beam images are scaled to the maximum counts, and the black line indicates a 50% contour, which for the single beam on the left has a divergence ~200 mrad.

pulse energy on target was decreased in steps by inserting absorptive glass plates into the beam. The FWHM pulse duration was in the range 105–130 fs, depending on the inserted plates, as measured with a SHG-FROG.

Our hydrogen gas jet target, described in [61-63], was not cryogenically cooled in the present experiment because for λ=3.9 μm the critical density regime (N_{cr}~7×10^{19} cm^{-3}) was easily achieved with moderate gas densities. By adjusting the backing pressure of the 150 μm orifice diameter nozzles and the distance of the laser axis above

the orifice, we achieved tunable peak H_2 densities from 1.8×10^{18} to 8×10^{19} cm^{-3}, with near-Gaussian density profiles and FWHM widths d_{FWHM} ~ 250–1000 μm. When fully ionized, the peak target density in the laser path spans $0.05N_{cr}$–$2.2N_{cr}$ at λ=3.9 μm.

Neutral gas and plasma profiles were probed with λ=650 nm, 130 fs pulses from an OPA synchronized with the λ=3.9 μm pulses, and imaged by an *f*/2 achromatic lens telescope to a compact Nomarski interferometer [154]. A LANEX scintillating screen, located 7.5 cm beyond the gas jet and shielded from laser exposure by 100 μm thick aluminum foil, was imaged to a low noise CCD camera to capture full electron beam profiles (Fig. 3.1 (f)). The magnetic spectrometer consisted of a 500 μm slit 7.5 cm beyond the jet followed by interchangeable permanent magnets with effective field strengths of 0.065 or 0.013 T, providing spectra in the ranges 750 keV–6 MeV and 2–12 MeV, with the LANEX screen 17.5 cm beyond the jet (Fig 3.1 (g-h)).

3.3 Results

Electron acceleration above ~500 keV, the low energy detection limit of our beam profile monitor, is observed over a wide parameter range and is summarized in Fig. 3.2. The unifying theme of this plot is that acceleration occurs for self-focusing lengths less than the target width, $\ell_{sf} < \sim d_{FWHM}$, with the straightforward interpretation that electron acceleration requires self-focusing of the beam within the axial extent of the plasma in order to drive a plasma wake capable of self-injection. The accelerated electron bunches have a divergence of ~200 mrad for P/P_{cr} ~2, and show increasing divergence as P/P_{cr} increases. For $P/P_{cr} > \sim 10$ (for which $N_e > N_{cr}$), the electron beam profile exhibits the signature of relativistic multi-filamentation of the

drive pulse (modulational instability), which can also be inferred from interferograms (see Fig. 3.1 (k, l)). Near the P/P_{cr} threshold, beam profiles also exhibit a "halo" of accelerated charge at high divergence (~1 rad).

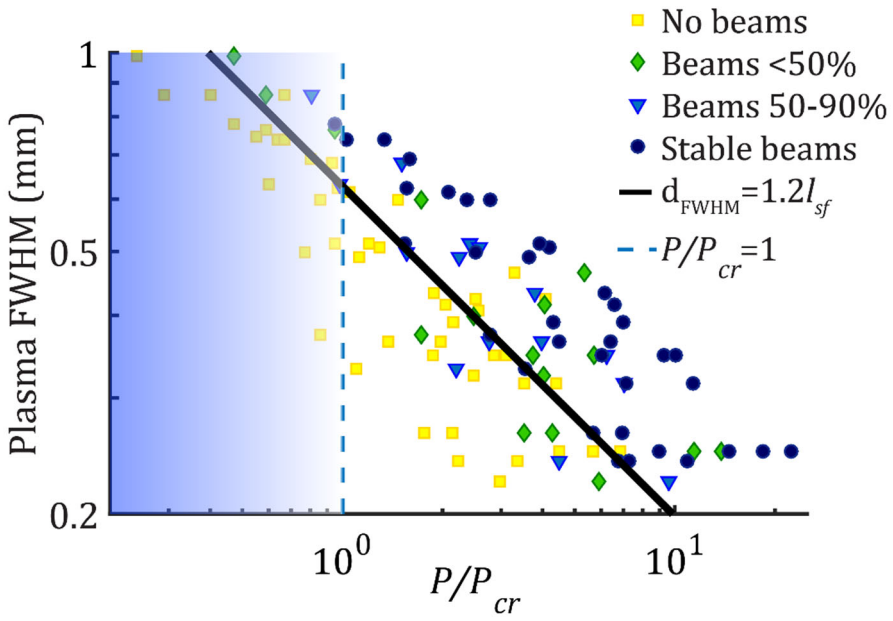

Figure 3.2. Plot demonstrating the onset of electron acceleration for a variety of target conditions. Results are grouped by the percentage of 20 shots which produced beams., where beam presence is defined as >2 pC of whole beam charge >0.5 MeV above background noise on an individual shot. The solid line indicates the threshold relationship between the gas jet width d_{FWHM} and the self-focusing length, while the shaded area and dotted line mark the range of P/P_{cr} where appreciable self-focusing is not expected.

Electron spectra averaged over 20 shots for selected conditions are shown in Figure 3.3, and display a Maxwellian energy dependence, with effective temperatures ranging from ~0.5 MeV to >2 MeV. Peak energies extend beyond 12 MeV (the resolution limit of the detector). Under all conditions, charge increases with increasing pump energy.

The effect of the plasma density, and hence critical power, is illustrated in Fig. 3.3 (a), which shows accelerated electron spectra as a function of density for a 23 mJ pump incident on a gas target with d_{FWHM} ~700 μm. Electron charge increases quickly as the peak density increases to $0.2N_{cr}$, but then drops as the density is further increased. For the same laser energy, 23 mJ, Fig. 3.3(b) shows total charge per steradian accelerated above 2 MeV vs. plasma density for various jet widths. It is seen that the plasma density giving peak accelerated charge depends on the jet width. Beyond this peak, charge and effective electron temperature both decrease. This suggests that for each jet width, a particular density (and value of P/P_{cr}) optimizes the acceleration process. Comparing the optimal (highest charge) cases at each jet width, we find that all share a ratio of jet width to self-focusing length of d_{FWHM}/ℓ_{sf}~2 (with all accelerated beams lying in ~$1.2 < d_{FWHM}/\ell_{sf} <$ ~3). Near the length onset threshold d_{FWHM}/ℓ_{sf}~1.2 we also observe highly structured spectra that show quasi-monoenergetic peaks on top of the Maxwellian spectrum for individual shots (e.g. Fig. 3.1 (h)), in line with previous work [61].

Applying the divergences measured from full beam profiles to the electron spectra, we estimate a maximum of ~850 pC of charge above 650 keV (average of 20 shots), with ~300 pC above 2 MeV. This is consistent with directly integrating the full beam profile and using an estimate of the energy-dependent LANEX response [155,156], which gives an approximate maximum beam charge ~1 nC at energies >500

keV. Using this full beam estimate, it is again seen that the total accelerated charge peaks for d_{FWHM}/ℓ_{sf}~2.

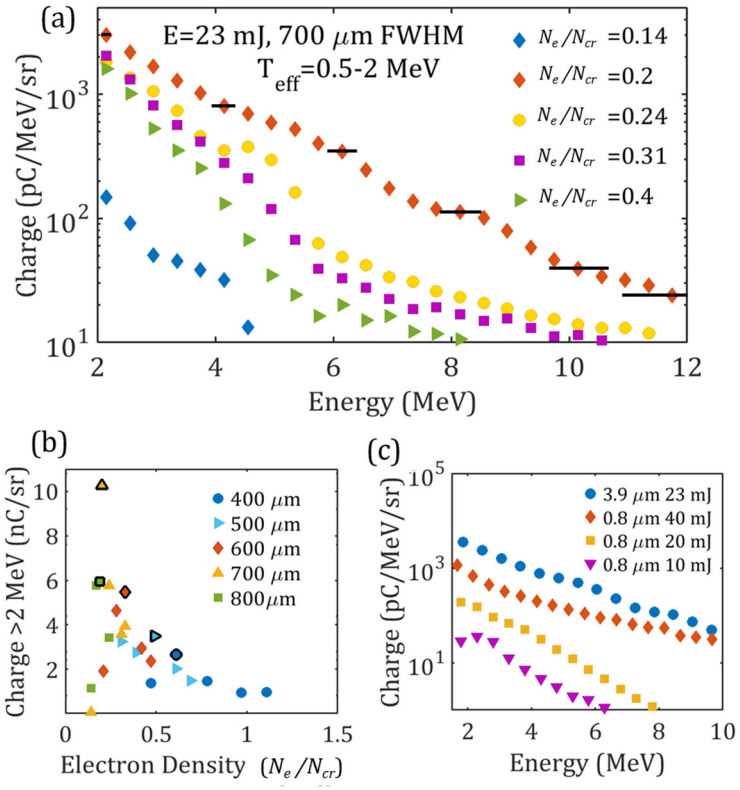

Figure 3.3. (a) Electron spectra for jet d_{FWHM} ~700 μm, 23 mJ pump and varying peak electron densities; bars indicate energy uncertainty, as determined by ray tracing. (b) Charge accelerated above 2 MeV by a 23 mJ pump vs. peak density for a variety of target widths. For each target width, the maximum value of charge accelerated is outlined in black. (c) Optimized electron spectra from current λ=3.9 μm experiment compared to spectra from λ=800 nm experiment reported in [61], both for N_e~0.25N_{cr}. All λ=3.9 μm spectra are averaged over 20 shots.

On shots measuring accelerated electrons, we also observed a bright, visible "flash", which experiments at λ =800 nm identified as coherent radiation emitted by accelerated electron bunches during laser assisted injection [61,77]. An example side-collected spectrum of this radiation for N_e~0.5 N_{cr} is shown in Fig. 3.4.

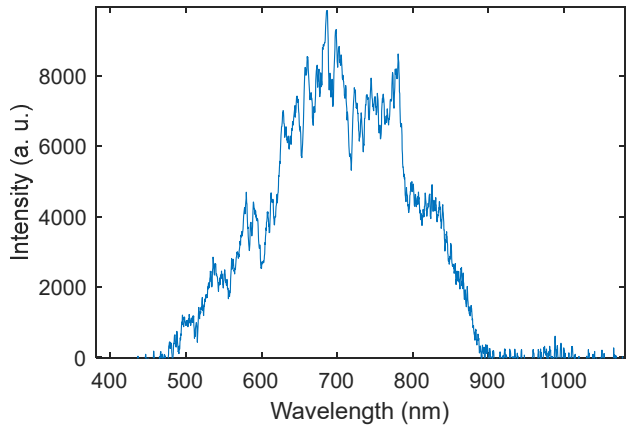

Figure 3.4. Side-collected spectra (average over 20 shots) emitted during injection and acceleration of electrons at $N_e \sim 0.5\, N_{cr}$. The sharp drop in spectral content at 780 nm is an artifact due to spectral coatings on collection optics.

The sharp local drop at 780 nm is an experimental artifact due to broadband visible antireflection coatings on the experimental chamber window through which flash spectra were collected. Due to experimental constraints, it was not possible to collect spectra over a full scan of jet and laser parameters. The spectral content of this "flash" is related to the acceleration gradient experienced by injected charge, with upper and lower limits set by the plasma density and the width of crests in the plasma wave [77]. Modulations on the spectrum are predicted to occur at a spacing given by the plasma frequency due to regularly spaced electron injection at a single axial location [77]. Here, such modulations are not well resolved, since at high P/P_{cr} ratios, multi-filamentation results in injection at many locations.

3.4 Discussion

An explanation for the correlation of charge with self-focusing length, as well as the appearance of quasi-monoenergetic peaks, is shown in Fig. 3.5 (a). For

simplicity, the density profile (dashed curve) is imagined as several stepped regions where a fixed energy pulse is either below or above the critical power. The self-focusing length ℓ_{sf} defines an effective collapse location in one of these regions, which will move forward (toward the source of the laser) as the critical power is increased. At this collapse point, essentially a secondary nonlinear focus, the local plasma density determines further laser-plasma evolution and acceleration. For collapse occurring in a region of low density plasma where $P/P_{cr} \ll 1$, there is no longer sufficient plasma to drive self-focusing or maintain self-guiding, and the nonlinearly focused beam quickly diffracts before self-modulation can drive injection into the laser wake, as depicted by the sketch of the expanding beam on the far right. As the collapse moves to areas of higher density (either through an increased jet width or shorter ℓ_{sf}), a weak nonlinearity can partially guide the focused beam (center beam sketch), leading to self-modulation. At a threshold collapse point, wave breaking occurs and a limited amount of charge will be injected and accelerated before the beam starts to diffract and injection stops, leading to quasi-monoenergetic peaks of charge accelerated in the laser's linear wakefield. Collapsing earlier in the jet increases the guiding distance (left beam sketch), and when overlapped with the rear density gradient leads to increased charge due to downramp injection [76]. For collapse within the peak of the jet, charge may decrease with the onset of relativistic multi-filamentation and reduced downramp injection, while shorter dephasing lengths [17,18] may reduce the effective temperature.

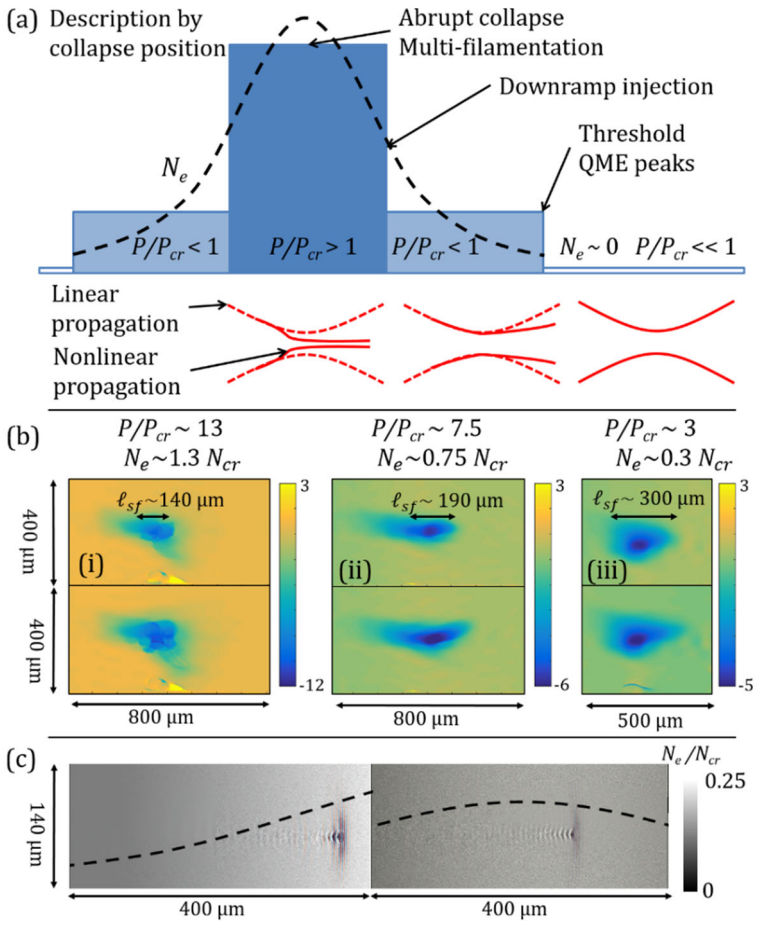

Figure 3.5. (a) Qualitative behavior of electron beams for nonlinear collapse at different locations within the plasma density profile. Self-guiding only occurs if the pulse collapses in areas where $P/P_{cr} > 1$, and will diffract elsewhere, though with partial confinement for $P/P_{cr} \lesssim 1$. The guiding length affects electron injection, leading to a scale length threshold and charge increases for focusing on the density downramp. (b) Drive laser-induced plasma phase images (average of 20 shots) during (top) and after (bottom) interaction with jet widths (i-ii) d_{FWHM} = 450 µm or (iii) d_{FWHM} =300 µm. Overlaid arrows indicate the calculated self-focusing length for the interaction conditions. (c) Particle-in-cell simulations illustrating density-dependent collapse location for jet d_{FWHM} =700 µm, and peak densities of 0.4 N_{cr} (left) and 0.25 N_{cr} (right). The pulse (overlaid) collapses on the upramp in the first case, while collapsing just past the peak of the jet in the second case.

The larger plasma structure and lower plasma density than in previous studies at $\lambda = 800$ nm [61] enables more detailed transverse interferometric probing of the plasma generated by the wakefield drive pulse, using the λ=650 nm probe and a 2-D

phase unwrapping algorithm [157]. By adjusting the delay between probe and drive pulse, we recorded time resolved images of the relativistic self-focusing process for a variety of target conditions. Figure 3.5 (b) shows averaged phase images for two jet widths (300 μm and 450 μm) and three different interactions (P/P_{cr} ~3, ~7.5 and ~14) at two probe delays: ~500 fs after the drive pulse enters the jet and after the pulse has completely left the jet. Each panel indicates the calculated value of ℓ_{sf} for its conditions, and it is seen that the phase images of the interaction follow the same trends.

We note that earlier work with a pressure boosted jet [60] imaged dynamics of a self-focusing pulse in a near-critical interaction, but for P/P_{cr} >200. As a result, the pulse abruptly collapsed on the density up-ramp and deposited its energy into a population of divergent, thermal electrons driving an opaque shock structure. Here, owing to the larger values of ℓ_{sf}, we observe details of a more gradual collapse accompanied by electron acceleration to MeV energies.

As seen in Fig. 3.3 (c), the charge in λ=3.9 μm laser-driven electron beams at optimized conditions significantly exceeds charge in beams driven at λ=800 nm [61]. When the comparison is for laser pulses of the same energy (20 mJ), the charge increase factor is ~20, and ~100 for the same peak power (200 GW). As discussed in Sec. 1.3, the number of accelerated charges for a fixed power P and a_0, fraction of critical density N_e/N_{cr}, and number of laser cycles scales as $N_{acc} \propto \lambda$, which would predict a 5× charge enhancement, far lower than observed. Due to the observed importance of the self-focusing length, it is possible that the jet width in the previous λ=800 nm

experiment was not optimized for maximum charge, particularly since achieving comparable fractions of critical density required operating closer to the jet [63], with resulting limits on the achievable scale length.

3.5 Simulations

We now discuss simulations of the current experiment and possible future experiments. Because the physics of LWFA is so nonlinear, complex, and dominated by kinetic effects, fluid-based codes are useful only for weakly relativistic interactions, and are, in general, inadequate for simulating most LWFA experiments. Particle-in-cell (PIC) codes, which solve Maxwell's equations on a discretized grid and then apportion plasma species into "macroparticles" to reduce numerical complexity, are the primary tool to simulate laser plasma accelerators [158-162]. Simulations were performed with the particle-in-cell codes EPOCH [158] and TurboWAVE [159] for a variety of pulse parameters. Simulations of a 20 mJ, λ=3.9 μm drive pulse and a 700 μm FWHM target with peak densities in the range $0.1 - 0.5\, N_{cr}$ were consistent with experimental results, producing few MeV electron beams with total charge ~100 pC. Frames from two different simulations are shown in Fig. 3.5 (c), demonstrating the shift in collapse position for 0.25 N_{cr} and 0.4 N_{cr} targets, respectively.

To enter the regime of resonant wakefield excitation at $a \gtrsim 1$ for our current pulse energy of ~20–30 mJ, our λ=3.9 μm pulse would need to be compressed from 90fs to ~30fs. Nonlinear compression schemes have been proposed and demonstrated to accomplish this [24,25], as mentioned in Chapter 2. Figure 3.6 shows simulations for such self-compressed pulses (30 fs FWHM). Pulses are focused to a ~9 μm FWHM

spot in a 0.02 N_{cr} plasma slab 100 μm wide, for a vacuum peak intensity of ~4×10^{17} W/cm^2 (a_0~2). Figure 3.6 (a) shows the electron density after the pulse has passed through the jet, showing cavitation, or complete expulsion of plasma electrons in the wake of the pulse, indicative of the nonlinear "blowout" regime. Panel (b) shows the electron phase space, with controlled injection in the first few plasma buckets leading to energy peaks at ~20 MeV (~0.1 fC of charge) and ~6 MeV (~0.1 pC) in the final accelerated beam. In this case, successive plasma buckets also experience wave breaking injection, leading to a large low energy tail in the final energy spectrum shown in Fig. 3.6 (c).

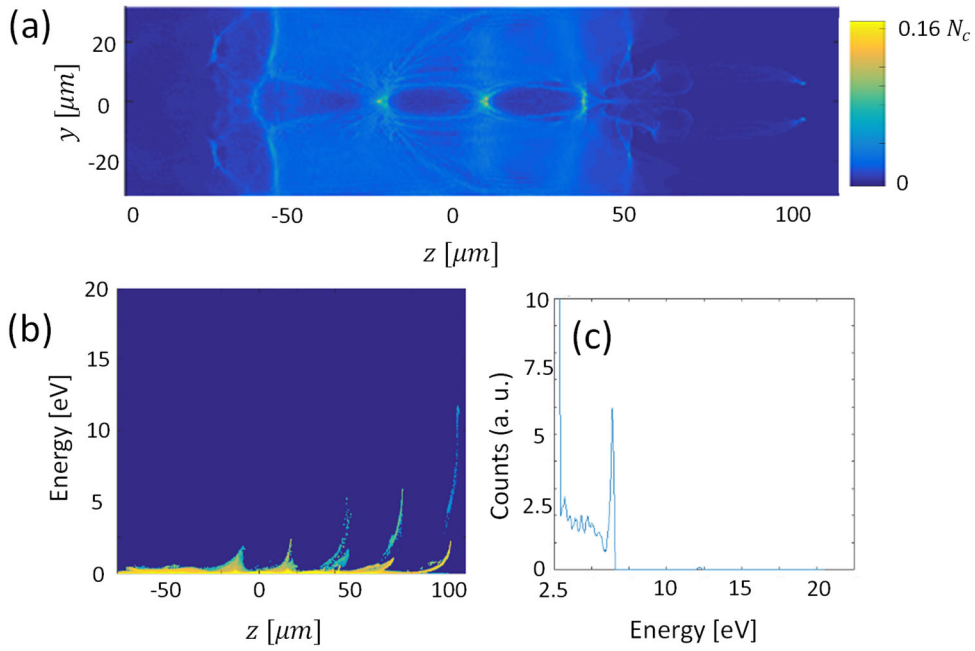

Figure 3.6. Simulations of LWFA driven resonantly by a ~20 mJ, 30 fs $\lambda = 3.9$ μm pulse in a 0.1 N_{cr} plasma slab 100 μm wide (a) Snapshot of the electron density profile after the laser and first accelerated bunch have left the jet, showing a strongly cavitated wake in the jet. (b) A snapshot of the electron beam phase space (log scale) showing injection over successive buckets. This leads to a low energy tail in (c) the electron spectrum, in addition to monoenergetic peaks at 6 and 12.5 MeV.

3.6 Future work enabled by mid-IR LWFA

We now discuss several unique opportunities for mid-IR driven LWFA. As discussed in Sec. 1.3, the relativistic dynamical equations underlying LWFA scale so that pulses of the same peak power, but with $\lambda \to \alpha\lambda$, laser intensity $I \to I/\alpha^2$, spot size $w_0 \to w_0\alpha^2$, pulse length $\tau \to \alpha\tau$ and acceleration distance $L \to \alpha L$ in a target of fixed N_e/N_{cr}, produce self-similar wake dynamics, for acceleration to the same final energy and an increase in bunch charge $n_a \to \alpha n_a$. As such, the 30 fs (~2.5 cycles), 20 mJ pulses we considered in Fig. 3.6 directly scale with few-mJ, few-cycle (~2-5 mJ, ~5 fs) λ =800 nm LWFA drivers operating near the critical density [163-170]. The exciting prospect of these accelerators depends on the scaling of the bubble size and total energy required as pulse lengths decrease: in the nonlinear blowout regime, both the beam focal spot and pulse length should be matched to the plasma bubble size, $w_0 \sim c\tau \sim \lambda_p/2$, while maintaining $a_0 \geq 1$. Thus for a given value of a_0, the energy required $\sim I w_0^2 \tau$ scales as $w_0^2\tau \propto \tau^3$.

Recently, use of such few mJ, few-cycle driver pulses has resulted in acceleration, at 1 kHz repetition rate, of quasi-monoenergetic beams with energy up to ~6 MeV using N_2 gas jets [164,165], and up to 15 MeV using near critical density H_2 gas jets [166,167]. Near critical density is needed because the experiments are in the bubble regime, $w_0 \sim c\tau \sim \lambda_p/2$, for $\tau \sim$ 5 fs pulses. However, effects from dispersion and resonant instabilities near the critical density are not well understood and are difficult to resolve in simulations. These few-cycle driven accelerators can also show unique effects, such as dependence on the carrier-envelope phase or the onset of hosing

instabilities [168-171]. Since these novel accelerators excite few-micron sized bubbles, they are difficult to probe with visible and near-infrared lasers. Scaled experiments with few-cycle MIR/LWIR lasers (~5× larger bubbles) could thus provide important information about wake dynamics in this new regime, since synchronized visible/infrared probes could more easily resolve the relevant sizes (~10-20 μm) and densities (~$0.02N_{cr}$ at optical frequencies).

In a different regime, scaling up the "standard" LWFA regime in the mid-IR, characterized by 25 TW–1 PW drivers and bubble sizes of tens of microns in the NIR, is also promising for future experiments. For scaled mid-IR/LWIR systems at the same peak power, bubble sizes of hundreds of microns enable external injection of conventionally accelerated electron beams into the LWFA structure [84,85,172] as dictated by existing state-of-the-art RF linac bunch lengths (tens to hundreds of microns [84,173,174]), or easier coupling between multiple laser acceleration stages [86]. Such external injection is one proposed method to improve laser accelerator quality, since emittance, or beam spread, is preserved from the initial high quality beam, while LWFA provides a high acceleration gradient.

Another unique aspect of a mid-IR driver is the additional control over ionization. In the present experiment, pulses were focused to similar values of a_0 compared to previous high density self-modulated experiments, which observed acceleration in He for >5 mJ, λ =800 nm pulses [62]. However, we did not observe any acceleration in He, despite peak gas densities comparable to runs with H_2. We attribute this change to ionization induced defocusing of the pump: since our peak

intensity is only a factor of ~10x above the barrier suppression threshold for the second ionization stage of He, more plasma is created on axis at the focus than off axis, resulting in defocusing of the pump beam before it can nonlinearly focus. This distinction between the effects of intensity and a_0 is also key to proposals for low emittance dual-wavelength laser wakefield acceleration [92]. In this scheme, a high a_0 MIR or LWIR beam excites a wake in a pre-ionized plasma, but has insufficient intensity to drive ionization injection of higher charge states. A secondary UV/VIS beam is then focused much more tightly within the wake to a high intensity, but a low value of a_0, so as to inject electrons without perturbing the wake. This combination ensures highly localized injection separate from the properties of the drive field, resulting in high quality, ultralow emittance beams [92].

In summary, we have observed MeV-scale electron acceleration driven by ultrashort mid-IR pulses for the first time and demonstrated the importance of the relativistic self-focusing length in enabling electron acceleration. Operating in the mid-infrared enables near- and above-critical density interactions with a simple gas jet and sets the stage for schemes that may require more tailored near-critical density profiles. In the LWFA bubble regime, mid-IR drivers generate larger bubbles, enabling more detailed imaging and easier synchronization with secondary laser pulses or electron bunches. In particular, probing physically larger wakes excited with few-cycle MIR pulses in near-critical plasma could provide insight into wake dynamics in this regime, which are hard to observe when scaled to NIR drivers.

Chapter 4: Remote detection of radioactive material using mid-IR laser-driven avalanche breakdown

4.1 Methods of standoff radiation detection

Assessing the localized presence of radioactive materials at large standoff distances by directly detecting their decay products is severely limited by geometry. While advanced versions of conventional gamma ray detectors are able to identify and locate radioactive material with source-detector distance R up to 100 m [175-177], there is rapid gamma flux drop-off beyond this distance owing to combined R^{-2} dependence and gamma ray absorption in air. In addition, these detectors are large and must sample at multiple locations to determine the radioactive source location. Most schemes for remote detection of radiation therefore rely on probing the local environment near the source, either by deploying remotely controlled or networked sensors [178-182], or by detecting chemical markers of the source with laser-induced-breakdown spectroscopy [183-185], THz spectroscopy [186,187], Raman spectroscopy [188,189], multi- and hyperspectral imaging [190], or Fourier transform infrared spectroscopy [191]. However, these optical methods require an unobstructed line-of-sight view of trace amounts of the radioactive substance outside any shielding, and thus could be defeated by careful source handling and cleaning of container surfaces.

Rather than relying on chemical traces of the source material itself, several recent approaches aim to detect the elevated levels of free electrons and negative ions in the air near a shielded radioactive source using a laser-driven electron avalanche

[192,193]. The concentration of these radiation-induced charged species is far too low for direct detection, with densities in the approximate ranges $\sim 10^{-2} - 10^{1}$ cm^{-3} for electrons and $\sim 10^{4} - 10^{7}$ cm^{-3} for ions [128]. However, the use of laser-driven avalanche breakdown, which starts from a single electron and exponentially increases the local electron density to detectable levels, can be viewed as an analogue of the detection of single photons by a photomultiplier tube, enabling sensitivity to these ultralow densities.

As discussed in Sec. 1.4, electron avalanche ionization is initiated when seed electrons are heated collisionally by intense electromagnetic wave-driven elastic collisions with background neutrals, converting coherent oscillatory electron motion into random velocities, or heating. Once electrons gain sufficient energy, they can liberate additional electrons through inelastic ionizing collisions with air molecules. If the laser-induced heating is sufficient to overcome losses such as electron cooling, attachment, and diffusion, the electron density will increase exponentially until it saturates. In the case of an avalanche-based detection scheme, the initial free electrons are generated by the ionization of air by decay products of radioactive sources.

The earliest detection concept based on avalanche ionization envisioned the use of a mm-wave or THz source to drive the breakdown seeded by free electrons in the vicinity of the radioactive material [192], and was the subject of simulation work [194-196] and a recent experiment [134]. Given the limited practicality and availability of high power mm-wave and THz sources, other proposals and experiments examined the use of visible and near-IR laser drivers. Detection with this wavelength range is limited

by the deleterious competing effect of multiphoton ionization (MPI) as discussed in Sec. 1.4.3, which generates a population of free electrons early in the laser pulse that overwhelms the seed population induced by the radioactive source.

Here, we present two experiments [37,38], demonstrating picosecond mid-IR laser pulses are exceptionally well suited as an avalanche driver for radioactive source detection. Free electrons, liberated by interaction of source decay products with air, quickly attach to oxygen to form O_2^- ions, with a bond energy of ~0.45 eV, which then forms the basis of subsequent air chemistry [128,193,197]. Early in the mid-IR pulse, the electrons are re-liberated by the high ionization rate of O_2^- and other negative ions, and then seed a subsequent avalanche. A variable initial seed density of negative ions, determined by the activity and location of the radioactive source, introduces a commensurate temporal shift in the onset of breakdown. We measure this timing shift by either measuring the attenuation of a chirped co-propagating near-infrared probe pulse [37], or measuring the backscatter of the mid-IR probe pulse with a single-shot, high sensitivity mid-IR spectrometer [38].

As shown in Sec. 1.4.4, for a 50 ps laser driver and initial seed densities $<\sim 10^{10}$ cm^{-3}, avalanche breakdown sites seeded by single electrons remain isolated owing to very limited electron diffusion during the pulse [132]. By imaging and counting these individual breakdowns in the laser focal volume, we also directly determine the density of negative ion seeds down to $\sim 10^4$ cm^{-3}, limited by breakdowns likely seeded by aerosols or dust. Directly counting breakdowns enables absolute benchmarking of three diagnostics employed here for remote detection. More generally, it enables

measurement of transient, ultralow electron densities far below those measurable through other methods. In Chapter 5, we describe experiments further leveraging this technique to measure record low laser-generated electron densities.

4.2 Experimental setup and diagnostics

Experiments were performed with chirped, high energy mid-IR laser pulses (50 ps FWHM, near flat-top temporal profile, 15-35 mJ, $\lambda = 3.6 - 4.2$ μm) [149]. The first experiment [37] focused pulses at varying f-numbers to intensities in the range $\sim 1 - 3$ TW/cm^2, and tracked breakdowns through total pump backscatter and the attenuation of a chirped probe beam, as described below. However, an uncorrected camera nonlinearity used in focal spot measurements led to an over (under) estimate of focal spot size (intensity) that was difficult to precisely correct after the fact. As such, we primarily present results from the second experiment [38], which had superior focal spot measurements and breakdown diagnostics, but refer to important results from the first. In the second experiment, depicted in Fig. 4.1, pulses were focused by a 1 m spherical mirror to a FWHM focal spot of ~140 μm as measured by an InSb camera, providing a proof of principle of multi-meter standoff detection. The focal spot changed slightly as pulse energy was increased, resulting in peak intensities ranging from 1.5 to 3×10^{12} W/cm^2 (1.5–3 TW/cm^2). The laser-driven avalanches were monitored by 3 'field' diagnostics that one might use in a practical detection setup: backscattered spectra of the chirped pump pulse, relative backscattered pump energy, and collection of the visible breakdown plasma emission. These were then benchmarked by direct

imaging of the full breakdown volume. All these measurements are described in more detail below.

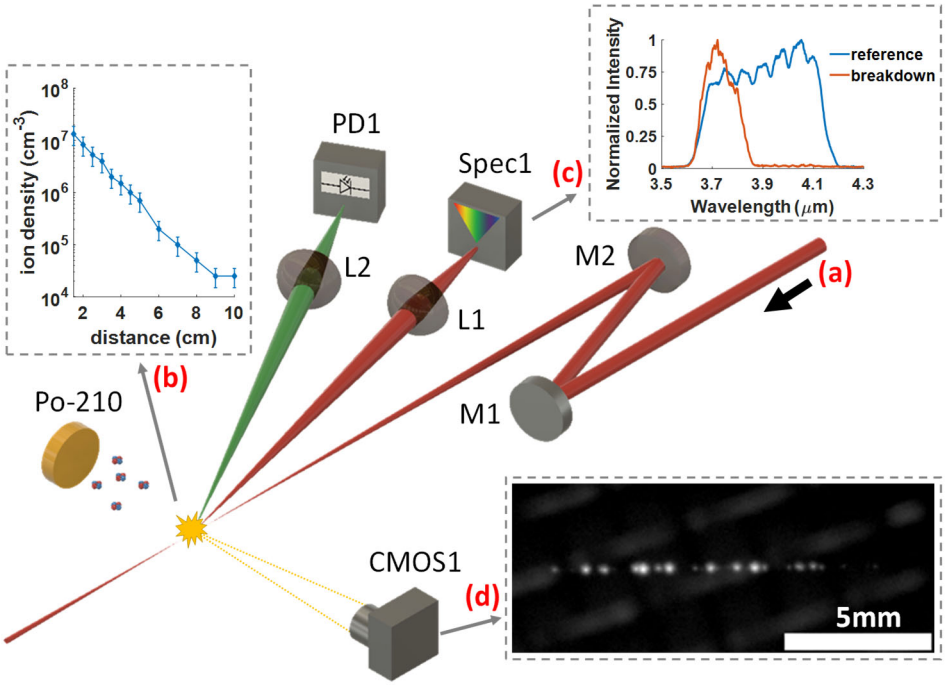

Figure 4.1. Experimental setup. (a) A chirped, 50 ps (FWHM) λ=3.6-4.2 μm laser pulse is focused by a 1 meter focusing mirror, M2, to a focal spot near a 5 mCi Po-210 source emitting 5.3 MeV α-particles, driving electron avalanche. (b) O_2^- ions formed in the vicinity of the α-source provide seed electrons for the avalanche, with total negative ion concentration vs distance from the α-source shown in the plot. (c) Backscattered mid-IR light is collected by lens L1, located 1 meter from the breakdown, into a home-built mid-IR imaging spectrometer, Spec1, with a sample backscatter spectrum and reference laser spectrum shown. Visible plasma emission is collected by lens L2 onto an amplified silicon photodiode PD1. A notch filter rejected stray light from the 1064 nm OPCPA pump laser. (d) Plasma emission from the breakdown is also imaged onto camera CMOS1, with a sample image shown.

The focused pulses drive avalanche breakdowns at a 20 Hz repetition rate in ambient air irradiated by a 5 mCi Po-210 spot source emitting 5.3 MeV α-particles (NRD Nuclespot). The distance between the source and the laser focus, d_{s-f}, was varied by translating the source on a rail. To prevent ions from a previous breakdown plasma seeding a successive avalanche, dry air was flowed at ~60 cm/s across the focal region. The steady state negative ion density induced in air by the Po-210 source was

measured using a Gerdien condenser ion counter (AlphaLab), with a plot of density vs. distance from the source shown in Fig. 4.1(b). The minimum distance of ~1cm is set by the ion counter geometry. A mechanical shutter capable of blocking all α-particles is affixed to the source for a portion of experimental runs to demonstrate on/off responses to radioactivity. Pump light backscattered from the breakdown plasma is collected at ~*f*/80 at 12° from the laser axis by a lens (L1) located 1 m from the plasma, and directed into a single-shot mid-IR imaging spectrometer (Spec1) with a liquid nitrogen cooled InSb camera (IRCameras IRC806) in its image plane, as discussed in Sec. 1.2.6. This unique diagnostic is used to measure the avalanche onset delay and the relative amount of backscattered mid-IR pump energy. It is able to capture single shot backscatter spectra and is far more sensitive than spectrometers based on a PbSe array. Examples of the incident positively chirped pump spectrum and the spectrum backscattered from an avalanche breakdown are shown in Fig. 4.1(c). Since the pump pulse is positively chirped, providing a frequency-to-time map, the air breakdown evolution is encoded in its backscatter spectrum. Backscatter from a seed-initiated breakdown is detectable on the mid-IR spectrometer when the local electron density reaches ~10^{18} cm^{-3}, based on considerations of plasma size and detector sensitivity as derived in Appendix A.1. The spectrometer was calibrated by measuring high order grating spectra of a 532 nm laser diode, indicating that the 50 ps pulse's spectrum was spread over ~250 pixels on the spectrometer's InSb camera detector, for a temporal resolution of ~0.2 ps/pixel. In order to improve extraction of breakdown onset times, spectra were smoothed with a 10 point moving average (reducing temporal resolution

to ~2 ps). The longest wavelength (and correspondingly, earliest point in time) where the backscattered spectrum exceeds the detector noise threshold of ~2 counts is defined as the breakdown time. Time advance is then determined by comparing the breakdown time to the end of the pulse, which we define as the point when the pump intensity drops to 10% of its peak value (λ=3.65 μm). Visible line and continuum emission (300-1000 nm) from the breakdown plasma is collected at *f*/18 at 16° from the laser axis by a lens (L2) located 90 cm away from the plasma and focused onto an amplified Si photodiode (PD1, Thorlabs PDA100A2). Images of the plasma emission in the breakdown volume are also collected at 90° from the laser axis by a low noise CMOS camera (CMOS1, Thorlabs Quantalux), with an example image shown in Fig. 4.1(d). The first experiment used a small amount (~μJ) of the negatively chirped near-infrared signal beam (1.4-1.5 μm) as a forward-directed probe for a similar timing measurement; there, we tracked the time at which the probe was attenuated by 20% compared to a reference spectrum. For that experiment, we also measured total pump beam backscatter on a PbSe photodetector (Thorlabs PDA20H), but did not track visible plasma emission.

4.3 Negative ion formation and density

All radioactive sources of interest, whether α, β, or γ emitters, result in free electron generation from the ionization of ambient air. Liberated electrons thermalize and then efficiently attach to neutral O_2 within tens of nanoseconds [197] to form O_2^-, initiating a chain of air chemistry reactions that generates more tightly bound ions such

as NO_2^-, O_3^-, O^-, OH^-, and the terminal ion NO_3^- [198,199]. Due to its low electron detachment energy of 0.45 eV [200], O_2^- is a readily accessible source of additional electrons to initiate breakdown. Assuming a steady source of ionizing radiation from a radioactive source, a simple rate equation model that ignores subsequent ion chemistry [128] gives the pre-avalanche ratio of free electron density to O_2^- density, $N_e/N_{O_2^-} \approx 5\beta/\eta N_{O_2} \approx 10^{-6}$, where β is the loss rate of O_2^- due to collisions with neutral air molecules, η is the rate of attachment of electrons to O_2, and N_{O_2} is the density of atmospheric oxygen. Thus we expect the negative ion density to greatly exceed the free electron density and dominate avalanche seeding.

For the Po-210 foil source, the negative ion concentration is highest within the α-particle stopping distance (continuous-slowing-down approximation (CSDA)) in air of ~3.5 cm from the source [201]. With the Gerdien condenser ion counter, we measure total negative ion densities from ~10^7 cm^{-3} down to ~10^4 cm^{-3} in moving ~10 cm away from the α-source, as shown in Fig. 4.1(b). With the α-source blocked, the ion counter measures background ion densities ~10^2-10^3 cm^{-3}. We note that the ion counter cannot distinguish among different species of negative ions, and it has a ~1 cm wide intake port fed by weak fan-driven air flow that smears out any ion density gradients present. As such, we use the ion counter measurements as an estimate of the trends in total seed ion density. A corresponding theoretical estimate of the initial negative ion density can be made given the source activity, the range of α–particles in air, and the average energy needed to create an electron-ion pair (the "W-value"), from

which an ionization rate can be determined. The W-value for a Po-210 α–particle in air is ~35 eV, such that a single decay will produce ~10^5 electron-ion pairs [202]. Given a CSDA stopping range of ~3.5 cm and the planar source size of 1.7 cm, half of the decay products will be emitted from the foil (2.5 mCi ~ 10^8 decays/second) in a volume of ~150 cm^3. This predicts an ionization rate of ~7×10^{10} $cm^{-3}s^{-1}$, which is ~10^9 times higher than ionization rates from background radioactivity from cosmic rays and ambient sources such as radon [128,193]. Solving the simplified (O_2^- ion only) steady state rate equations presented in [128] with this ionization rate gives an O_2^- ion density $\geq10^8$ cm^{-3} and a free electron density of ~10^2 cm^{-3}. Ion densities are likely lower in practice due to ion diffusion, air convection, and energy lost by the α- particle as it leaves the foil source, suggesting reasonable agreement with the densities measured above.

4.4 Negative ion detachment

In the focal volume, O_2^- ions, with a binding energy of 0.45 eV, are detached early in the mid-IR pulse, providing a seed source for subsequent electron avalanche. Determining the exact detachment rate is difficult, but calculations of two photon rates [203] and tunneling calculations [50] suggest full ionization occurs within ~1 ps at intensities ~1 TW/cm^2. The more tightly bound negative ions produced through air chemistry (NO_3^-, NO_2^-, O_3^-, O^- and OH^-) [198,199], which have binding energies of $1.5-4$ eV [204], will experience lower rates of photoionization early in the pulse, but full tunneling calculations assuming a Coulomb potential suggest ions with detachment energies ~$1.5-3$ eV will ionize over 10s of picoseconds for $I > \sim1$ TW/cm^2, while

the most tightly bound ion (NO_3^- , ~4 eV) will not ionize until $I > \sim 3$ TW/cm^2. We note, in general, that using more accurate atomic and molecular potentials for negative ions in the Keldysh theory would result in even higher detachment probabilities [205]. An important point is that MPI and tunneling rates of neutral atoms and molecules by the mid-IR pulse are negligible; tunneling ionization of O_2, is an extremely low probability process for intensities $\lesssim$3 TW/cm^2, with electron density yield of <1 cm^{-3} for a 50 ps, $I < 3\mathrm{TW/cm^2}$ pulse [39,50]. By contrast, our previous work using a near-IR laser (λ=0.8μm) found that 8-photon MPI of neutral O_2 generated a seed density which overwhelmed that generated by the radioactive source, making λ=0.8μm laser-driven avalanches insensitive to the presence of the source [131].

4.5 Effect of ion density and laser focusing on breakdown timing

Once seed electrons are present in the laser focal volume, avalanche breakdown can proceed only if the local laser intensity exceeds a threshold above which electron attachment, diffusion, and inelastic collision losses are overcome. A finite laser pulse duration increases the effective threshold significantly beyond what it would be for a CW beam, since the growth rate must increase in order to drive a detectable breakdown *before* the end of the pulse. As considered in Section 1.4.2, in the limit of short pulses (<1 ns), the breakdown threshold which leads to a detectable breakdown is approximately I_b (TW/cm^2)~$8 \times 10^2/p\tau\lambda^2$, where p is the pressure (atm) and τ is the pulse length (ps), giving $I_{th} \approx 1$ TW/cm^2 for our conditions. Exposed to this intensity or greater, individual free electrons initiate an avalanche which reaches a significant fraction of the laser critical density (N_{cr}=7.2×10^{19} cm^{-3} at λ=3.9 μm) before the end of

the pulse. Pump absorption and plasma heating then dramatically increase, leading to increased backscatter of the pump pulse and a strong, visible spark. For a Gaussian beam of peak intensity I exceeding a breakdown threshold I_{th} and focused to a spot radius w_0 , the total volume for which $I > I_{th}$ is

$$V_{th} = \frac{\pi^2}{3}\frac{{w_0}^4}{\lambda}\left[\frac{2}{3}(5+\hat{I})\sqrt{\hat{I}-1} - 4\tan^{-1}\left(\sqrt{\hat{I}-1}\right)\right], \quad (4.1)$$

where $\hat{I} = I/I_{th}$ [206]. Thus the number of breakdown sites $= N_i V_{th}$, where N_i is the seed density, will increase with seed ion density and/or intensity.

Breakdown timing is correlated with both peak intensity and seed density. As the peak intensity increases, the volume V_{th} where the intensity exceeds the breakdown threshold increases, increasing the probability that an electron will be liberated from an ion and initiate an avalanche. As seed density or volume increase further ($N_i V_{th} \gg 1$), these liberated electrons are more likely to occupy regions of high intensity, leading to a higher local temperature, an increased collisional ionization rate, and a faster breakdown.

4.6 Results

Avalanche breakdowns were detectable (signal-to-noise ratio SNR>1) in backscatter diagnostics for peak intensities above a threshold of ~1.5 TW/cm^2, in agreement with the estimate above.

4.6.1 On/off measurements

We first show in Fig. 4.2 the effect of opening and closing the radioactive source shutter. Plotted are the signals from our breakdown diagnostics for 1000 consecutive laser shots, with the shutter opening and closing every 50 shots. The laser focus is 2 cm from the source, with the beam propagating perpendicular to the source normal direction, as depicted in Fig. 4.1. Examining the plots of pump backscattered spectra (bottom panels of Fig. 4.2(a)), it is seen that as the peak laser intensity increases, earlier breakdown is manifested as the appearance of redder portions of the positively chirped pump spectrum For a few shots at every intensity (~2-3% of all shots in the experiment), a single, very bright breakdown site (~5× brighter than other breakdowns, as imaged by the CMOS1 camera) develops very early in the pulse (25-40 ps time advance), likely due to random seeding by dust in the focal volume, as explained further below. As intensity is further increased to 3 TW/cm^2, breakdown occurs intermittently in non-irradiated air (with shutter closed), due to seeding by the background concentration of negative ions, or by enhanced seeding from contaminants, also discussed below. Comparing the backscatter energy, plasma emission, and breakdown time advance signals on one plot, Fig. 4.2 (b) shows the on-off response at 2.25 TW/cm^2, where each point is rescaled by subtracting the median background (non-irradiated) response and then dividing by the median irradiated response. The left scale is normalized backscattered energy and breakdown plasma emission, and the right scale is breakdown time advance. The plot is truncated at 3× median values. We use the median rather than the mean for rescaling to avoid skewing by the breakdowns seeded

by dust. The plot shows that the total backscattered mid-IR signal and plasma emission exhibit more shot-to-shot variability (with standard deviations of 42% and 52% of the median value after excluding high scatter points) than the breakdown time advance (with a standard deviation of 21% of the median value).

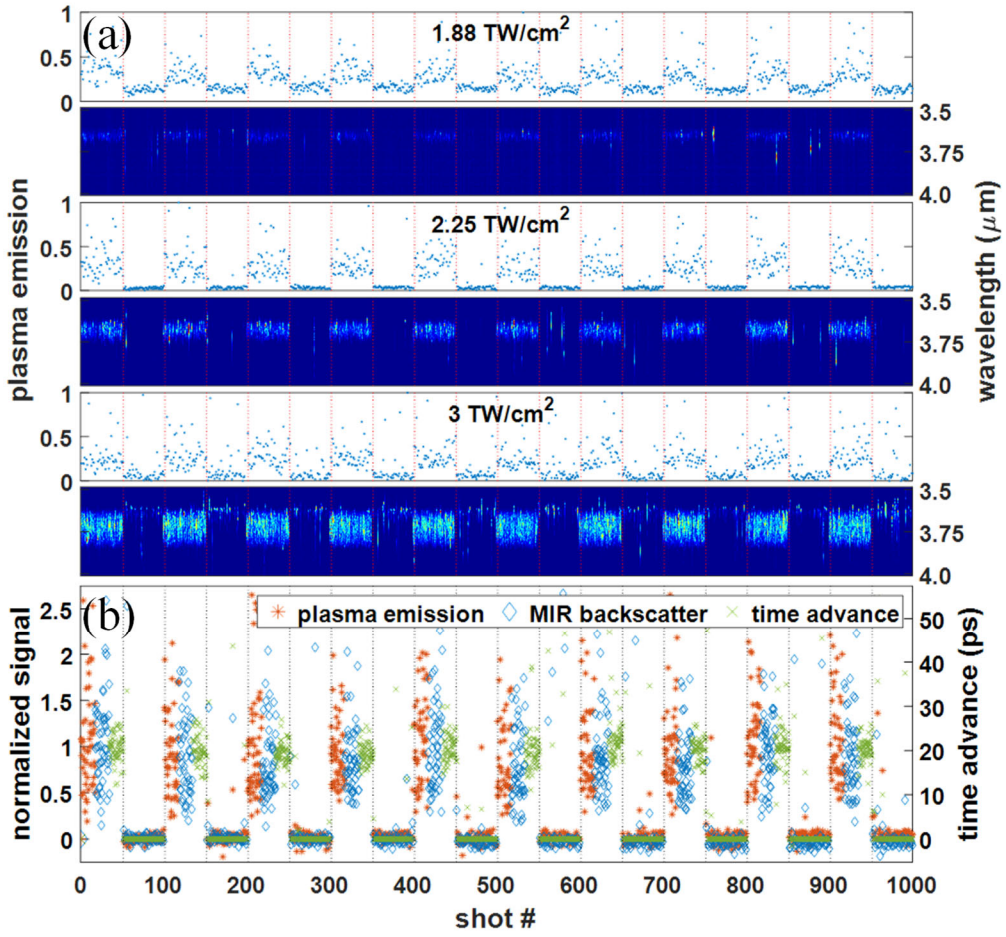

Figure 4.2. Real time measurements of radiation with data collected at 10 Hz (rate limited by data acquisition speed). (a) Single shot measurements of plasma emission and mid-IR backscattered spectra from the laser focus 2 cm from the α-source, with a shutter blocking/unblocking the radiation every 50 shots. For each intensity, the visible plasma emission is shown on the top panel, while spectra are shown on the bottom panel. (b) All three diagnostic signals plotted together for pump intensity of 2.25 TW/cm^2. For each data point, we subtract the median background (non-irradiated) signal and divide by the median irradiated response in order to directly compare the variation of each diagnostic. In order to compare the data scatter for the 3 channels on unblocked shots, the plot artificially reorders the shot numbers and squeezes 50 shots for each detection channel into adjacent ~13 shot-wide intervals.

Since the seed ion density 2 cm from the source is high enough for a large number of breakdown sites in the threshold volume (with some located at the highest intensity) such that the time advance is expected to be constant shot-to-shot, the different spreads in the three breakdown signals reflect their consistency as diagnostics of the seed ion density. For integrated mid-IR backscatter, the increased variability stems from propagation through randomly placed plasma sites: varying shot-to-shot backscatter interference between multiple scattering points in the breakdown volume, evident as fluctuating spectral fringes in the backscatter spectrum. These shot-to-shot fluctuations are increased by fluctuations in the shape and local density distribution of plasma. Likewise, the relationship between laser energy and plasma heating (and plasma emission), already nonlinear in the case of a uniform plasma, is also subject to local propagation effects: large shot-to-shot variations from scattering and refraction of the laser pulse from local plasma non-uniformities. The observed time advance, on the other hand, is largely decoupled from propagation in the vicinity of high density plasma: it is determined only by a single seed ion site near the region of highest intensity that breaks down the earliest, with the spectral content associated with that early backscatter unaffected by the interference and spectral fringing from the later backscattering from avalanche sites located in regions of lower pump intensity, which begin sizeable backscatter at later times.

4.6.2 Seed ion density scan

To compare the behavior of our avalanche signals over a range of radiation-induced seed densities, we scanned the α-source-laser focus separation d_{s-f} over 1 –

9 cm while keeping the intensity fixed. Figure 4.3 (a)-(c) presents the raw data from our three detection channels for a peak laser intensity of 2.25 TW/cm^2, while Fig. 4.3 (d) plots the mean and standard deviation of the measurements, again scaled between the maximum values of each detection channel and background.

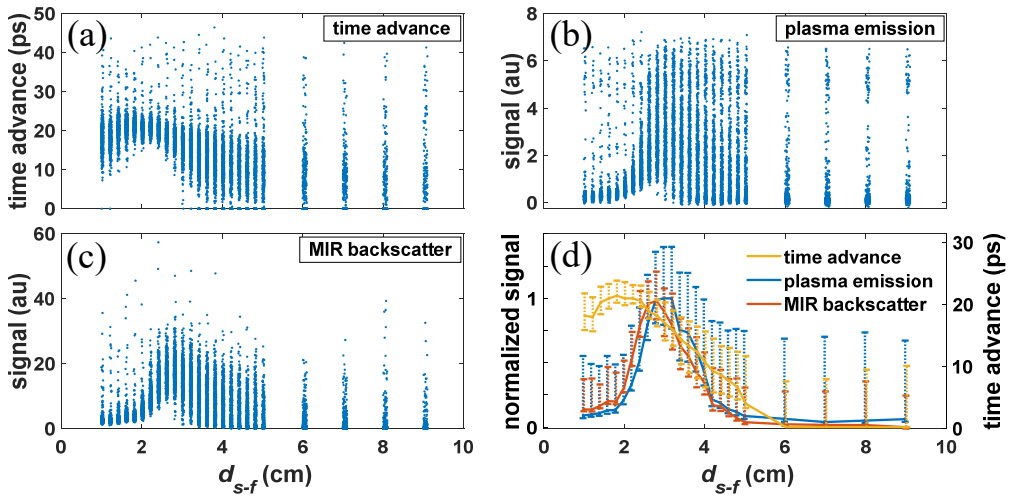

Figure 4.3. Single shot measurements of (a) time advance, (b) plasma emission, and (c) total MIR backscatter for a pump intensity of 2.25 TW/cm^2 as the distance from the α-source, d_{s-f}, is scanned over 1-9 cm. 500 shots were taken at each position, with 2 mm increments up to 5 cm, and 1 cm increments thereafter. The minimum d_{s-f} of 1 cm is limited by the Po-210 source holder. (d) Mean values at each location, with error bars denoting the standard deviation of data (calculated separately for values above and below the mean). As discussed later in the text, the suppression in plasma emission and total backscatter is caused by intensity clamping at high seed densities.

As seen in Fig. 4.3 (d), while the decreasing responses of the three detection channels are similar far from the source, near the source the response of the breakdown time advance channel is strikingly different from the other two. The breakdown time advance is roughly constant near the source because a seed ion is highly likely to be present near the region of highest intensity ($N_i V_{th} \gg 1$). For d_{s-f} beyond ~ 3 cm, the time advance decreases and becomes more variable, since only a few seed ions will be randomly distributed within the focal volume ($N_i V_{th} \gtrsim 1$). Far from the source

(d_{s-f} =5-9 cm), most shots do not record a breakdown advance (time advance=0, $N_i V_{th} \ll 1$), but those that do exhibit an advance that continues to decrease with d_{s-f}.

The backscattered pump energy and visible plasma emission, on the other hand, start at low levels near the source and then rise quickly to the peak near ~ 3 cm, falling to lower levels beyond that point. The lower levels of these signals near the source do not reflect an actual decrease in seed ion density, but rather the effect of pump laser scattering from multiple localized high density breakdown plasmas, as determined through benchmark imaging measurements below.

4.6.3 Breakdown imaging

Under all conditions of our experiments, breakdowns consisted of discrete, countable avalanche sites, due to the extremely limited electron diffusion from initial seeds over the length of the pulse. Individual seed ion locations in the focal volume were directly counted by imaging plasma emission from their associated avalanche sites (using camera CMOS1, as shown in Fig. 4.1(d), which shows a sample image). This enabled benchmarking of our three breakdown diagnostics using absolute seed ion counts. Collected images were processed to count breakdown sites and record the brightness of each one. A summary is presented in Fig. 4.4, showing in panel (a) the mean number of breakdown sites at each laser intensity and α-source-laser focus separation, d_{s-f}, averaged over 500 shots. Overlaid for reference is the ion density curve from Fig. 4.1(b), rescaled for plotting here.

The images show that the average number of breakdown sites increases both as the source is moved closer to the focal volume (higher ion density), and as peak

intensity is increased. At a given d_{s-f}, (and corresponding seed density), the breakdown count scales as $n \propto V_{th}(\hat{I})$ in Eq. (4.1). Fitting the measured breakdown counts (at d_{s-f} =1 cm) to $V_{th}(\hat{I})$, using I_{th} as a fitting parameter, gives I_{th} ~1.1 TW/cm^2, a value in line with similar fits at other values of d_{s-f} up to 4 cm (which give I_{th} = 0.9-1.3 TW/cm^2). This lower breakdown threshold (compared to backscatter diagnostics) is consistent with plasma imaging being able to detect much lower plasma densities due to its higher optical collection efficiency.

Over the range of intensities in Fig. 4.4, the volume for which $I > I_{th}$ is in the range V_{th} 2.7×10^{-5} to 2.7×10^{-4} cm^{-3}. This gives a peak seed ion density ranging from $2(^{+2}_{-1})\times10^5$ cm^{-3} at d_{s-f} =2.5 cm to ~10^4 cm^{-3} at d_{s-f} =4 cm, with the range given by variation in count measurements at the 5 different drive intensities. Comparison with the ion counter measurements, which peak at 10^7 cm^{-3} near the source, shows that the seed ion count is only a fraction of the number of negative ions detected by the Gerdien counter, although the seed ion density does track the total negative ion density. This behavior is consistent with the weakly bound O_2^- ions being part of a complex air chemistry chain which ends in more chemically stable terminal ions. While electrons may not detach from these more tightly bound ions in time to contribute to the breakdown [198,199], there are several reasons to believe that this approach underestimates the number of initial breakdown seeds. For a large number of breakdown counts, sites may be overlapped in camera images, particularly since each pixel resolves ~50 μm. Propagation effects may also suppress the number of counts

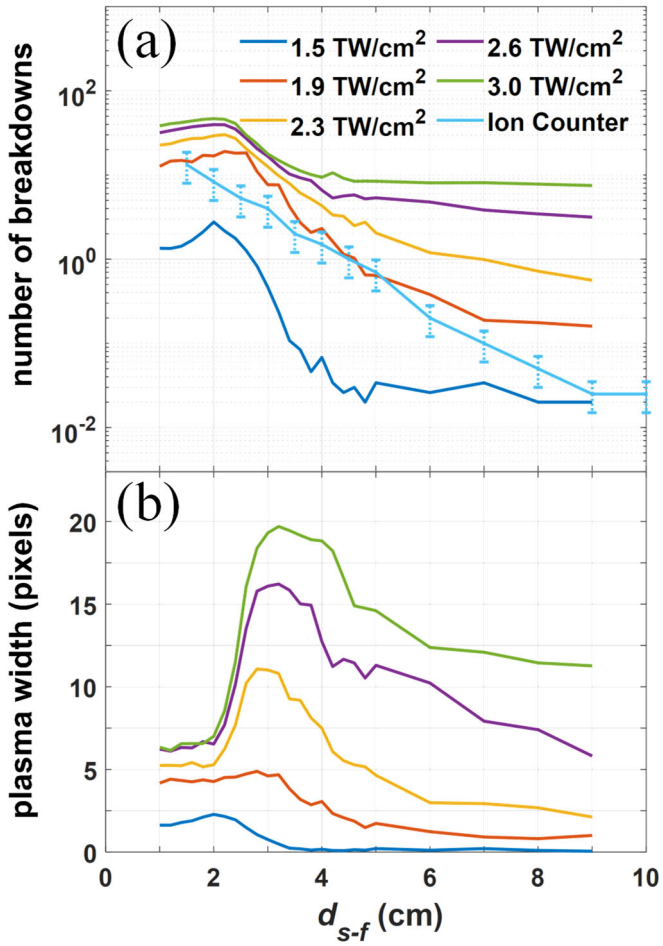

Figure 4.4. Summary of data from CMOS camera images. (a) Mean number of individual breakdowns observed for a range of intensities as function of source distance, with 500 shots at each position. Fig. 4.1(d) shows a typical image from which breakdowns were counted. The ion density measured with the Gerdien ion counter is overlaid with arbitrary scaling for comparison. (b) Mean value of the widest peak extracted from each shot (over 500 shots) for the same scan of intensity and source distance. Each camera pixel corresponds to ~50 microns, such that many smaller breakdowns lead to detection on a single pixel.

downstream of the laser focus, as discussed below. Both of these effects would result in a lower fitted value of I_{th}, and thus an overestimate of the breakdown volume. Using a subsequent experimental setup [39] which directly measured the λ=3.9μm, 50ps laser breakdown threshold using seed electrons released in the center of its focal volume by a secondary laser, we measured radiation seed densities ~5×10^6 cm^{-3}, a factor of ~20× higher than inferred from the Fig. 4.4, and closer to the total number density of negative

ions measured with the Gerdien condenser meter. Below, we will discuss two more measurements suggesting that a significant fraction of all negative ions contribute to avalanches.

The plots of breakdown site counts vs. d_{s-f} in Fig. 4.4(a) show a peak seed ion density near ~ 2-2.2 cm. We identify this as the location of the Bragg peak for 5.3 MeV α-particles in air, which is consistent with CSDA calculations of their stopping distance (~3.5 cm) [201], but is lower due to energy lost as α-particles leave the source (Po-210 embedded in a metal foil), and their angular emission spread from the source foil. At the Bragg peak, α-particle energy deposition in air increases as particles near the end of their range. This results in a peak in ion density near d_{s-f} ~2-2.2cm followed by a rapid drop at longer distances, which is borne out in all curves of Fig. 4.4(a). This feature also agrees with the decrease in observed breakdown time advance seen beyond 2.5 cm in Fig. 4.3(d). The absence, in the overlaid Gerdien ion counter curve in Fig. 4.4(a), of a peak ion density near 2 cm suggests that the ion counter measurements were smeared out by air flow and the size of the intake port.

Farther from the source (d_{s-f} >5 cm), the number of breakdown sites in the focal volume plateaus, and problematically, the seed ion densities calculated using V_{th} are strongly intensity-dependent. There are several factors contributing to this effect. First, 2-3% of all shots show early breakdowns, likely seeded by dust, which introduces a baseline average of ~0.02 breakdown sites per shot, as seen in the curve at 1.5 TW/cm^2. Dividing the remaining four curves by the breakdown volume $V_{th}(\hat{I})$ shows

an increase in the seed ion density as $N_i \propto I^{4-5}$. If the threshold intensity (and thus V_{th}) is actually smaller as discussed above, this scaling would have a larger exponent. We show in Chapter 5 that this increase in the number of counts likely stems from a ubiquitous contaminant with an ionization potential of $\chi_p \sim 6$ eV and a relative concentration of ~10^{-9} -10^{-11} [39].

To assess the importance of propagation effects on our 3 detection channels, we examined the laser energy absorbed at local breakdown sites. We recorded the FWHM width of the brightest breakdown site in each image, which, assuming saturation of the local breakdown plasma density, correlates with the laser energy absorbed by that plasma and its backscatter over the pulse. This metric, averaged over 500 shots at each position, is shown in Fig. 4.4(b), with each pixel value corresponding to ~50 microns. It is seen that for I > 1.9 TW/cm^2, the breakdown sites with greatest heating are located near d_{s-f} ~3 cm. However, for $d_{s-f} < 3$ cm, the maximum plasma size (and heating) drops abruptly and clamps at ~5 pixels (250 microns), irrespective of intensity. This behavior is not due to the reduced ion density before the Bragg peak, since Fig. 4.4(a) shows that the ion density close to the source (<2 cm) is still higher than beyond 3 cm, yet breakdown sites for $d_{s-f} > 3$ cm are more strongly heated. The decrease in plasma size is less pronounced for the runs at 1.9 TW/cm^2, where the breakdown count in the focal volume is ~10, compared to 20-50 breakdowns at higher intensities. For I = 1.5 TW/cm^2 on the other hand (breakdown count ~1-2), the peak heating occurs at the same position as the Bragg peak (~2 cm), consistent with the highest seed ion density giving the highest probability of seed locations close to peak laser intensity.

We infer from these results that scattering and refraction from multiple plasma sites dominate our laser-driven avalanches at high laser intensity and seed ion density. As the number of breakdown sites increases, Mie scattering from plasmas upstream of the focused beam waist can reduce the intensity of the laser pulse, limiting late time heating and growth of downstream breakdowns. A simplistic model that overestimates this effect takes each avalanche site as a plasma sphere of diameter 250 μm (based on the clamped plasma size in Fig. 4.4(b)) which casts a shadow over half the longitudinal extent of the breakdown volume (~3 mm). This predicts an occluded volume (shadow) per seed ion of $\sim 10^{-4}$ cm^3. Hence, for seed ion densities $>\sim 10^4$ cm^{-3}, the heated and expanding breakdown sites scatter the pump laser enough to mutually limit their heating—hence the effective clamping in plasma heating and growth observed at short distances in Fig. 4.3(b). Despite the simplicity of this model, this estimate is within an order of magnitude of the measured seed ion concentration of $\sim 10^5$ cm^{-3} at 3 cm, where these effects are important. Since the plasma breakdown sites affect pump propagation only toward the end of the plasma evolution when their density and size are high enough to induce significant scattering and refraction, this effect should not affect the breakdown time determined by the seeds located at the highest intensity. It will, however, limit the late time heating, plasma size, and subsequent laser backscatter and plasma emission. This, then, explains the divergence in backscatter and plasma emission signals vs. the time advance signal in Fig. 4.3: Time advance is determined by breakdowns occurring sufficiently early that propagation effects have not yet affected the signal, while integrated backscatter and plasma emission sample the

breakdowns through the full pulse, and so both are strongly affected by propagation effects.

While a complete treatment of 3D optical propagation through a time-dependent distribution of high density plasma scattering centers is beyond the scope of this work, we note that prior work has often observed that scattering from laser-produced plasma limits plasma heating and growth further downstream [207,208]. In addition, carbon black suspensions which seeded localized electron avalanche were observed to limit the laser intensity through Mie scattering [209], consistent with our observation of the clamping of plasma heating and growth near the α-source, as plotted in Fig. 4.4 (b).

4.6.4 Comparisons with breakdowns in N_2 and a corona discharge

We now consider a series of measurements, taken during the first experiment [37], which shed some light on the question of which ions contribute to laser-driven breakdowns. In the first measurement, we compared the breakdowns seeded by the α-source to those seeded by a corona discharge ion generator. Our results, in Fig. 4.5, show comparable results, as measured by breakdown time advance and backscattering, between the two sources when the total negative ion density from the generator, again measured with the Gerdien ion condenser meter, is 10^6-10^7 cm^{-3}. Even though some past work suggests that electric discharges and radioactive sources can generate different distributions of ion species [199], the maximum timing shift in each case was similar. This suggests that for similar charge density, laser-driven air breakdown is insensitive to the details of the particular ion distribution.

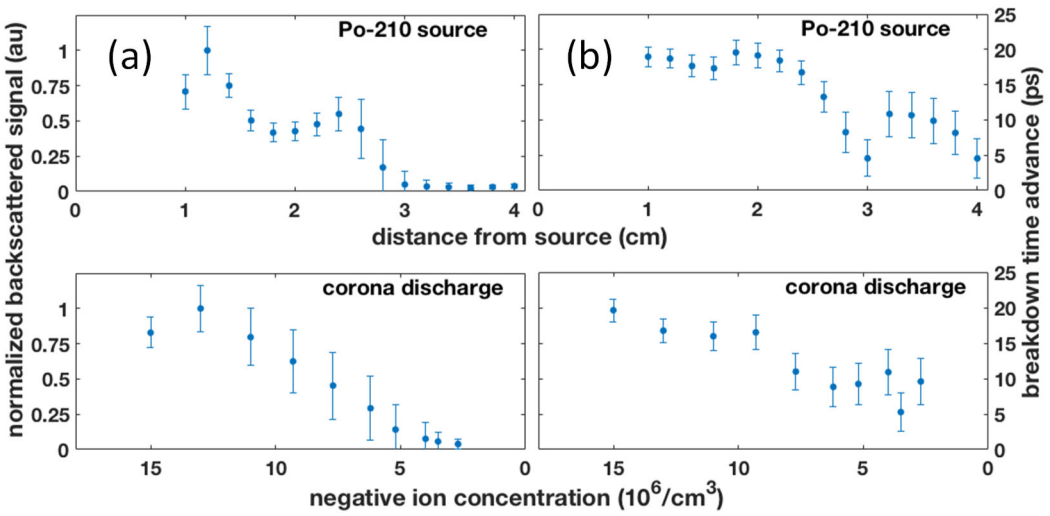

Figure 4.5. Comparison of avalanche breakdowns seeded by Po-210 source and corona discharge ion generator. (a) Normalized backscatter signal vs. source distance from breakdown seeded by Po-210 source (top) and vs. negative ion concentration from ion generator (bottom). All shots are for an intensity of ~4×10^{12} W/cm^2 [uncertain due to measurement nonlinearity], which was high enough to ensure breakdowns at every position/ion concentration. **(b)** Breakdown time advance vs. distance from breakdown seeded by Po-210 source (top) and vs. negative ion concentration from ion generator (bottom). Error bars show the standard deviation over 2500 laser shots..

In the second measurement, we observed breakdowns for α–radiation of a flow of pure N_2. In a pure N_2 environment, free electrons produced by ionizing radiation and knock-off electrons do not form negative ions, since N_2^- is an unbound state [204]. Thus, avalanche breakdown in irradiated N_2 is seeded by free electrons. The total number of negative charges should be similar to that of air, since its "W-value" is ~36 eV [210], as compared to 35 eV for air. Likewise, the breakdown evolution should be similar, since in a follow-up experiment [39], we measured comparable intensity thresholds for N_2 and air. When comparing the Po 210-irradiated N_2 breakdown to one in air (both located 1 cm from the source), there was no detectable shift (>2.5 ps) in the breakdown time advance, from which we infer that the local free electron density in the irradiated N_2 sample is roughly comparable to the negative ion density in the air. This

then strongly suggests that the seed density level was the same between N_2 and air, and thus that all negative ion species contribute to our time advance measurement.

4.7 Simulations

4.7.1 Discrete breakdown simulations

In the present experiment using 50 ps laser pulses, avalanche breakdown sites seeded by individual ions are nearly stationary and evolve entirely according to the local laser intensity. As discussed in Sec. 1.4.4, for a time t, electrons in the tenuous breakdown plasma diffuse over a length scale $r_d = \sqrt{2D_e t}$ for an electron diffusion coefficient $D_e = k_B T_e / m\nu_{en}$, where ν_{en} is the electron-neutral collision rate, m is the electron mass, k_B is Boltzmann's constant, and T_e is the electron temperature. Using typical values from our breakdown simulations (below) of $k_B T_e$ ~10 eV and ν_{en}~ 2-4 ps^{-1} [112,113] gives r_d ~ 3-8 μm for time delays t ~10–70 ps during the heating pulse envelope. This length is an overestimate that applies to electrons very early in the breakdown before they are restrained by local plasma electrostatic forces. The small value of r_d guarantees that individual breakdown sites remain localized and stationary relative to the scale of the laser focus, where the spot diameter and confocal parameter are $2w_0$=240 μm and $2z_0$ =10 mm.

The above considerations restrict the type of ionization model appropriate for our conditions. "Zero-dimensional" or "0D" models—ionization rate equations with no spatial dependence of ion or electron densities—implicitly assume that these densities are uniform or smoothly varying [128,193]. Such an approach is not appropriate for a

very low density ($< r_d^{-3}$) of seed electrons, nor for the locally high plasma density in the vicinity of an avalanche site, which is surrounded by neutral air.

We can, however, use a 0D model to provide the local electron density growth rate and electron temperature and apply it to the breakdown proceeding from a single seed electron, since for breakdowns which have not achieved saturation, electron velocity distributions are largely determined by laser-driven heating via electron-neutral collisions [40]. To proceed, we used coupled rate equations for electrons, neutrals, positive ions, and negative ions as detailed in [128] and added loss terms important for high temperature picosecond breakdowns [129,211]. The model is discussed in greater detail in Chapter 6. Here, the pulse is much longer than typical heating times $\tau_h \sim T_e/2U_p\nu_{en} \sim 1$ ps at our conditions [40,130], so avalanche growth adiabatically follows the intensity. Using growth rates extracted as a function of intensity from the 0D model, we then track the local density used in a simulation of a single electron seed by dividing the number of electrons by an effective volume $4\pi {r_d}^3/3$, where r_d transitions to an ambipolar diffusion scale length once the plasma Debye length $\lambda_D = (k_B T/4\pi n_e e^2)^{1/2}$ is equal to the electron diffusion length [132,212].

The breakdown onset time for a seed electron exposed to a given peak intensity is taken to be the time when the electron density reaches ~10^{18} cm^{-3}, which corresponds to the experimental breakdown detection threshold. The resulting time advance Δt_{adv} (the difference between the breakdown time and the end of the pulse) for a range of local peak intensities is shown in Fig. 4.6 (a) for a third-order super-Gaussian pulse

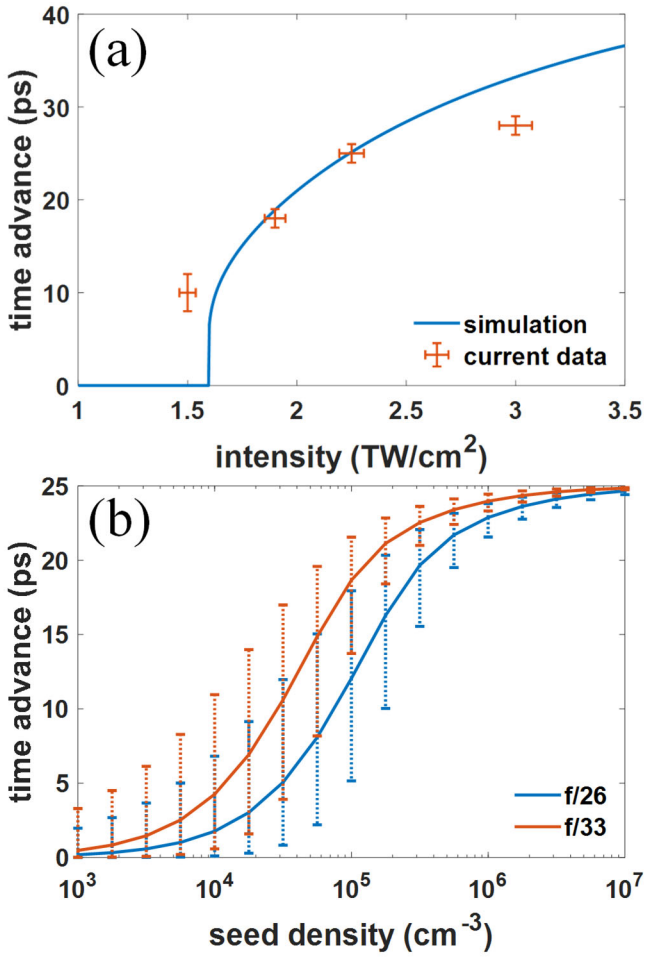

Figure 4.6. Results from numerical simulations. (a) Simulated breakdown time advance (as determined by reaching a threshold electron density of 10^{18} cm^{-3}) for single electrons exposed to a super-Gaussian temporal pulse for a given local peak intensity. Below the threshold of ~1.6 TW/cm^2, the model predicts no detectable breakdown. Maximum time advance vs. intensity is also plotted for current experimental data. (b) Statistical breakdown time advance modeled for two focal volumes for peak intensity 2.25 TW/cm^2 as a function of seed density. Each point shows the mean expected breakdown time and spread, calculated (separately) as the standard deviation for values above and below the mean. For the larger focal spot (*f*/33), the volume above the breakdown threshold (Eq. 4.1) becomes larger, providing sensitivity to a lower seed density.

with FWHM duration of 50 ps. The simulation curve in Fig. 4.6 (a) predicts a breakdown onset intensity threshold ~1.6 TW/cm^2, which agrees well with the experimentally threshold of ~1.5 TW/cm^2 for observing backscatter. Maximum time advances observed as a function of intensity in the current experiment are also plotted, and show reasonable agreement with simulations.

4.6.2 Simulating statistical breakdown time advance

While our adapted 0D model predicts the breakdown time advance initiated by a seed electron exposed to a given laser intensity, the distribution of seed electrons in a region of spatially varying intensity introduces a statistical spread in the onsets of local breakdowns, as discussed above in Sec. 4.5. The Poisson probability that a given intensity I will determine the time advance is $P(I) = e^{-n'}(1 - e^{-\delta n})$, where $\delta n = N_i \delta V$ is the average number of seed electrons in a volume element δV corresponding to intensity I, and $n' = N_i V'$, where V' is the volume corresponding to higher intensity $I' > I$. A calculation incorporating these probabilities is presented in Fig. 4.6 (b), which tracks the mean value of breakdown time advance for different focal volumes as seed density is increased (at constant peak intensity of 2.25 TW/cm^2). Error bars are given by the standard deviation above and below the mean. It is seen that decreasing the *f*/number (and focal volume) shifts the sensitivity to lower seed densities, and that at high seed densities, the time advance saturates to the values predicted in Fig. 4.6 (a). The simulation results are in good quantitative agreement with our present experiment (*f*/33 focusing, or a 3 cm beam focused at 1 meter): at 2.5 cm from the source where we measured a seed density $2(^{+2}_{-1})\times10^5$ cm^{-3} through imaging, we measured a time advance (for 2.25 TW/cm^2) ranging from 19-22 ps (range of standard deviation error bars in Fig 4.3 (d)), matching the range generated through simulations (18-23 ps at a seed density of 1.7×10^5 cm^{-3}). At $d_{s-f} = 4$ cm (seed density ~10^4 cm^{-3}), we measured a time advance of 6-15 ps, compared with a simulated time advance of 0.5-10 ps. If the

density estimates were revised upward by a factor of ~10× as discussed above in Sec. 4.6.3, the agreement is similar on the high end, but slightly worse on the low end. However, given approximations made in the simulations discussed in Chapter 6, such agreement within an order of magnitude is reasonable.

4.8 Application to remote detection at large standoff distances

Based on the results of the present experiment, any laser focal geometry with the same pulse width used for remote detection at range will require peak intensities above the threshold of 1.5 TW/cm^2. In Sec. 1.4.2, we found breakdown thresholds scale as λ^{-2}, but the increase in focused spot size as λ for fixed $f/$number implies varying wavelength will not change the total power/energy required. Breakdowns leading to a backscatter signal with SNR >10 require higher intensities ~1.6-1.8 TW/cm^2. For example, detection at a range of 100m using a λ=3.9μm, 50 ps pulse would require focusing of ~75 mJ at *f*/100 by a 1 meter diameter optic. This would probe a focal volume ~10^{-3} cm^3, providing sensitivity to seed ion densities ~10^3-10^4 cm^{-3} (with statistical variations in time advance below 10^4 cm^{-3} and saturation above it).

While the scaling presented above is, in principle, straightforward, propagation and focusing over tens of meters is complicated by turbulence and nonlinear propagation. We note that delivering intense pulses at range through realistic atmospheric conditions is an active area of theoretical research [213], and that a recent experiment has demonstrated long range propagation by self-channeling through turbulence and linear compensation of initial pulse chirp [214,215].

As noted in Sec. 4.6.1, 2-3% of all shots exhibited very bright, early breakdowns with large values of time advance, uncorrelated with the radioactive source or the driving intensity. This behavior is consistent with dust-initiated avalanches, which have a reduced breakdown threshold and start at high local density. While these dust-initiated breakdowns would be an important consideration under field conditions, it is easy to sort them from the data owing to their large time advance (30-40 ps) and high relative backscatter energy compared to negative ion-seeded breakdowns (10-20 ps time advance). However, in a detection environment that includes enough dust and aerosols to seed such early breakdowns on every shot, additional sorting of the data would be required. One possibility would be to combine information from multiple detection channels (avalanche time advance, total backscatter energy, and plasma emission) to further constrain data processing and analysis.

While increasing the focal volume at a fixed seed density increases the number of breakdown sites, the laser pulse repetition rate can be severely limited by the much longer diffusion time of long-lived breakdown products out of larger focal volumes, lengthening the time required for the air to return to equilibrium conditions. This issue will become more pronounced at standoff distances where focal volumes might increase by a few orders of magnitude. However, under field conditions, this self-seeding effect might be avoided by dynamically sweeping the focal position.

For increased $f/$number (ratio of standoff distance R to focusing optic diameter D) at larger standoffs, the focal spot, and hence energy $\mathcal{E}$ required, increase as $w_0 \propto (R/D)$, $\mathcal{E} \propto (R/D)^2$. This indicates ~750 mJ for focusing our pulse length at $f/300$.

However, increasing the $f/$number quickly leads to a very large V_{th} due to its characteristic $V_{th} \propto {w_0}^4 \propto (R/D)^4$ scaling in Eq. (4.1). Correspondingly, sensitivity is degraded as the focal volume will always contain many seed ions even at background conditions discussed in Sec. 4.3 (N_i ~10^2-10^3 cm^{-3}). Likewise, moving to longer wavelengths, such as the 95 GHz source used in [134], increases the V_{th} for fixed $f/$number as λ^3. Providing the seed ion density exceeds background levels, maintaining sensitivity requires decreasing the number of ions from which seed electrons are liberated. This can be achieved for long wavelength lasers, since ion detachment will decrease as both the required intensity $I_{th} \propto \lambda^{-2}$ and photon energy $\hbar\omega$ decrease.

A hard limit on V_{th} is set by the background density of free electrons (~10^{-2} cm^{-3}) as set by cosmic rays and sources such as radon, since even longer wavelength lasers will always initiate avalanche from these existing free electrons. While operating arbitrarily close to the threshold intensity ($\hat{I} = I/I_{th}$~1), this degrades SNR. We note in particular that this limits would strongly discourage the use of microwave sources as considered in [134].

4.9 Summary and conclusion

We have demonstrated laser induced avalanche detection of a radioactive source in a true standoff geometry, where the three remote detection channels rely only on backscattering or plasma emission. Of the three demonstrated detection channels, we found that the breakdown time advance diagnostic—which depends on single shot spectrally-resolved measurements of chirped pulse backscatter— gave the most precise

measure of the radiation environment, and was also immune from pump laser scattering by multiple breakdown plasma sites. We discussed extending these diagnostics to greater (>10 m) standoff distances.

We have also demonstrated that direct imaging of the laser breakdown volume, which enables counting of the individual breakdown plasma sites and measuring their sizes, is a very powerful benchmark for assessing the fidelity of the three remote detection channels. The direct imaging measurement also makes possible the absolute determination of ultralow charge densities, with direct measurement of an extremely low densities (10^5 cm^{-3} and below) of O_2^- and other ions produced through subsequent air chemistry. As there is still some question as to which ion species we detect, our avalanche method could be further improved using auxiliary pulses tuned to detach ions with more specificity, coupled with longer wavelength, lower intensity avalanche driver pulses.

Chapter 5: Absolute measurement of laser ionization yield in atmospheric pressure range gases over 14 decades

5.1 Multiphoton and tunneling ionization yield measurements

The unification of tunneling ionization and multiphoton ionization (MPI) of atoms in intense laser fields by Keldysh in 1965 [49] provided an analytic foundation for strong field laser physics [50,102,216-218], but measurements of the transition from MPI to tunneling had to await later advances in short pulse lasers [135,219-221]. This transition is characterized in atomic units by the dimensionless Keldysh parameter $\gamma = \left(2\chi_p\right)^{1/2}\omega/E_0$, where χ_p is the atom's ionization potential, E_0 is the peak laser field, and ω is the laser frequency. At moderate intensity I ($\gamma \gg 1$, MPI regime), the yield Y, or ionization probability, is proportional to E_0^{2n} ($\propto I^n$), while at higher intensities or longer wavelengths ($\gamma < 1$), the transition to tunneling and barrier suppression ionization [219,220] is characterized by $Y \propto I^{p<n}$, where n is the integer number of photons needed to exceed χ_p. Early yield measurements were conducted in extremely low density gases (typically ~10^8 –10^{12} cm^{-3}) in order to prevent ionization products interacting with background gas or experiencing space charge effects in transit to high voltage detectors [103,219,220]. However, many applications of strong-field ionization, such as high harmonic generation [8] or high intensity pulse propagation [2,3], occur at atomic densities many orders of magnitude higher where density-dependent ionization may be important.

Recent theoretical work, for example, suggests many-body effects in high density gases leads to an additional ionization channel which is important at lower laser intensities: excitation-induced dephasing (EID) [51-54]. If "standard" isolated atom multiphoton/tunneling ionization is viewed as the result of optical-field induced dephasing of bound state-continuum coherence, which spoils the adiabatic following of the electron population in the strong, highly detuned optical field, then at elevated densities it was proposed that additional dephasing from Coulomb interaction with electrons in nearby atoms enhances ionization beyond the isolated atom process. EID calculations [51] predict that the additional yield scales nearly linearly with density and is proportional to I^2 (in strong contrast with I^n scaling for MPI), and is nearly independent of target species and laser wavelength, as shown in Fig. 5.1. Of particular interest to our experiments, EID predicts yields Y in the range 10^{-9}-10^{-7} for 1 TW/cm^2, λ=1-10 μm, 100 fs pulses in a variety of atmospheric pressure range gases [51-54], with $Y \propto I^2$ up to a transition to the isolated atom rate at higher intensities. For example, for a λ=1 μm, 100 fs pulse in hydrogen, Ref. [53] showed $Y \propto I^2$ up to $Y \sim 10^{-6}$ at $I \sim 20$ TW/cm^2, transitioning to MPI yields ($\propto I^{10}$) of $\sim 10^{-5}$ at $I \sim 40$ TW/cm^2. While prior ionization yield measurements at atmospheric pressure [222,223] have shown reasonable agreement with isolated atom rates, they were limited to $Y > \sim 10^{-5}$ for a λ=800 nm driver, precluding investigation of EID ionization.

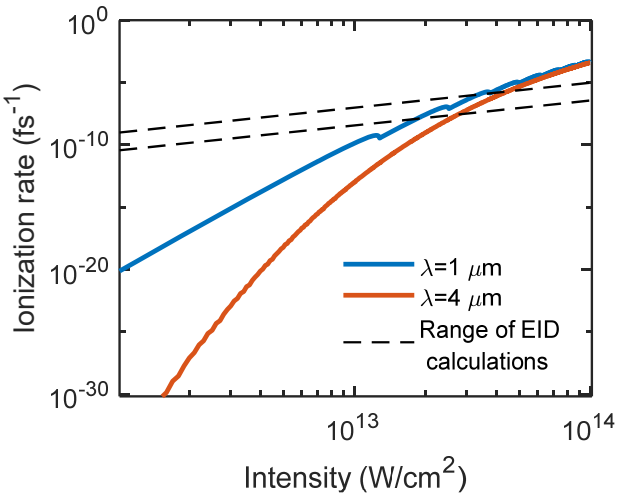

Figure 5.1. Comparison of standard ionization theory with EID many-body ionization. Calculated standard ionization rate [50] of O_2, the most readily ionizable air constituent, for $\lambda = 1\ \mu$m (blue) and $\lambda = 4\ \mu$m (red), as in Sec. 1.2.4. Calculations of EID ionization have only been performed for atomic hydrogen and argon [51-54], with an approximate range of effective rates for $\lambda = 1 - 10\ \mu$m pulses shown by the dotted lines. Despite very different ionization potentials and photon energies, predicted rates fall in a narrow range.

The potential effect of EID ionization is significant, especially when its boost to plasma density would have a commensurately larger effect on the refractive index experienced by longer wavelength lasers. For example, under conditions where standard ionization is negligible, EID was invoked to explain a recent experiment observing self-channeling of a λ=10.2 μm, ~1 TW/cm^2 peak intensity CO_2 laser pulse over 20 Rayleigh ranges in air [21], a process requiring plasma generation to offset Kerr self-focusing.

Here, we use avalanche ionization driven by a picosecond, mid-IR *probe* laser pulse to measure absolute ionization yields over 14 decades (10^{-16} to 10^{-2}) from femtosecond near-IR and mid-IR *pump* pulse irradiation of atmospheric pressure range

air, nitrogen and argon (0.5-3 bar) [39]. This represents an unprecedented dynamic range with a single setup, with sensitivity exceeding all other methods we are aware of.

5.2 Experimental setup and methods

As discussed in Chapters 1 and 4, during avalanche ionization free electrons (here initially generated by femtosecond pump pulses) gain sufficient energy through probe-driven collisions until they ionize neutral atoms/molecules, leading to an exponential growth factor $e^{\nu_i t}$ in the local number of electrons, where ν_i is the effective collisional ionization rate, enabling single electron sensitivity. Avalanche ionization was driven by a positively chirped ~10 mJ, 50 ps λ=3.9 μm probe pulse focused to intensities ~1–1.5 TW/cm^2 at a $1/e^2$ intensity radius (waist) of $w_0 = 70\mu$m. As discussed in Chapter 4 (Sec. 4.5), the probe pulse length and peak intensity define a breakdown threshold and volume inside which breakdowns from individual seeds will be detectable, although in this experiment, breakdown locations are further constrained by the overlap of this volume with the focused femtosecond pump pulse. Crucially, the mid-IR avalanche driver eliminates driver-supplied MPI electrons from the seed population [37,38], such that only pump-induced ionization produces in probe-driven breakdown sites.

Figure 5.2 shows the experimental setup. The femtosecond pump pulse, synchronized to the avalanche-driving probe, was either in the near-IR (λ=1024 nm, 274±10 fs) or in the mid-IR (λ=3.9 μm, 85±5 fs) and focused to peak intensities of 1–100 TW/cm^2, with intensity control provided by a waveplate and polarizer. All three pulses were derived from a 20 Hz chirped pulse amplification (OPCPA) system [149].

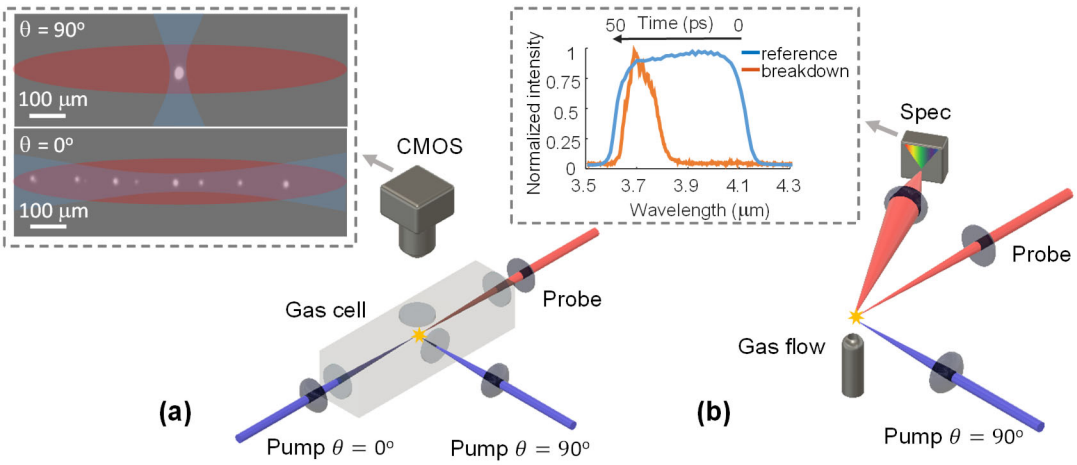

Figure 5.2. Experimental setup. (a) *Breakdown counting* (I <10 TW/cm^2): A positively chirped, λ=3.9–4.2 μm, 50 ps mid-IR laser probe pulse was focused into a gas cell to drive avalanche breakdowns seeded by electrons liberated by either a counter-propagating ($\theta = 0°$) or a perpendicularly-directed ($\theta = 90°$) pump pulse (274 fs, $\lambda = 1024$ nm or 85 fs, $\lambda = 3.9$ μm). The inset shows, for each geometry, sample images of individually seeded breakdowns, collected by camera CMOS, and overlaid with pump pulse focal volume (blue) and the probe pulse breakdown threshold volume (red). **(b)** *Breakdown time advance* (I >10 TW/cm^2): pump-induced initial plasma density and corresponding yield are determined from breakdown timing encoded in the backscatter spectrum of the chirped mid-IR probe pulse. Backscatter is collected by spectrometer Spec, with example incident and backscattered spectra and corresponding timing shown. Here, breakdowns are observed directly above a ~5 mm gas flow orifice

The λ=1024 nm pump pulses were focused to Gaussian waists ($1/e^2$ intensity radius) of w_0=8 μm (I < 100 TW/cm^2, Rayleigh range z_0~0.2 mm) or w_0= 26 μm (I < 10 TW/cm^2, z_0~2 mm) for transverse overlap of pump-probe beams ($\theta = 90°$, see below), while for counter-propagating beams ($\theta = 0°$), they were focused to w_0= 30 μm. The λ=3.9 μm pump pulses were focused to w_0=39 μm (z_0~1.2 mm, up to 10 TW/cm^2) for $\theta = 90°$. Near-IR and mid-IR peak pump intensities were determined by measuring focal spots directly on a CCD camera or an InSb array, respectively. Pulse duration measurements made using an autocorrelator (for λ=1024 nm) or with scanning second-harmonic generation frequency resolved optical gating (SHG-FROG, for λ=3.9

μm). Uncertainty in pulse duration ($\pm\sim 5$ %) and focused beam spot size ($\pm\sim 4\%$ due to finite pixel size) gave absolute uncertainty of $\sim \pm 10\%$ in measured intensity values.

For low yields up to $\sim 10^{-11}$, visible avalanche breakdowns are local to individual seed electrons, with radial migration of avalanche-liberated electrons limited to $< \sim 10\ \mu m$ by electron and ambipolar diffusion during the 50 ps probe pulse [38,132]. Thus breakdowns are isolated and were counted by imaging, with a 16-bit low-noise CMOS camera, the overlap of the pump pulse and probe breakdown volume (Fig 5.2 (a)) inside a sealed gas cell filled with air, nitrogen, or argon passed through a 0.01 micron rating particulate filter. In this regime, the occurrence of breakdowns is statistical, requiring multi-shot averaging. Images were collected at 2× magnification on the CMOS camera, and the number of breakdowns was determined by counting the number of sites with peak signals above 20 pixel counts after median filtering.

In order to determine the breakdown threshold for different gases and pressures, probe pulse peak power was reduced until the pump-seeded breakdowns at the center of the probe volume (peak probe intensity) were barely visible (~20 pixel counts). This gave a breakdown threshold $I_{th}\sim 1$ TW/cm^2 in nitrogen and air, and 0.6 TW/cm^2 in argon, with a $1/p$ pressure dependence for all gases studied, in line with scalings presented in Sec. 1.4.2. We note that due to the high level of control of location and number of seed electrons using the pump pulse, this measurement is far more precise than those based on count ratios presented in Chapter 4 [38]. In order to determine peak yield Y_0 corresponding to the peak intensity I_0, we use $N = \int_V Y_0 \cdot (I(r,z)/I_0)^m\, dV$,

where N is the average number of counts measured, $I(r,z)$ is the spatially varying pump intensity with peak value I_0 over the probe breakdown volume V , and the yield is observed to scale as I^m. A counter-propagating ($\theta = 0°$) pump-probe geometry maximized the overlap volume and hence sensitivity. As higher pump intensity increased the number of seed electrons beyond ~10, individual breakdowns upstream interfered with probe driving of downstream avalanches [38]. Switching to a perpendicular geometry ($\theta = 90°$) reduced the overlap volume $\sim 100\times$, eliminating this propagation effect at higher yield. While the small volume for $\theta = 90°$ prevents reliably imaging more than 1 breakdown per shot, counting the incidence of no breakdowns allowed us to infer the Poisson mean up to ~4 breakdowns/shot, since a Poisson distribution with mean value μ has a probability $P(0) = 1 - e^{-\mu}$ of observing no counts. With the pump blocked, breakdowns occurred in ~1 out of 100-1000 shots due to probe-induced MPI of a contaminant (see below).

As the yield (and seed electron density) increases even further, $Y \lesssim 10^{-10}$ to 10^{-2}, adjacent incipient avalanche sites become closer than the electron diffusion length and it is no longer possible to resolve and count breakdowns. However, the avalanche is now seeded by a well-defined local electron density such that one can measure a deterministic avalanche time, $\tau = \ln(N_{ef}/N_{e0})/\nu_i$, where N_{e0} is the seed electron density, ν_i is the electron density collisional growth rate, and N_{ef} is a final (detectable) electron density [128]. By employing the chirped probe-backscatter breakdown timing method discussed in Sec. 4.2 [38], we measure the breakdown time advance $\Delta t_{adv} =$

$\tau_{driver} - \tau$, where $\tau_{driver} = 50ps$ is the avalanche driver duration, and Δt_{adv} corresponds to the reddest (earliest) wavelength of the chirped probe pulse detectable in the backscattered spectrum at a detection threshold $N_{ef} \sim 10^{18}$ cm^{-3} (see Appendix A.1). The spectrum is collected by a single shot mid-IR spectrometer (Sec. 2.6, [38]), with setup and example spectra shown in Fig. 5.2 (b). Wavelength-to-time correspondence of the chirped driver was established using a cross correlation with the λ=1024 nm beam.

5.3 Results and Discussion

Figures 5.3–5.5 together show femtosecond pulse ionization yields Y spanning 14 orders of magnitude. For lower peak intensities of $0.6 - 10$ TW/cm^2, where yields are determined from counting individual breakdowns, Fig. 5.3 plots Y_{1024nm} for air (a), a comparison of Y_{1024nm} for air, N_2, and Ar (b), and $Y_{3.9\mu m}$ for air (c), all at atmospheric pressure. Here, $\gamma_{1024nm} > 3$ and $\gamma_{3.9\mu m} < 0.9$, in the MPI and tunneling regime, respectively. The corresponding average breakdown counts/shot are shown on separate scales. In Fig. 5.3 (a), the curves for $\theta = 0°$ and $\theta = 90°$ are horizontally offset owing to peak intensity uncertainty of $\sim \pm 10\%$ (horizontal bars) in each geometry. Theoretical isolated molecule yields were calculated using a rate valid for arbitrary γ by properly treating the Coulomb correction in the multiphoton limit $\gamma \gg 1$ [49,50]. This "standard" yield for air (80/20 N_2/O_2) and N_2, using effective potentials for N_2 and O_2 [221], is plotted as the yellow curves in Fig. 5.3 (a, c), with the curve in Fig. 5.3(c) scaled up by $100\times$.

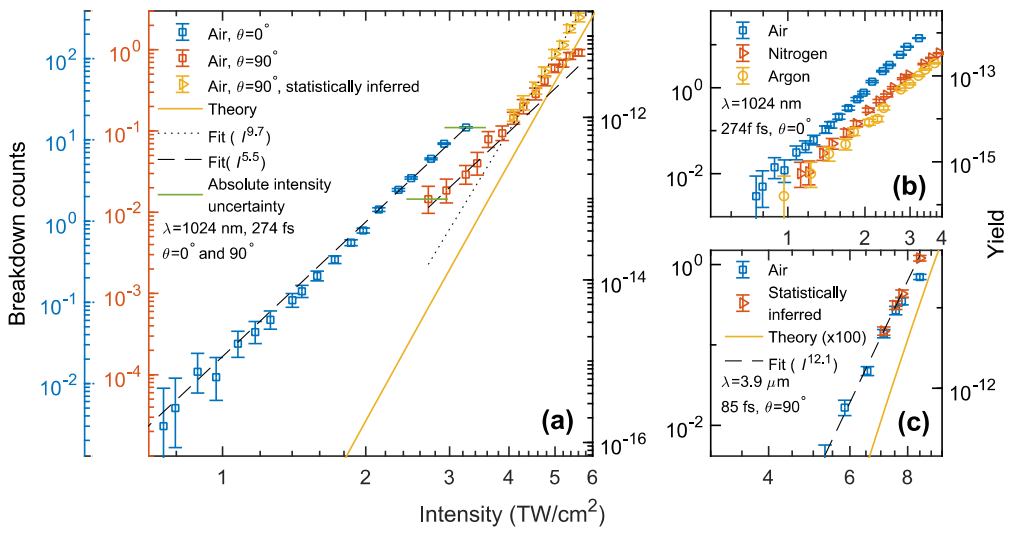

Figure 5.3. Ionization yield measured in breakdown counting regime (I <10 TW/cm^2). (a) Breakdown counts and corresponding yields Y_{1024nm} in $\theta = 0°$ and $\theta = 90°$ geometry. For $I > \sim 4$ TW/cm^2 , $Y_{1024nm} \propto I^{9.7}$, consistent with MPI of O_2 ($\chi_p \sim 12.1$ eV) and for $I < \sim 4$ TW/cm^2, $Y_{1024nm} \propto I^{5.5}$, consistent with MPI of a contaminant with $\chi_p \sim 6$ eV. Error bars correspond to a Poissonian 95% confidence interval [130]. Horizontal bars on the 0° and 90° plots reflect absolute intensity uncertainty from switching between geometries. The overlaid theory curve plots the yield based on standard N_2 and O_2 molecular ionization rates [50,221]. **(b)** Comparison of Y_{1024nm} for atmospheric pressure air, N_2 and Ar for $I < \sim 4$ TW/cm^2 ($\theta = 0°$), showing $Y_{1024nm} \propto I^{5.5}$ for all 3 gases. **(c)** $Y_{3.9\mu m}$ for atmospheric pressure air ($\theta = 90°$). The overlaid ionization theory curve for 80/20 N_2/O_2 is multiplied by 100. In (a) and (c), saturated counts were inferred statistically from the incidence of no breakdowns occurring, as described in the text.

Best fits to the data points for all 3 gases give $Y_{1024nm} \propto I^{5.5\pm0.3}$ (for $I < \sim 4$ TW/cm^2) and $Y_{3.9\mu m} \propto I^{12.1\pm0.8}$, with measured yields orders of magnitude greater than standard theory. For air at $I > \sim 4$ TW/cm^2, the yield dependence transitions to $Y_{1024nm} \propto I^{9.7\pm1.0}$, consistent with the expected MPI scaling of I^{10} for O_2, the most readily ionized air constituent ($\chi_p \sim 12.1$ eV). The $\sim 2\times$ offset between experiment and theory in this range is consistent with ~10% experimental uncertainty in absolute intensity and the lack of species-specific atomic structure in the theoretical rate [50]. The range of exponents is determined by the 95% confidence interval for linear fitting

to data on a log-log scale. We note that in this plot, the background level of counts from the mid-IR probe pulse alone is $\sim 10^{-3}$ for the low intensity pump points (for $\theta = 0°$) and $\sim 10^{-2}$ for $\theta = 90°$, as discussed more below.

These results strongly suggest that the ionization yield at lower intensity originates from a contaminant. As shown in Fig. 5.3 (b), these breakdowns were observed at a similar level in all gases, which included lab compressed air (filtered for oil/moisture and particulates) and high purity argon and nitrogen (Praxair, Ultrahigh Purity 5.0, <3 parts-per-million (ppm) water, <0.5 ppm total hydrocarbon content). When air passed through the particulate filter was replaced with bottled ultra-high purity air (Praxair, Ultra Zero, <2 ppm water, <0.1 ppm total hydrocarbon content) passed through an activated charcoal Supelcarb hydrocarbon filter (capable of filtering primary hydrocarbons to ~the part-per-billion level) for identical pump conditions ($\lambda = 3.9\ \mu m, \theta = 90°$), the number of breakdown counts decreased by ~4×, as shown in Fig. 5.4. The gas cell experiment was repeated for air pressures of 0.5 bar to 3 bar. At all pressures, the yield scaling at lower intensity followed $Y_{1024nm} \propto I^{5.5\pm0.3}$, consistent with the presence of the contaminant. At higher intensity, the yield dependence transitioned to the MPI scaling of O_2, as in Fig. 2 (a).

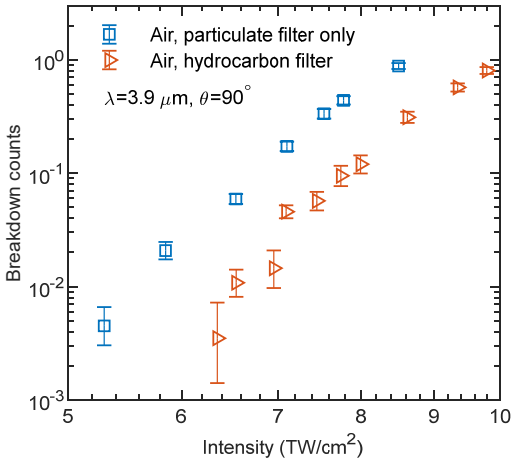

Figure 5.4. Effect of hydrocarbon filter on yield measurements in air. Breakdown counts observed with the λ=3.9 μm pump for two sources of air: (i) air passed through only the particulate filter or (ii) ultra-high purity compressed air from a bottle fitted with an additional part-per-billion hydrocarbon trap.

Since counts could not be observed below ~5 TW/cm^2 for $\lambda = 3.9\ \mu m, \theta = 90°$ and pumping in the $\theta = 0°$ geometry with the $\lambda = 3.9\ \mu m$ pump was experimentally difficult, low yield ionization for this wavelength was tested using breakdown counts initiated by "self-seeded" electrons, or seed electrons produced by the leading edge of the 50 ps, ~1.5 TW/cm^2 probe pulse which were subsequently amplified and detected as breakdown counts generated by the remainder of the pulse. Figure 5.5 shows both raw counts for 1.5–1.8 TW/cm^2, and corrections for the increase in size of the breakdown volume with increasing intensity and the increase in the time during which electrons can be liberated and amplified. Namely, if for a threshold of ~1 TW/cm^2 single electron-seeded breakdowns at a local intensity of 1.8 TW/cm^2 occur in ~50/1.8~27 ps while breakdowns at 1.5 TW/cm^2 occur in ~50/1.5~33 ps, the second pulse has 6 ps longer in which to ionize contaminants through MPI and still drive a detectable breakdown. (Here we roughly approximate $\nu_i \propto I$, as in Sec. 1.4.2). While

the correction is simplistic (applying changes in volume and timing as a constant multiplicative factor and ignoring spatial variations in yield and timing), it gives a rough estimate of the scaling in this regime. In particular, it shows that counts are still driven by MPI/tunneling, with a best fit of the corrected counts giving $Y_{3.9\mu m} \propto I^{19\pm8}$.

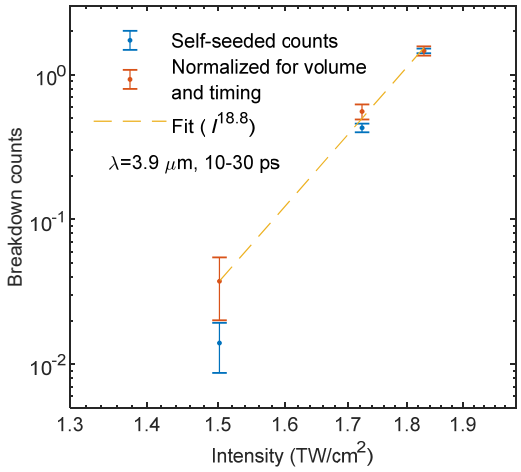

Figure 5.5. Scan of self-seeded counts. Number of breakdowns observed for varying probe (only) pulse intensities, with seed electrons liberated via MPI by the leading edge of the pulse. Also shown is a correction for changes in breakdown volume and effective seed timing as probe intensity is increased. A best fit of the points gives scaling $Y_{3.9\mu m} \propto I^{19\pm8}$, with the large uncertainty set by the limited range of results.

The strong intensity scaling of probe self-seeded breakdowns also explains the variation in background breakdown counts, since small changes in probe intensity (~10-15% uncertainty for different configurations, or intraday and day-to-day drifts) can lead to large changes in background rates. A slightly lower probe peak intensity for the $\theta = 0°$ experiment of Fig. 5.3 led to the ~10× reduction in probe self-seeded background counts compared to the $\theta = 90°$ geometry, despite the larger pump-probe overlap volume.

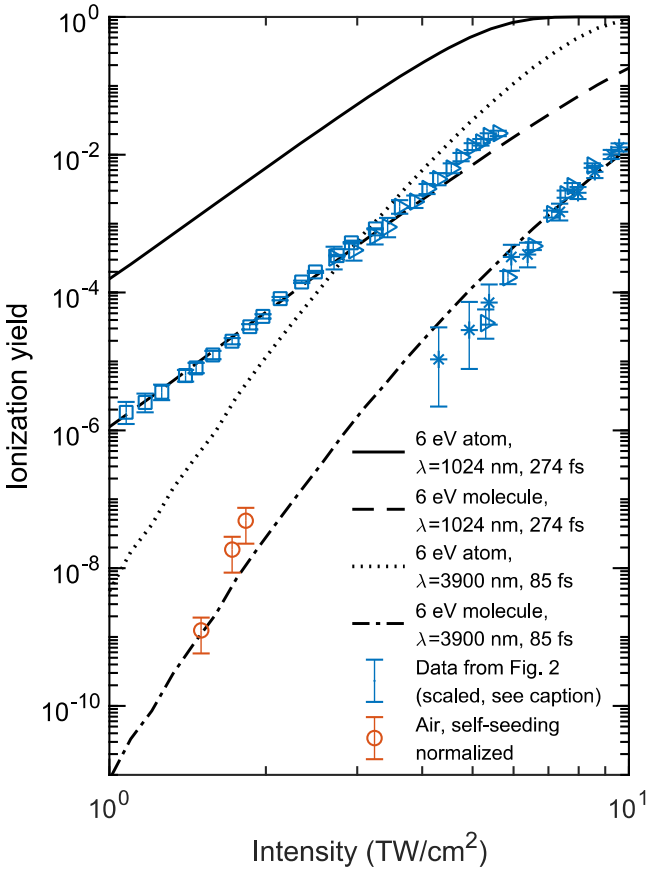

Figure 5.6. Comparison of contaminant yield with isolated atom/molecule theory. Counts in air ($\theta = 0°$, squares; $\theta = 90°$, triangles) and argon ($\theta = 90°$, stars) are shifted to overlap with theoretical curves for comparison. The red points (open circles) are from data in Fig. 4, normalized to the other λ=3.9 μm data on the plot. Two theory curves were generated for each wavelength: a 6 eV atom and a 6 eV molecule. The molecule calculation employs a shape factor (0.5) to account for changes to its tunneling potential [221]. The calculated contaminant yields, together with the absolute yields determined in Fig. 2, suggest a contaminant concentration in the range 10^{-11}–10^{-9}, assuming a shape factor bounded between 1 (atom) and 0.5 (typical molecule).

As shown in Fig. 5.6, fitting the yield scaling to the standard isolated atom/molecule ionization rate [50] suggests the contaminant species has an ionization potential χ_p~6 eV and an approximate concentration of ~10^{-11}–10^{-9}. The ≲2 TW/cm^2 (red) points with $Y_{3.9\mu m} \propto I^{19\pm8}$ inferred from Fig. 5.5 were normalized to the data taken with the 85 fs pump pulse by accounting for the ratio in volumes between the

self-seeding case and the $\theta = 90°$ geometry (~300) and the change in pulse length and temporal shape (~1000×). This normalization gives a yield in reasonable agreement with the theoretical curve, and is also consistent with a contaminant with ionization potential ~6 eV. We note that early MPI experiments indicated the presence of low ionization potential contaminants in all laboratory gases; these were considered to be the source for seed electrons in air avalanche breakdown experiments [103]. However, the concentration and yield of these seed sources could not be quantified as in the present work. We also note that experiments studying ionization of air with λ =248 nm laser pulses (5 eV photon energy) observed a $Y \propto I$ increase in yield for 10^6–10^9 W/cm^2 intensities, before transitioning to $Y \propto I^2$ yield dependence indicative of two-photon resonantly enhanced multi-photon ionization [127]. Based on plasma conductivity measurements, they inferred laser-induced electron densities of 10^9–10^{10} cm^{-3} and proposed that the results were consistent with ionization in aerosols, or an intermediate-state resonant excitation pathway in a contaminant.

Figures 5.7 and 5.8 cover the transition from MPI of air and N_2 to tunneling ionization, with $3 > \gamma_{1024nm} > 0.75$. In this regime, we used our breakdown time advance diagnostic described in Sec. 4.2. Conversion from Δt_{adv} to yield was calibrated by data from the direct imaging measurements at ~6 TW/cm^2 (Fig. 5.3 (a)) and previous absolute measurements of yield at ~100 TW/cm^2 [222], with direct interpolation between the points assuming a constant growth rate ν_i for a flat-top probe pulse intensity. Since this approach is novel, we take a detailed look at the calibration. For a single electron seed, the time required to reach a specific breakdown condition is

determined entirely by the local intensity. For the present experiment, the width of the breakdown volume (region above threshold) for driving avalanche and backscattering was ~40μm, while the diffusion-limited diameter of single-electron-seeded breakdown plasmas was ~10μm during their initial growth phase. Thus, even when a single breakdown occurs on every shot, timing measured by backscatter will be variable because a single pump-generated seed electron could find itself in a range of intensities above the breakdown threshold. This is seen in Figure 5.7, where the points at ~<6 TW/cm^2 show a timing variation even though Fig. 5.3 shows there is a ~1 breakdown/shot at that intensity. Once ~4-8 seed electrons are distributed in the breakdown region, there is a higher probability that one seed electron is located at the region of peak probe intensity, leading to more deterministic timing. Above ~8-10 seed electrons in the breakdown region, there is a high probability of 2 electrons being located at the region of peak intensity and within ~10μm of each other, such that number of generations (a doubling of electron number) needed to reach the detection threshold is reduced by one. Thus we estimate that time advance is directly correlated with density for yields above 7×10^{-11}cm^{-3}, namely 10 times the yield corresponding to ~1 breakdown per shot calculated in Fig. 5.3.

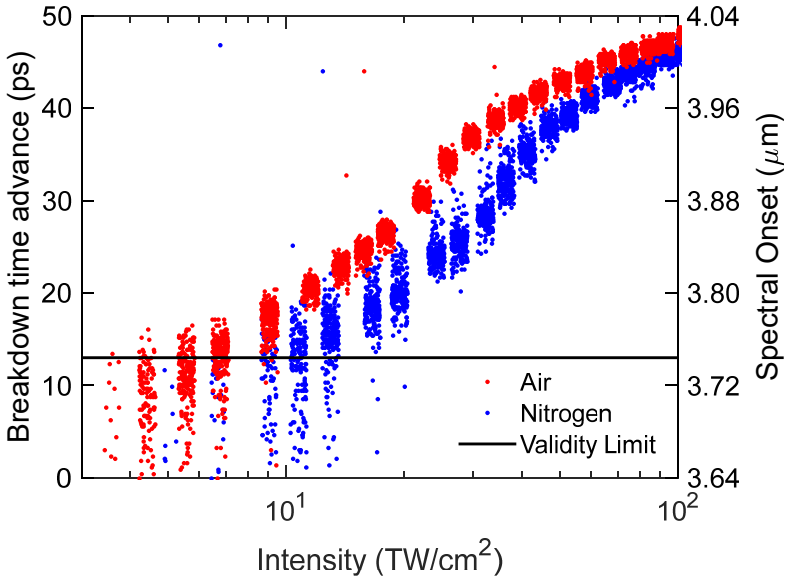

Figure 5.7. Single shot breakdown timing. Each point corresponds to a single probe pulse backscattered spectrum measurement, with the right vertical scale showing the longest wavelength detected, and the associated breakdown time advance shown on the left vertical scale. For low pump intensities, liberated electrons, when they are generated at all, are randomly positioned in the probe breakdown volume, leading to a spread of breakdown times. As pump intensity is increased, multiple seed electrons are generated and more are likely to be found at the peak probe intensity, which visually corresponds to ~13 ps time advance. As more breakdowns occur, they begin to overlap, leading to a deterministic decrease in breakdown timing (>13 ps advance), with the spread in points in that part of the plot determined by fluctuations in probe intensity.

Yields at 100 TW/cm^2 were matched exactly with the standard theoretical rate [50], since measurements of O_2 and N_2 yield in a thin gas jet with a 42 fs, 800 nm pulse at this intensity [222] showed excellent agreement with the theoretical rate over this same intensity range. Interpolating between this yield and the directly measured yields in Fig. 5.3 gives an electron density growth rate of $\nu_i = 0.55\ \mathrm{ps}^{-1}$ during the probe pulse, which was used to calculate the intermediate densities and yields in Fig. 5.8. The dot-dash line indicates the point at which yield extraction based on time advance is meaningful (validity limit), as described above.

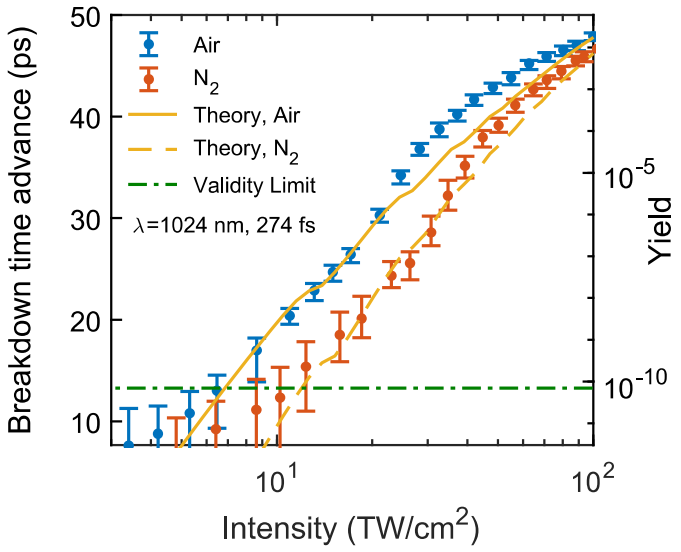

Figure 5.8. Ionization yield measured in breakdown time advance regime (I >10 TW/cm^2). Ionization yields in air and N_2 determined by breakdown time advance Δt_{adv}, with theoretical yields overlaid. The horizontal dot-dashed line indicates the limit above which Δt_{adv} is deterministically correlated with seed electron density. Below this level, individual breakdowns do not overlap during their initial growth phase, and Δt_{adv} is determined by statistical placement of seed electrons in the pump volume. Conversion to yield was benchmarked with imaging results from Fig 5.3 (a) and previous measurements [222]. The points at each intensity give the mean Δt_{adv}, and error bars show the standard deviation of timing measurements due to either statistical placement of seeds (low intensity) or ~5% fluctuations in probe pulse energy (higher intensity).

Measured yields and theory show agreement within a factor of 10 over the full intensity range despite the simplistic assumption of constant ν_i. We note that our chirped probe pulse temporal profile is not exactly square, with a spectral measurement of the OPCPA's mid-IR beam and its near-IR conjugate suggesting more power at the beginning of the pulse, so that collisional heating ($\propto I\lambda^2$) will be stronger at the beginning of the chirped pulse than at the end. Accounting for this would tend to suppress the inferred density slightly throughout the range, bringing it into closer agreement with the theoretical rate.

This backscattering calibration does not rely on simulations, which in turn are dependent on accurate rates for elastic and inelastic collisions, attachment, diffusion, and transport. Nevertheless, a comparison with simulations can give confidence in the general approach. Using a constant intensity of 1.3 TW/cm^2 (the peak probe intensity used for high yield measurements) in a self-consistent set of 0-D equations that track the temperature of avalanching electrons through electron-neutral collisions (heating), and attachment, excitation, dissociative and ionization losses, [128,129] predicts a growth rate of $\nu_i = 0.35\ \mathrm{ps}^{-1}$ after ~2 ps of initial heating needed to reach a steady state plasma temperature of 10 eV, fairly close with the growth rate of $\nu_i = 0.55\ \mathrm{ps}^{-1}$ extracted above. Since the simulations are sensitive to uncertainty in loss rates and collisional heating rates, as well as any departure from the assumption of a thermal electron distribution, this level of disagreement is not unexpected, as we discuss further in Chapter 6.

5.4 Summary and conclusion

Our femtosecond pump ionization yield measurements can be summarized as follows: At lower intensities (Figs. 5.3-5.6, $< \sim 4\ \mathrm{TW/cm^2}$) where the biggest relative contributions from EID ionization are expected, pump wavelength-dependent scaling of yield is consistent with ionization of a low-level contaminant with χ_p~ 6 eV. Neither the wavelength-independent I^2 scaling nor the wavelength-insensitive absolute yield suggested by EID is observed, even when measuring yields a factor of 10^6 lower than those predicted [52-54]. The source of disagreement is unclear, calling for a reexamination of the theoretical work. In the higher intensity range $4\ \mathrm{TW/cm^2} < I <$

$10\ \mathrm{TW/cm^2}$ of Fig. 5.3, the yield at λ=1024 nm transitions into MPI of O_2, while it is in the tunneling regime of the contaminant for λ=3.9μm. In Fig. 5.8, at higher intensities up to 100 TW/cm^2 and the transition from MPI to tunneling, the ionization yield is in good agreement with isolated atom/molecule theory.

Avalanches seeded by low ionization potential contaminants could have an effect on long wavelength infrared filamentation and be consistent with the observations of self-channeling of $\lambda = 10.6\ \mu\mathrm{m}$, TW-level CO_2 laser pulses [21] without the need for EID ionization. Not only can a long-wave IR pulse easily ionize the χ_p~ 6 eV contaminant, but the λ^2 dependence of collisional heating and free electron polarizability [21,54] renders such a pulse quite sensitive to any free electrons it self-generates and their subsequent avalanche growth. We also note that the growth rate, $\nu_i = 0.55\ \mathrm{ps^{-1}}$, extracted from our measurement applies to laser-air interactions with a different wavelength but the same numerical value of $I\lambda^2$, and can be used to benchmark simulations of high intensity, picosecond laser-driven avalanche. We will discuss these possibilities further in Chapter 6, where we combine our avalanche and multiphoton results with a propagation code.

In conclusion, we have shown that avalanche breakdown using picosecond mid-IR probe pulses is a sensitive diagnostic of extremely low electron densities—achieving an unprecedented dynamic range of 14 orders of magnitude, with picosecond and few micron resolution. We measure ionization generated by femtosecond pump pulses in several gases in the atmospheric pressure range and find that the yield at lower laser

intensities $\sim 1\ \mathrm{TW/cm^2}$ is consistent with MPI of a ubiquitous parts-per-trillion contaminant, and is not dependent on predicted many body effects, while yield at higher intensities ($> \sim 10\ \mathrm{TW/cm^2}$) is consistent with MPI or tunneling ionization of isolated molecules. The sensitivity and range of our density diagnostic exceeds performance for all other weakly-ionized plasma density measurements of which we are aware while also avoiding reduced spatial resolution inherent in bulk plasma or longitudinal averaging (as in standard interferometry [224], dispersion interferometry [225], plasma conductivity measurements [226] or optical emission [227]) or reduced temporal resolution (as in microwave scattering [228] and charged particle counting). Such performance is of particular interest for intermediate electron densities (10^8-10^{13} $\mathrm{cm^{-3}}$) present in a variety of weakly ionized plasma systems

Chapter 6: Self-guiding of long-wave infrared laser pulses mediated by avalanche ionization

6.1 Motivation for long wavelength filamentation

Femtosecond filamentation of intense laser pulses in gases and condensed media arises from the interplay of diffraction, Kerr self-focusing, and collapse arrest by plasma-induced refraction, enabling high intensity self-guided propagation over extended distances [2,3]. As discussed in Sec. 1.2.2, filamentation occurs for pulses whose peak power exceeds a critical value $P_{cr} = 3.77\lambda^2/8\pi n_0 n_2$ for Gaussian beams, where λ is the laser wavelength, and n_0 and n_2 are the medium's linear and nonlinear indices of refraction. In "standard" filamentation, self-induced Kerr lensing focuses the beam until multi-photon or tunneling ionization of the medium and associated plasma defocusing arrests pulse collapse. As input power is increased well beyond P_{cr}, the beam is unstable to breakup into multiple filaments, limiting the peak power delivered in a single high intensity channel. The $P_{cr} \propto \lambda^2$ scaling indicates higher multi-filamentation thresholds for longer wavelengths, stimulating recent interest in mid-IR and long-wave IR (LWIR) filamentation [21,22,44-47,53,54,229]. For LWIR pulses, new mechanisms have been proposed for collapse arrest, including the formation of optical shocks and harmonic walk-off for short (<1 ps) pulses [45-47] and avalanche ionization seeded by many-body induced ionization for longer (>1 ps) pulses [21,53,54].

In this Chapter, we present propagation simulations showing that avalanche ionization at discrete breakdown sites, likely seeded by aerosols, is essential for atmospheric self-guiding of moderate intensity LWIR pulses with few-millimeter beam widths [40], consistent with recent experiments [21]. Our simulations incorporate the latest understanding of LWIR ionization processes in air provided by the experiments covered in Chapters 4–5 [37-39]. In general, avalanches proceed as localized plasma breakdowns centered either on aerosols or electrons generated by tunneling ionization early in the pulse. In both cases, refraction from these discrete plasma sites is manifested through forward Mie scattering [230]. We first discuss a time-resolved temperature based model of avalanche growth, adapted from recent work [128-130] to account for the growth of these isolated sites in high intensity LWIR regime. We then incorporate these spatially discrete, transient breakdowns in our propagation simulations, a more realistic approach than the continuous plasma background assumed in previous models. In the absence of aerosols, we find that self-focusing continues until it is arrested by standard tunneling ionization, with avalanche-generated plasma refracting only the trailing edge of the pulse. Aerosols, on the other hand, lead to enhanced, *saturable* ionization early in the pulse, enabling avalanche-mediated collapse arrest and channeling of few picosecond LWIR pulses at moderate intensities.

6.2 Temperature model for avalanche growth rates

In avalanche breakdown, free electrons undergo laser-driven dephasing elastic collisions with neutral molecules until they have enough kinetic energy to collisionally ionize the neutrals in a cascading process. The growth in the local number of electrons

at an avalanche site is $n_e = n_{eo}e^{\nu_i t}$ where $\nu_i = \langle\sigma_i v\rangle N_n$ is the electron collisional growth rate, n_{eo} is the local number of seeds, N_n is the local neutral molecule density, and $\langle\sigma_i v\rangle = \int_0^\infty dv\, f(v)\sigma_i(v)v$ for electron velocity distribution $f(v)$ and collisional ionization cross section σ_i. Growth saturates as the neutral density is depleted ($N_n = N_{no} - N_e$) for increasing electron density N_e. Under thermal quasi-equilibrium, the electron velocity distribution is given by $f(v) = \alpha v^2 \exp(-mv^2/2k_B T)$ for temperature T, where k_B is Boltzmann's and α is a normalization constant. In order to achieve this state during laser heating, the electron-electron collision frequency ν_{ee} should be greater than the electron heating rate $\tau_h^{-1} \sim (K_e/(2U_p\nu_{en}))^{-1}$ for average electron kinetic energy $K_e = \frac{1}{2}m\langle v^2\rangle$, where τ_h~1 ps is the heating timescale under our conditions. Using $\nu_{ee}[\mathrm{s}^{-1}] \approx 2.9 \times 10^{-6} \ln\Lambda\, N_e/T^{3/2}$, where $\ln\Lambda \approx 23 + \ln(T^{3/2}N_e^{-1/2})$ for N_e in cm^{-3} and T in eV [212], K_e ~10-100 eV and $\ln\Lambda \sim 6-16$ under our simulation conditions gives $\nu_{ee} > \tau_h^{-1}$ only for $\overline{N_e} \gtrsim 10^{18}$ cm^{-3}, or near saturation of the breakdown.

Our goal is to couple a model of avalanche at discrete sites to a propagation simulation. Given the lack of true thermal quasi-equilibrium, the best, albeit forbidding, approach would be to solve the Boltzmann equation for the full time-resolved electron distribution function [106,125,231,232], accounting for angle-resolved scattering over wide primary and secondary electron energy ranges. However, some of these rates are not well known, and coupling such an approach to propagation codes will vastly increase computation time. Instead, we describe a simpler temperature-based model

used here and in previous chapters. Use of a thermal distribution in our calculations is still permissible over a much wider range of density because $\nu_{en} \gg \nu_{ee}$ during the fast rising portion of the breakdown. Momentum transfer collisions with neutrals impart an average energy of $2U_p$, but a single collision can add to (or deduct from) an electron's energy over a wide range, and thus have a "thermalizing" effect similar to electron-electron collisions even though there is average net energy gain. This is evident in calculations [233] and measurements [234,235] of inverse bremsstrahlung in fully ionized plasmas giving super Maxwellian distributions, namely $f_n(v) = \alpha_n v^2[\exp(-mv^2/2k_BT)]^n$ for integer $n \geq 1$, although in the present case, inelastic collisions would further perturb the velocity distribution. We show below that our temperature-based model still contains the essential physics to explain recent LWIR propagation experiments, and that it is insensitive to our assumption of a Maxwellian electron energy distribution.

First we consider electron heating. A free electron in a laser field has a cycle-averaged kinetic energy $U_p \cong 0.93\ I\ [\mathrm{TW/cm^2}](\lambda[\mu\mathrm{m}])^2$ eV, which is transferred into incoherent motion through electron-neutral collisions at rate ν_{en}. The Lorentz-Drude model gives a heating rate per electron of $W_{coll} = 2U_p\omega^2\nu_{en}(\omega^2 + \nu_{en}^2)^{-1} \sim 2U_p\nu_{en}$, for laser frequencies $\omega/\nu_{en} \gg 1$ at atmospheric pressure. Electron heating is offset by losses, including rovibrational and electronic excitation, dissociation and ionization losses of energy χ_l and excitation rate ν_l in N_2 and O_2 [112,113]. The rate of change in total system internal energy density is then

$$\frac{dU}{dt} = \frac{3}{2}\frac{d(k_B N_e T)}{dt} = \frac{3}{2}k_B\left(\frac{dN_e}{dt}T + \frac{dT}{dt}N_e\right) = 2\nu_{en}N_e U_p + \nu_i N_e U_p - \sum_l N_e \nu_l \chi_l \,. \quad (6.1)$$

This central equation is drawn from recent work on nanosecond breakdowns driven by $\lambda > 10$ μm pulses [128-130], which together with tabulated loss rates [211] was used for simulations in Chapters 4-5. Here, we have added the term $U_p(dN_e/dt) = \nu_i N_e U_p$, which accounts for the effective heating of electrons collisionally released at random times in the laser cycle, since both ν_i and U_p are considerably larger than in this previous work. We specifically ignore diffusive losses for laser spot sizes much larger than r_d: because electron-neutral interactions dominate during the fast rising portion of the breakdown, and the neutral density is uniform across a breakdown site, our model predicts a very weak temperature gradient. Once a local breakdown nears saturation, however, the rates of electron-electron and electron-ion collisions rapidly increase as neutrals deplete. As such, strong temperature gradients will emerge, indicating limited validity at this point. Rearranging gives

$$\frac{dk_B T}{dt} = \frac{2}{3}\left(2U_p\nu_{en} + \nu_i U_p - \Sigma_l \nu_l \chi_l\right) - \nu_i T \ , \quad (6.2)$$

where $N_e^{-1}(dN_e/dt)T = \nu_i T$ tracks thermal energy redistribution in a growing electron population [128-130]. For the present simulations, we have directly integrated relevant cross sections in N_2 and O_2 [112,113] over a Maxwellian distribution up to $k_B T$=1 keV instead of relying on low temperature (<30 eV) tabulated rates [128-130,211]. The heating rate $2U_p(2\nu_{en} + \nu_i)/3$ and loss rate $2(\Sigma_l \nu_l \chi_l)/3 + \nu_i T$ in Eq. (6.2) are plotted vs. $k_B T$ on the left scale in Fig. 6.1 for a λ=10.2 μm, 1 TW/cm^2 pulse. The right scale shows the ionization rate $\nu_i(k_B T)$ as a function of temperature and, for

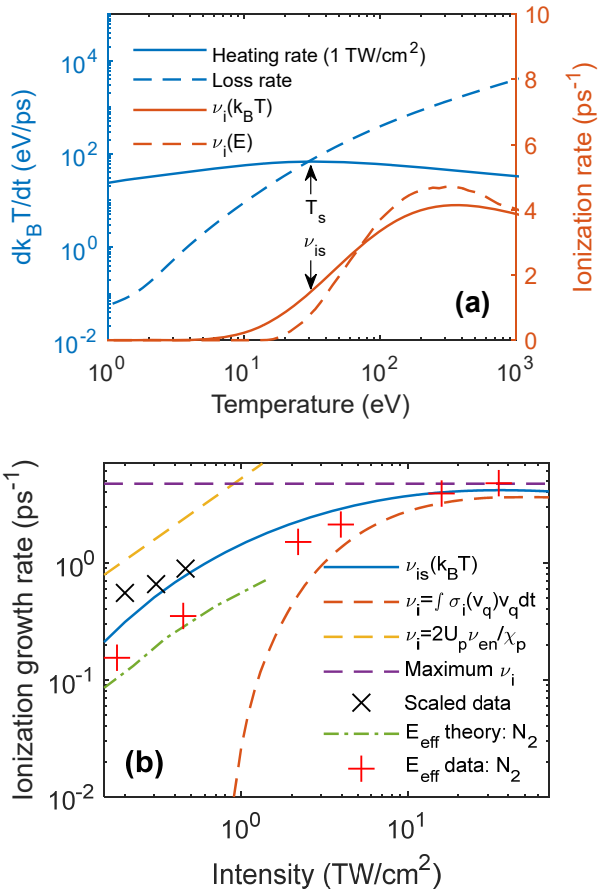

Figure 6.1. (a) Temperature-dependent heating rate (for λ=10.2 μm, 1 TW/cm^2) $(dk_BT/dt)_{heating} = 2U_p(2\nu_{en}+\nu_i)/3)$ and loss rate $|(dk_BT/dt)_{loss}| = 2(\Sigma_l\nu_l\chi_l)/3 + \nu_iT$ (left scale, log) in air. The ionization rate ν_i (right scale) is shown as a function of electron energy E and temperature T. (b) Quasi-static ionization growth rate ν_{is} extracted from the temperature model (solid blue curve). Dashed curves indicate limiting values of the growth rate based on no collisional heating (red), no energy loss (yellow), and the peak value of the ionization growth rate (purple). Scaled rates from Boltzmann theory for DC breakdowns in N_2 (dash-dot) [231] and from experimental results in air at λ=4 μm (×) [38,39] and DC experiments in N_2 (+) [231,238] are given for comparison.

comparison, the rate $\nu_i(E)$ for a monoenergetic electron distribution. For sudden intensity transients, temperature must be tracked as a function of time using the net heating rate, such that avalanche growth lags the intensity profile [236]. For a sustained constant intensity pulse, or for pulses whose temporal changes are long compared to heating times (characteristic time $\tau \gg \tau_h$), the point where the heating and loss rates

cross ($dk_BT/dt = 0$) defines a quasi-static equilibrium temperature T_s [37,129] and an associated quasi-static growth rate ν_{is}.

Figure 6.1(b) plots the calculated quasi-static growth rate ν_{is} (achieved after time $\tau \gg \tau_h$) as a function of intensity, compared with limiting cases and other theoretical and experimental results. The horizontal dashed line indicates the maximum achievable growth rate matching the peak ionization rate in Fig. 6.1(a). The upper (yellow) dashed curve indicates growth rates assuming that laser heating immediately results in ionization of species with ionization potential χ_p ($\nu_i = 2U_p\nu_{en}/\chi_p$). This assumption is a common approach used in propagation models [2] due to its simplicity, but it ignores energy losses [111] and the $-\nu_i T$ term discussed above, and thus greatly overestimates growth rates. The lower (red) dashed curve shows rates assuming electron velocities are given solely by quiver motion in the laser field, $v_q(t) = (eE/m\omega)\cos(\omega t)$, as appropriate for $\tau \ll {\nu_{en}}^{-1}$ [237]. These limits define two regimes: above 5 TW/cm^2, ν_{is} is insensitive to details of the model, since it is tightly bounded by the limiting cases. At lower intensities (1-5 TW/cm^2), ν_{is} is within a factor of ~10× of the limiting cases.

Absent full Boltzmann calculations for our conditions, we scale from other theoretical and experimental results. For $\omega \gg \nu_{en}$, the heating rate is expected to scale directly with the ponderomotive energy $U_p \propto I\lambda^2$, such that avalanches at λ=4 μm can be compared with those at λ=10 μm driven at a factor of $(10/4)^2 = 6.25$ lower intensity. The experiment presented in Chapter 5 directly measured the growth rate

$\nu_{is} = 0.55\ \mathrm{ps}^{-1}$ for λ=4 μm at 1.3 TW/cm^2 [39], which is scaled and plotted as the lowest × point in Fig. 6.2. The remaining two × points are calculated from backscatter-based breakdown timing measurements in Chapter 4 [38], assuming that the same total growth $n_f/n_0 = \exp(0.55\tau(ps))$ is required to reach detection for total pulse length $\tau = 50$ ps. Due to the difficulty in comparing different experimental setups and backscatter geometries, these points are more uncertain, but still show that the temperature model predicts the general trend with reasonable accuracy. For DC breakdowns, comparisons can be made using two experiments that have the same effective electric field, namely, $E_\omega \nu_{en}/\omega N_n = E_{DC}/N_n$ for electric field E_ω of frequency ω scaled by the neutral density N_n in the experiment, where there are different conventions for whether the peak or rms field should be used [111,114,128]; here we scale by the peak field. Applying this scaling to DC breakdown theory [231] and experiments [231,238] in pure N_2 gives the remaining data in the plot, and again shows agreement within a factor of 2. For LWIR beam, multi-photon effects discussed in Sec. 1.4.3 are not expected to contribute to the growth rate [111], such that DC comparisons are permissible.

Below in Fig. 6.2, we plot ionization growth rates ν_{is} calculated from several different electron velocity distributions: a Gaussian distribution centered around a nonzero energy, and a super Maxwellian of order $n = 2$. As above, ν_{is} is found for each distribution by finding the central energy/super-Maxwellian temperature where heating and loss rates balance as a function of intensity. These changes in distribution shape do not noticeably shift rates calculated using a standard Maxwellian ($n = 1$) .

Our approach assumes that only elastic momentum transfer collisions contribute to electron heating, but an electron which undergoes an inelastic collision will also dephase with respect to the laser field similar to the collisional heating process for elastic collisions. Correctly incorporating such additional heating is difficult [239], and again suggests a Boltzmann approach. However, if we assume that including inelastic collisions effectively doubles the collisional heating rate, the ionization rate is moderately increased (× 2.5) at ~0.1 TW/cm^2, with a smaller relative change at >1 TW/cm^2.

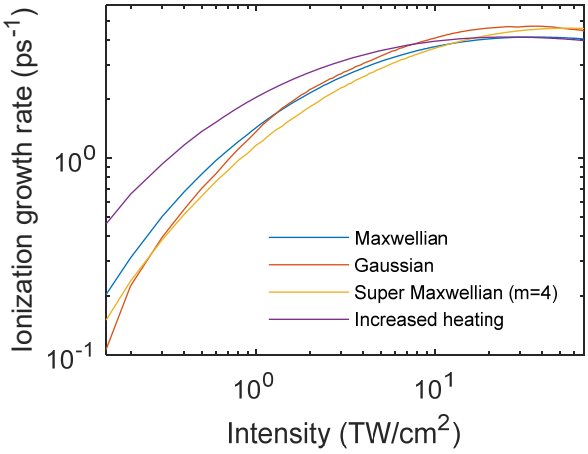

Figure 6.2. Quasi-equilibrium ionization growth rate ν_{is} vs. laser peak intensity (for λ=10 μm) for several electron velocity distributions. Purple curve: rough estimate of effect on ν_{is} of inelastic collisions.

These rates calculated using non-Maxwellian electron distributions or including inelastic contributions to collisional heating give similar variation (~2×) in ν_{is}, of the same order as the spread in scaled experimental and theoretical data. Thus, using a Maxwellian distribution should still allow accurate discrimination between high intensity (>10 TW/cm^2) and low intensity (0.5-5 TW/cm^2) regimes, while also

incorporating the delayed response [236] of avalanche growth to intensity transients. When applied to breakdowns in Chapters 4-5, it should also give approximate values of the breakdown threshold and time advance.

6.3 Refractive index of isolated avalanche sites

As discussed in Sec. 1.4.4, at an avalanche site, electron diffusion gives a characteristic plasma radius $r_d = \sqrt{2\tau k_B T_e/m_e \nu_{en}} \sim 0.3\sqrt{\tau[\text{ps}]\, T_e\,[\text{eV}]}$ μm for electron temperature T_e and electron-neutral collision rate $\nu_{en} \sim 2-4$ ps^{-1} (for 2 eV $< T_e <$ 1 keV) [112,113]. In particular, electron diffusion is limited to ~5 μm even for $k_B T_e \sim$100 eV for a <3.5 ps pulse, so we use $r_d \sim$ 5 μm as a baseline for our propagation simulations below. In general, breakdown will proceed as isolated avalanche sites surrounded by neutral air unless the initial seed electron density satisfies $N_{e0} > 1/r_d^3$ ~10^9–10^{11} cm^{-3}, for which the laser effectively interacts with a continuous plasma.

During laser propagation, the absolute changes in refractive index ($\Delta n = |n-1| \sim \overline{N_e}/2N_{cr}$) and propagation phase ($|\Delta\Phi| = 4\pi a|\Delta n|/\lambda$) across an individual breakdown site of radius a are small ($\ll 1$) for average plasma density well below critical density, $\overline{N_e} \ll N_{cr} = 1.1\times10^{21}$ cm$^{-3}/\lambda^2$ [μm]. Thus scattering occurs in the Rayleigh-Gans (RG) regime ($|\Delta n| \ll 1$, $a \ll \lambda/|\Delta n|$) [230]. An effective refractive index is then calculated from the forward scattering amplitude [230] $S(0)$ of an ensemble of scatterers of number density N_{sc}, giving $n_{eff} = 1 + N_{sc}V\Delta n = 1 - N_{sc}V(\overline{N_e}/2N_{cr})$, for average breakdown site volume V, with a detailed derivation in Appendix A.2. This equals the index of a continuous plasma of density $N_{sc}V\overline{N_e}$, as

covered in previous work on exploding nano-plasmas [240]. The RG approximation breaks down as $\overline{N_e}$ approaches N_{cr} at individual breakdown sites, necessitating the calculation of Mie scattering amplitudes [230]. This limits our use of RG-based n_{eff} to breakdowns with $\overline{N_e} < N_{cr}/2 \sim 5 \times 10^{18}$ cm^{-3} , corresponding to ~6×10^9 electrons in a $a = r_d = 5$ μm breakdown volume, for which the Mie and RG models give effective refractive indices within 20%. Above this density, the increase in side scattering (extinction) and dependence on breakdown size limit the fidelity of our simulations. More information on scattering losses and the validity of the RG approximation is given in Appendix A.2.

6.4 Seed sources for LWIR avalanche

The initial electron population needed to seed LWIR avalanche in air can originate from tunneling ionization, which depends extremely sensitively on intensity as seen in Fig. 6.3. The presence of an ubiquitous air contaminant with $\chi_p \sim 6$ eV, as recently measured at relative concentrations ~10^{-9}–10^{-11} [39], dominates ionization below ~10 TW/cm^2. Separately, aerosols (solid density particulates including dust, water droplets/fog, etc.) are readily ionized due to near-field enhancement or existing static charge. We recently estimated aerosol concentrations of $\sim 10^4$ cm^{-3} in our lab air by measuring the number of avalanches inside a breakdown threshold volume with and without particulate filtering [38]. Other detailed measurements of aerosols in indoor environments show a range of number concentration (N_{sc}~10^2–10^4 cm^{-3}) and

particle size (~0.1-10 μm) [241-243]. In general, aerosol concentrations are higher in outdoor "field" conditions envisioned for applications of self-guiding.

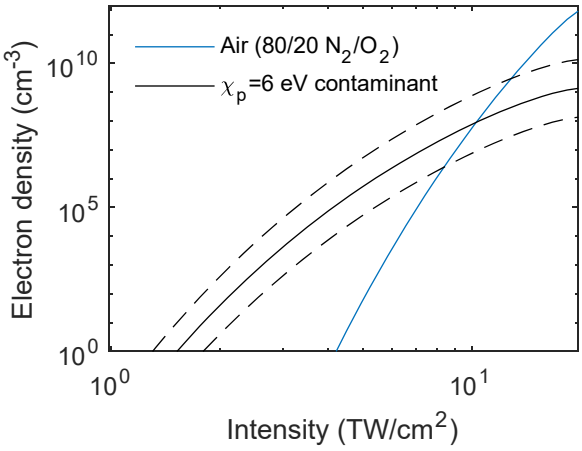

Figure 6.3. Generated electron density vs. peak intensity from ionization of air and a $\chi_p \sim$ 6 eV contaminant [39] by a λ=10.2 μm, 1 ps FWHM Gaussian pulse. Dashed lines indicate bounds of approximate uncertainty in the number density of contaminant species [39].

We can estimate the requirements for seed number density and growth to enable collapse arrest and self-guiding by equating the nonlinear index shifts associated with Kerr focusing and plasma refraction: $\Delta n_{Kerr} = \Delta n_{eff} \rightarrow n_2 I = N_{sc} V \overline{N_e} / 2N_{cr}$. For n_2 $\sim 5 \times 10^{-19}$ cm^2/W [244,245] and $V = 4\pi r_d^3/3$, we estimate $(N_{sc} V \overline{N_e})$ $\sim 10^{13} \times$ $I[\mathrm{TW/cm^2}]$ cm^{-3}. At $I = 1$ TW/cm^2, this gives $N_{sc} \sim 10^4$ cm^{-3} breakdown sites avalanched to $\overline{N_e} \sim N_{cr}/2$, the limit of our effective index approximation, or a larger N_{sc} avalanched to a lower terminal $\overline{N_e}$. This estimate applies equally well to a continuum density $N_e = \sim 10^{13} \times I[\mathrm{TW/cm^2}]$ cm^{-3}.

6.5 Propagation simulations

Propagation simulations were conducted by combining the avalanche model ($n_e = n_{eo} e^{\nu_i t}$ plus Eq. (6.2)) with a 2D+time axisymmetric unidirectional pulse

propagation equation (UPPE) solver [26,246], with a detailed description of implementation in Appendix A.3. Our simulation parameters match a recent experiment with 3.5 J, 3.5 ps, λ=10.2 μm pulses ($P\sim 2P_{cr}$) focused to a 4 mm FWHM spot (4 TW/cm^2, ~5 m Rayleigh range) [21]. The pulses initially self-focused and created a tenuous visible plasma over ~5 m, followed by beam expansion to ~1 cm FWHM and self-guiding over ~30 m at peak intensities ~1 TW/cm^2, accompanied by pulse shortening to ~1.8 ps. Since generation of seed electrons from tunneling ionization is negligible at this intensity, the avalanche-generated plasma responsible for self-guiding was thought to be seeded by many-body induced ionization [21,53,54]. Measurements in Chapter 5 [39] cast doubt on this seed source and pointed instead to tunneling ionization of contaminants or aerosols.

6.5.1 Aerosol-free air

We first consider aerosol-free air, initializing propagation at the focus (4 mm FWHM, 4 TW/cm^2). The initial electron population was set at $N_{e0} = 10^4$ cm^{-3}, but results were insensitive to this value. Additional seed electrons were contributed by tunneling ionization [50] (see Fig. 6.3). Figure 6.4(a) shows the peak intensity, pulse temporal FWHM and beam FWHM, and plasma density (at the peak intensity and after the pulse) versus propagation distance. The pulse self-focuses to ~20 TW/cm^2 after 2.25 m of propagation while also undergoing self-shortening to ~2 ps as the front and rear diffract. At this point, substantial tunneling ionization occurs during the leading edge of the pulse, generating a seed electron density $N_{sc}\sim 10^{12}$ cm^{-3} $> r_d^{-3}$, in the

continuum density regime. This is seen in Fig. 6.4(b), which shows the on-axis intensity and plasma density after 2.25 m of propagation. The falling edge of the pulse drives continued avalanche to high density behind the pulse, as the effective density $N_e = N_{sc}V\overline{N_e}$ continues growing above the density N_{sc} of sites generated through tunneling. This rising density further refracts the pulse's falling edge, leading to the shortened pulses shown in the inset plots of Fig. 6.4(b) at 2.25 m and 3 m. The final sub-picosecond pulse continues to filament in the tunneling ionization regime, with peak intensity $I \geq 20$ TW/cm^2 and ~1 mm FWHM beam size [44,47], very different than the ~1 TW/cm^2, 1 cm beam observed in [21]. Since our envelope-resolved simulation does not have sufficient spatial resolution to track further propagation with high fidelity, we terminated this simulation at ~3 m.

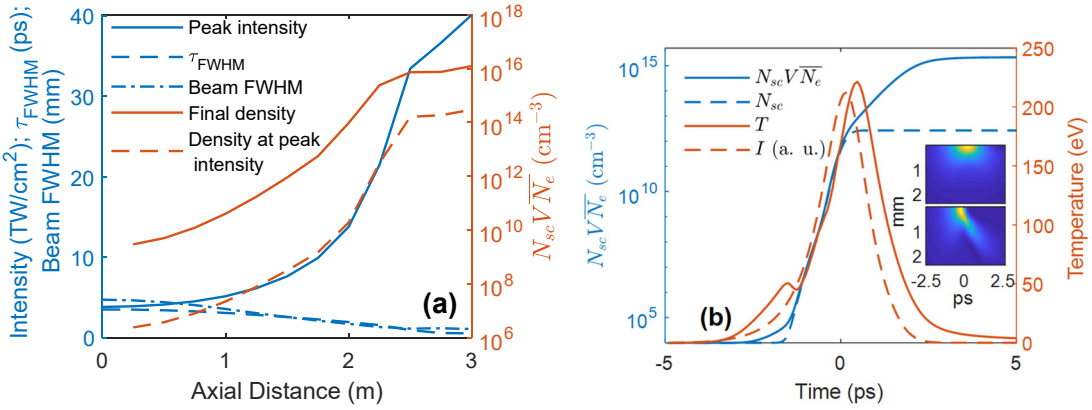

Figure 6.4. (a) Pulse parameters over 3 m of propagation. Left axis: pulse peak intensity (TW/cm2, solid) and beam FWHM and temporal FWHM (mm, ps; dashed), right axis, plasma density at the intensity peak of the pulse (dashed) and after the pulse has completely passed (solid). (b) On-axis intensity and plasma density/temperature after 2.25 m of propagation, showing a rapid increase in the density N_{sc} of breakdown sites due to seed generation by tunneling (dotted blue line), followed by slower increase in volume average density $N_e = N_{sc}V\overline{N_e}$ due to avalanche. Temperature (right scale) roughly follows the pulse intensity profile. Inset plots show spatiotemporal intensity profiles (normalized to peak intensity) at 2.25 m (top) and 3 m (bottom).

The failure of avalanche growth in aerosol-free air to arrest collapse before the onset of tunneling is inevitable given the electron density growth rates in Fig. 6.1 (b) and tunneling yields in Fig. 6.3. Even for the maximum growth rate of 4.7 ps^{-1} (predicted only for $I \gtrsim 10\mathrm{TW/cm^2}$ in Fig. 6.1 (b)), an initial electron density $N_{eo}\sim10^9$ is needed to reach the effective density $N_{sc}V\overline{N_e} = 10^{13}$ cm^{-3} we estimated for self-guiding at 1 TW/cm^2. This initial density in turn requires tunneling at $\sim10\ \mathrm{TW/cm^2}$ in the leading edge of the pulse as shown in Fig. 6.2. Thus, it is unlikely that the ~1 TW/cm^2 channeling observed in [21] is stabilized by avalanche from electrons liberated by tunnel ionization.

6.5.2 Aerosol initiated avalanche

Avalanche ionization in aerosols, however, introduces a new propagation regime consistent with self-guiding at modest intensity. For the near-solid density of an aerosol particle, the electron-neutral collision rate ($\nu_{en}\sim10^{15}\mathrm{s^{-1}}$) is much higher than infrared frequencies ($\omega_{en}/\nu_{en} \ll 1$) [232,247]. Thus, as discussed in Sec. 1.4.1, collisional heating $W_{coll} \propto I\nu_{en}^{-1}(1+(\omega/\nu_{en})^2)^{-1} \approx I/\nu_{en}$ becomes wavelength-independent for $\lambda \gtrsim 300$ nm, suggesting ionization rates $\nu_{is} = 10 \times I[\mathrm{TW/cm^2}]$ ps^{-1} calculated for fused silica breakdowns at λ= 1 μm are representative [232]. Using a rate directly proportional to intensity, rather than tracking temperature evolution, is permissible since the pulse length $\tau \gg \tau_h^{-1}$ as discussed above in Sec. 6.2. To model ionization of sub-wavelength-sized particles, we apply $I \to 4I$ to account for $2\times$ electric field enhancement near a dielectric sphere with a dielectric constant $\varepsilon\sim4$. This

approach then predicts that at $I = 0.5\ \mathrm{TW/cm^2}$, growth will proceed from an initial electron seed in a 0.2 μm diameter aerosol to full single ionization (10^8 electrons) in $\Delta t \sim \ln(10^8)\,\nu_{is}^{-1} \sim 1$ ps. This is consistent with aerosols avalanching to saturation during the rise of the pulse and then avalanching more slowly as plasma expands into the surrounding air..

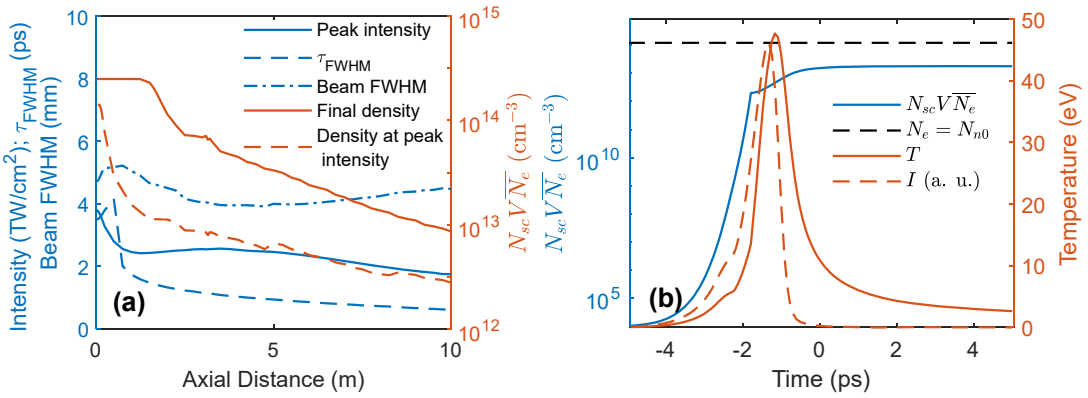

Figure 6.5. (a) Simulation including aerosol-enhanced avalanche for initial aerosol density of 2×10^4 $\mathrm{cm^{-3}}$. (b) On-axis intensity and plasma density/temperature after 6 m of propagation, showing a rapid increase in density due to breakdowns in aerosols, followed by slower avalanche in air, with volume average density reaching ~10^{13} $\mathrm{cm^{-3}}$ near the intensity peak of the pulse, broadly consistent with self-guiding as shown above. The horizontal dashed line indicates full ionization of the breakdown sites.

Accordingly, we conduct a second set of propagation simulations for a range of initial aerosol densities (N_{sc}~10^3–3×10^4 $\mathrm{cm^{-3}}$), with results for $N_{sc} = 2 \times 10^4\ \mathrm{cm^{-3}}$ shown in Fig. 6.5. For simplicity and specificity, we assume a uniform aerosol radius of $a = 0.2$ μm. In these simulations, the pulse is immediately shortened as energy in the falling edge is scattered off-axis by the rapidly formed plasmas. After this transient, aerosol-enhanced plasma generation is sufficient to arrest self-focusing, resulting in self-guiding of $0.5 - 1.5$ ps pulses at ~2-2.5 $\mathrm{TW/cm^2}$ over ~10 m.

Figure 6.5 (b) shows on-axis plasma density and pulse shape at 6 m, after onset of self-guiding. In contrast to Fig. 6.4, the aerosols provide a rapid increase in $N_{sc}V\overline{N_e}$ that arrests collapse over the full pulse. Ionization saturation limits further pulse shortening, which would reduce avalanche for $\tau < \nu_{en}^{-1}$. Thus avalanche breakdown of aerosols appears essential for long distance stable self-guiding of moderate intensity picosecond LWIR pulses.

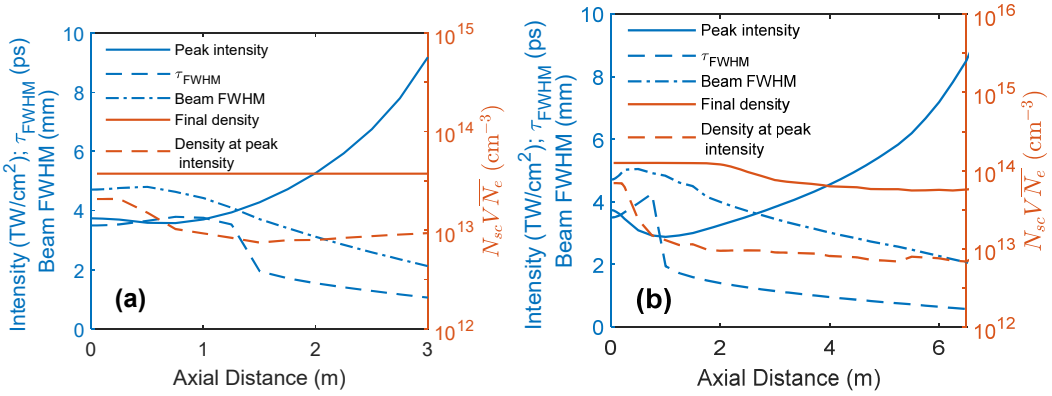

Figure 6.6. Simulations including aerosol-enhanced avalanche for initial aerosol densities (a) $N_{sc} = 3 \times 10^3$ cm^{-3} and (b) $N_{sc} = 10^4$ cm^{-3}.

Additional simulation runs with initial aerosol densities less than $N_{sc} \sim 2 \times 10^4$ cm^{-3} are shown below in Figure 6.6. While the run at (a) $N_{sc} = 3 \times 10^3$ cm^{-3} shows slightly slower self-focusing than the case with no aerosols, the generated density is still insufficient to fully arrest pulse collapse, leading to a rapid increase in intensity as the pulse self-focuses towards the end of the run. For (b) $N_{sc} = 10^4$ cm^{-3}, the intensity decreases slightly before increasing again and trending upwards at the end of the 6.5 m simulation window. Further, since (a) and (b) show continued self-focusing

(arrested only by tunneling ionization), the generated avalanches always exceed $\overline{N_e} > N_{cr}/2$ by the end of the pulse, limiting the validity of the propagation simulations.

6.6 Summary and conclusion

While our simplifications have made a complex problem tractable and provided a clear physical picture for the role of aerosols, our work calls for more detailed studies in several areas. In particular, because $\overline{N_e} = N_{cr}/2$ is reached and exceeded at breakdown sites during the pulse, and because the saturated aerosol plasma can further heat through electron-ion collisions and rapidly expand into the background air, the RG model breaks down and would need to be replaced by a full scattering computation coupled to plasma dynamics. Additionally, while we have considered wavelength independent avalanche in aerosols for $\omega/\nu_{en} \ll 1$, Brunel or "vacuum" heating [248] at the particle-air interface may introduce additional wavelength-dependence

In summary, we have developed a model for self-guiding of long wavelength infrared (LWIR) picosecond laser pulses stabilized by avalanche ionization from discrete plasma breakdown sites. In aerosol-free air, we find pulse self-focusing is arrested by tunneling ionization of air constituents and contaminants, leading to high self-guided intensities and narrow channel diameters, inconsistent with recent experiments [21]. Aerosol-centered avalanche sites, however, enhance plasma generation, which enables self-guiding at moderate intensities with larger channel diameters. Future experimental propagation studies of picosecond LWIR pulses in controlled atmospheres could help quantify the role of aerosols in self-channeling.

Chapter 7: Summary and Future Work

7.1 Summary

Throughout this dissertation, we have examined the advantages of mid-IR lasers for several high intensity laser-plasma applications. In Chapter 3, we presented the first results for mid-IR driven laser wakefield acceleration. Favorable wavelength scaling enabled near-critical and above-critical density interactions in moderate density gas jets and a detailed scan of self-focusing lengths. Compressed mid-IR laser pulses open up the opportunity for resonant plasma wake excitation in atmospheric density range gas jets and the generation of quasi-monoenergetic electron beams with modest pulse energies. LWFA with mid-IR pulses also enables easier probing of the larger wake structures. In Chapter 4, we demonstrated that mid-IR driven avalanche breakdown enables single-electron detection sensitivity in atmospheric density range gases, employing both imaging and breakdown timing diagnostics. We applied this ultra-sensitive detection method to determine charge densities induced in the vicinity of a radioactive source by its decay products (here, α-particles), and to test three independent remote diagnostics for radioactive detection. We found that breakdown timing, as encoded in the backscatter of a chirped mid-IR avalanche driver pulse, was the most robust measurement, with demonstrated insensitivity to complex plasma dynamics and propagation effects. Our currently available mid-IR laser pulse energy indicates that standoff distances of 10-100 m are possible in near-term experiments, while increased pulse energy could allow even greater standoff distances. In Chapter 5, we applied avalanche detection to free electrons generated by MPI and tunneling

ionization induced by a femtosecond pump pulse, enabling detection of ionization yields over an unprecedented 14 orders of magnitude and uncovering the presence of a ubiquitous low density molecular contaminant with ionization potential $\chi_p \sim 6$ eV. These measurements also verified that standard MPI/tunneling ionization rates for isolated atoms and molecules are operative even in atmospheric density gases, in contrast to predictions of recent theories suggesting that many-body effects could increase the ionization rate by orders of magnitude at modest (~1 TW/cm^2) laser intensities. In Chapter 6, armed with insights from our avalanche breakdown experiments, we performed the first simulations of high intensity nonlinear pulse propagation through a medium composed of discrete plasma breakdown sites (seeded by aerosols). In the absence of aerosols, pulse self-guiding was mediated by tunneling ionization, leading to much higher intensity and narrower guiding channels than seen in recent picosecond LWIR pulse self-guiding experiments. Discrete aerosol-seeded breakdown sites enabled avalanche-mediated self-guiding at modest intensities, agreeing with experiments. These simulations call for more detailed study of aerosol-initiated breakdowns in the picosecond regime, with application to all applications of self-guided LWIR pulses in outdoor environments.

7.2 Ongoing and Future Work

Beyond the work described in this dissertation and its potential applications, we have conducted a number of collaborative projects which further demonstrate favorable wavelength scaling in the mid-IR. Here we briefly review two areas of study, and describe possible future work.

7.2.1 Broadband THz generation

The terahertz domain, broadly defined as encompassing frequencies from 0.3 to 30 THz ($\lambda = 10\ \mu\text{m} - 1\ \text{mm}$), overlaps many rotational resonances in molecules, vibrational frequencies in large macromolecules, and resonances in novel semiconductor nanostructures, with applications in linear and nonlinear spectroscopy and imaging, biological systems, nonlinear optics, and high field physics [249]. However, powerful THz sources are far more limited than those in the mid-IR, requiring complicated and low efficiency schemes for frequency conversion from shorter wavelength laser drivers.

One promising route for generating powerful, broadband THz pulses involves driving currents in air plasma generated through tunneling ionization. In order to radiate at THz range frequencies, these laser-driven electrons must accelerate on a 100 fs-1 ps timescale, much slower than the electron quiver period in the laser field (~1-10 fs). When a laser pulse is focused together with its second harmonic, a transient, directional photocurrent is driven due to the broken symmetry of the field, with maximum THz emission predicted for a phase delay of $\pi/2$ between the ω and 2ω pulses [5,6]. In collaboration with the Kim group at Maryland, we demonstrated a record ~1% laser-to-terahertz conversion efficiency using a λ_1=3.9 μm/ λ_2=1.95 μm two-color pulse with phase control between the two beams [26]. Experiments from another group showed similar THz generation efficiency [27]. Prior 2-color experiments with NIR drivers had achieved conversion efficiencies $10^{-4} - 10^{-3}$ [26,250], so use of mid-IR drivers was a significant improvement. In addition, since the 3rd-9th harmonics of our λ=3.9 μm

beam lie entirely in the visible and near-infrared, we were able to easily measure them and understand their generation mechanism [251]. Other routes for generating strong THz include laser driven organic crystals [252], or spectral downshifting in strongly-driven plasma wakes, as observed in [253]. The second approach would also allow us to use THz generation as a probe of wake dynamics for our near-critical density laser wakefield accelerator.

7.2.2 RF generation

Radio frequency emission, spanning from the THz region down to <2 GHz, has also been observed from filaments and laser plasmas in air [7,254,255], but generation mechanisms have remained in dispute. In collaboration with researchers from the Air Force Research Laboratory, we determined that RF yield from mid-IR air filaments are greatly enhanced ($\gtrsim$10×) compared to those driven at λ=800 nm [29], scaling supported by detailed simulations that identifies the radiation mechanism as longitudinal currents excited along the length of the plasma filament [256]. At the same time, we also found that RF generation driven by two-color pulses is also enhanced under $\omega - 2\omega$ relative phase control, and produces a different angular emission pattern [28]. However, the phase dependence and spectral content was a function of emission angle, suggesting further work to see if this behavior is related to the THz emission mechanism described above. Conducting laser driver wavelength-based comparisons of RF generation in atomic clusters and solid targets could likewise clarify generation mechanisms in each of these systems.

Appendices

A.1: Density threshold of backscatter diagnostic

The electron density corresponding to the breakdown detection threshold is estimated by assuming Fresnel reflection from a sharp plasma density step. For a sharp boundary, the total reflection is given by $R = \left|\frac{n_1 - n_2}{n_1 + n_2}\right|^2$, where n_1 and n_2 are the indices of refraction on either side of the interface. For a plasma well below the critical density, $N_{cr} = \frac{1.1\times10^{21}}{\lambda[\mu\text{m}]^2}\text{cm}^{-3} = 7.2 \times 10^{19}\ \text{cm}^{-3}$ at $\lambda = 3.9$ μm, the plasma index of refraction is $n_2 \cong 1 - \frac{N_e}{2N_{cr}}$, such that $R = \left|\frac{N_e/2N_{cr}}{2}\right|^2 = \frac{N_e^2}{16N_{cr}^2}$ for $n_1 = 1$. The size of the plasma before saturation and late-time heating is limited by electrostatic plasma forces to a sphere of approximate radius $r{\sim}5\ \mu$m, as discussed throughout the main text, so the fractional beam energy backscattered by a single breakdown site (at threshold) is $\frac{\pi r^2}{\pi w_0^2}$, where w_0=120 μm is the beam spot size.

Assuming that the backscattered energy is spread over 2π radians, the collection efficiency is $\eta = \frac{1}{2(f/\#)^2} \sim 8 \times 10^{-5}$ for *f*/80 collection optics. The collected energy is spread out spectrally on the InSb detector, and the FWHM length of the pulse, $\tau_{pulse}{\sim}50$ ps, dictates that the energy backscattered and collected on a single pixel for incident laser energy E_0 is

$$E_{pixel} = E_0 \left(\frac{N_e^2}{16N_{cr}^2}\right)\frac{r^2}{w_0^2}\ \eta\ \frac{\tau_{pixel}}{\tau_{pulse}}\ . \qquad \text{(A. 1)}$$

To detect this backscattered energy, the energy/pixel must be above the background noise. The detector showed a noise threshold of $NT{\sim}2$ counts, with each count corresponding to $q{\sim}400$ electrons. The quantum efficiency QE of the camera in the spectral range of the pump is 90%, and the photon energy needed to generate one electron is $h\nu = 0.31$ eV. So the energy/pixel needed for detection just above the noise threshold is

$$E_{pixel,thresh} = NT \times \frac{q}{QE} h\nu. \tag{A.2}$$

Setting $E_{pixel} > E_{pixel,thresh}$ for a typical incident energy E_0=20 mJ, gives a threshold detectable plasma density of

$$N_{e,thresh} = 4\, N_{cr} \sqrt{NT \times \frac{q}{QE} \frac{h\nu}{\eta} \frac{1}{E_0} \frac{w_0^2}{r^2} \frac{\tau_{pulse}}{\tau_{pixel}}} = 6 \times 10^{17}\ cm^{-3}. \tag{A.3}$$

An important scaling from Eq. (A.3) is $N_{e,thresh} \propto f/\#$. Assuming backscatter collection with the same optic used to focus the laser, the scaling at range requires an avalanche driven closer to saturation.

A.2: Effective refractive index and absorption length under Rayleigh-Gans and Mie scattering

Here we describe the approach for finding an effective refractive index of a medium composed of many discrete breakdown sites, closely following the approach of [230]. For a scatterer located at the origin in spherical coordinates, a complex scattering function $S(\theta, \phi)$ is defined by $u_{scatt} = S(\theta, \phi)(e^{ik(r-z)}/ikr)u_0$, assuming that a scalar field description is appropriate. Here u_{scatt} is the scattered field amplitude

at (r, θ, ϕ), $u_0 e^{ikz}$ is a plane wave incident on the scatterer, and $k = 2\pi/\lambda$ is the vacuum wavenumber. For an ensemble of scatterers of uniform size, all forward scattered light (described by $S(\theta = 0, \phi) \equiv S(0)$, independent of ϕ) is coherent with the incident beam, yielding an effective refractive index

$$n_{eff} = 1 + \frac{2\pi N_{sc}}{k^3} \Im\{S(0)\}, \tag{A.4}$$

where N_{sc} is the number density of scattering particles and $\Im\{S(0)\}$ denotes the imaginary part of $S(0)$. Scattering into angles $\theta \neq 0$ is incoherent for random placement of scatterers, and contributes only to beam propagation losses, as covered below.

As discussed in the main text (Sec. 1.4.4, Chapters 4-6), diffusion during avalanche for 3.5 ps pulses dictates localized breakdown plasma radii $r_d \sim 5\mu$m for $T_e \sim 100$ eV. The average plasma density at the local breakdown site is well below the critical density, $\overline{N_e} << N_{cr} = 1.1 \times 10^{21}$ cm$^{-3}/\lambda^2$ [μm] so that the phase shift for a beam traversing the plasma site is $|\Delta\Phi| = 2kr_d|n-1| \ll 1$, where $n = \sqrt{1 - N_e/N_{cr}} \approx 1 - N_e/2N_{cr}$ is the plasma index, $|n-1| = |\Delta n| = N_e/2N_{cr} \ll 1$, and $r_d \ll \lambda/|\Delta n|$ for $\lambda \sim 10$ μm. The two latter conditions ensure that scattering falls in the Rayleigh-Gans (RG) regime, a simple extension of the familiar Rayleigh approximation. In particular, $S(0)$ is the same for RG and Rayleigh scattering, so we readily obtain

$$S(0) = \frac{ik^3(n-1)}{2\pi} V, \tag{A.5}$$

where V is the volume of the scattering site. Combining Eqs. A.4 and A.5 we find

$$n_{eff} = 1 + \frac{2\pi N_{sc}}{k^3}\,\Im\left\{\frac{ik^3(n-1)}{2\pi}V\right\} = 1 - N_{sc}V(n-1) \approx 1 - N_{sc}V\left(\frac{\overline{N_e}}{2N_{cr}}\right). \tag{A.6}$$

Since $N_{sc}V$ corresponds to an effective fill fraction, and $n - 1 \approx N_e/2N_{cr}$ for plasma well below the critical density, this result is simply the same as for a continuous plasma density $N_e = N_{sc}V\overline{N_e}$.

The total $\theta \neq 0$ Mie scattering of the incident beam results in an extinction (attenuation) length given approximately by

$$\gamma_{ext} \sim N_{sc}\pi r_d^2 |n-1|^2 \approx N_{sc}\pi r_d^2 \frac{(\overline{N_e})^2}{2N_{cr}^2} \ll 1. \tag{A.7}$$

For $r_d \approx 5\ \mu$m, λ=10 μm, and $\overline{N_e} \sim 5 \times 10^{18}$ cm^{-3} ($= N_{cr}/2$, the approximate limit of RG applicability) we get

$$\gamma_{ext} \approx N_{sc}\ [\text{cm}^{-3}] \times 10^{-7}\ \text{cm}^{-1}, \tag{A.8}$$

corresponding to an extinction length $\gamma_{ext}^{-1} \sim 10$ m for $N_{sc} \sim 10^4$ cm^{-3}. For plasma site densities well below this, the $(\overline{N_e})^2$ dependence indicates that Mie scattering losses are negligible over the length scales we consider. Indeed, the lineouts in Fig 4(b) of the main text indicate that for the self-guided pulse interacting with aerosol initiated plasmas, $\overline{N_e} \sim N_{cr}/50$ at the intensity peak of the pulse, indicating $\gamma_{ext}^{-1} \sim 3$ km for $N_{sc} \sim 2 \times 10^4$ cm^{-3}.

Once the breakdown fully singly ionizes, the scattering efficiency approaches a limiting value [230] such that for $r_d \approx 5\ \mu$m,

$$\gamma_{ext} \approx 2N_{sc}\,\pi\,r_d^2 \approx N_{sc}\ [\text{cm}^{-3}] \times 10^{-6}\ \text{cm}^{-1}, \tag{A.9}$$

giving an extinction length $\gamma_{ext}^{-1}\sim$ 1 m for $N_{sc}\sim 10^4$ cm^{-3}. This extinction length will be even shorter as plasma breakdowns expand radially with additional laser heating. We note that since this is not absorption, but rather side and small angle scattering, laser energy may appear to persist beyond γ_{ext}^{-1} as significant energy is scattered into an incoherent, forward directed "halo." In particular, the experiment [21], with which we compare our simulations, had a secondary post-pulse 25 ps after the main 3.5 ps pulse, which did not persist beyond the ~5 m plasma channel. The creation of near-critical density plasma sites from breakdown saturation of aerosols by the main pulse is consistent with (1) further heating and plasma emission from the second pulse to create a visible plasma channel, and (2) enhanced extinction of this second pulse over few meter lengths.

As the average plasma density $\overline{N_e}$ for a breakdown site approaches N_{cr}, the RG approximation breaks down and the index diverges from $n_{eff} = 1 - N_{sc}V(\overline{N_e}/2N_{cr})$. A full calculation of the Mie scattering amplitude for λ=10 μm shows n_{eff}^{Mie} agrees with n_{eff} to within 20% for a plasma of radius $r_d = 5\ \mu$m at density $\overline{N_e}$ up to $N_{cr}/2$. For $\overline{N_e} > N_{cr}/2$, the two approaches diverge and become more sensitive to the size parameter kr_d. Figure A.1 shows this comparison, with the full Mie calculation of the effective refractive index contribution (change in total effective index) of each site $\Delta n_{eff,site}^{Mie} = (n_{eff}^{Mie} - 1)/N_{sc}V$ for plasma sites of various sizes as a function of $f = \overline{N_e}/N_{cr}$, along with the refractive index contribution per site used in simulations,

$\Delta n_{eff,site}^{approx} = (n_{eff} - 1)/N_{sc}V = -(\overline{N_e}/2N_{cr})$. The actual change in local refractive index at each $\Delta n_{site} = (1 - \overline{N_e}/N_{cr})^{1/2} - 1$, is also shown.

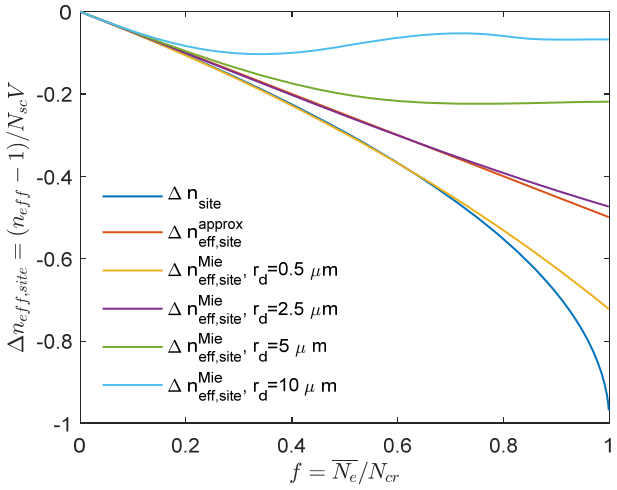

Figure A.1. Effective index contribution per site $\Delta n_{eff,site}^{Mie} = (n_{eff}^{Mie} - 1)/N_{sc}V$ for various breakdown sizes as a function of $\overline{N_e}/N_{cr}$ at a site. The effective index contribution per site used in simulations $\Delta n_{eff,site}^{approx} = (n_{eff} - 1)/N_{sc}V = -(\overline{N_e}/2N_{cr})$ as well as the actual index change at each site $\Delta n_{site} = n - 1 = (1 - \overline{N_e}/N_{cr})^{1/2} - 1$ is shown for comparison.

At saturation, the growth of the avalanche is no longer driven by exponential growth of free electrons but rather by laser heating mediated by electron-ion collisions, accompanied by an expanding ionization shock front, which increases the breakdown size. Given the difficulty of fulling calculating evolving breakdown sizes, the resultant size dependent index of refraction, and increased scattering and the increase in attenuation, we assume saturation at full ionization with no further outward plasma growth, which would tend to underestimate losses and scattering for the back half of the pulse.

Here we present further details of our propagation/avalanche simulations. Our simulations use a 2D UPPE algorithm [246] to simulate MIR laser pulse propagation through air. UPPE ('Unidirectional Pulse Propagation Equation') is a system of ordinary differential equations (ODEs) of the form

$$\frac{\partial}{\partial z}A_{k_\perp}(\omega,z) = iQ_{k_\perp}(\omega)2\pi P_{k_\perp}(\omega,z)e^{-i\left(k_z-\frac{\omega}{v_g}\right)z} \quad . \tag{A.10}$$

Here, A is related to the optical field E by $E = Ae^{ik_z z}$. The ODEs are indexed by $k_\perp$, the spectrum of radial spatial frequencies. The system is solved by a GPU implementation of the MATLAB ODE45 function. $P_{k_\perp}(\omega,z)$ is the nonlinear polarization of the medium, which in our simulation includes Kerr self-focusing, the molecular rotational response, and the plasma response. Our particular implementation of UPPE is called YAPPE ('Yet Another Pulse Propagation Effort'). The plasma response, which is the primary focus of our study, includes refraction and associated losses. The refractive response can be written as a polarization as follows:

$$P_{k_\perp}^{plasma}(\omega,z) = -\frac{4\pi e^2}{m_e\omega_c^2}\{N_{e,eff}E\}_{\omega,k_\perp} \tag{A.11}$$

for central frequency $\omega_c = 1.848\times 10^{14}\ s^{-1}$ (corresponding to $\lambda = 10.2$ μm), plasma density $N_{e,eff}$, and optical field E, and where $\{\ \}_{\omega,k_\perp}$ denotes the following sequence of operations: the bracket contents (in Eq. A.11, the product $N_{e,eff}(r,z,t)E(r,z,t)$) are first computed in spatiotemporal space, then Fourier transformed $t\rightarrow\omega$, and then Hankel transformed $r\rightarrow k_\perp$. The plasma response is taken to be non-dispersive, using only the central frequency ω_c instead of all frequency

components. Given that we simulate a 3.5ps duration pulse, the characteristic plasma dispersion length is long enough that this is a reasonable assumption. Tunneling/MPI losses are also factored into the simulation with the following imaginary polarization:

$$P_{k_\perp}^{ionloss}(\omega, z) = i\frac{n_0}{k}\left\{\frac{(\partial_t N_e^{field})\, U_I}{I}\right\}_{\omega,k_\perp} \quad \text{(A. 12)}$$

for ionization energy U_I and optical intensity I. N_e^{field} is the electron density contributed by tunneling ionization/MPI; this equation does not include electron density yield from avalanche. There are also losses from plasma heating, which are explained after the avalanche model below.

During breakdown, electron temperature is tracked as

$$\frac{dk_BT}{dt} = \frac{2}{3}\left(2U_p\nu_{en} + \nu_i U_p - \Sigma_l \nu_l \chi_l\right) - \nu_i T \ , \quad \text{(A. 13)}$$

for ponderomotive energy $U_p \cong 0.93\, I\ [\mathrm{TW/cm^2}](\lambda[\mu\mathrm{m}])^2$ eV, electron neutral collision rate ν_{en} and ionization losses of energy χ_l and excitation rate ν_l in N_2 and O_2. All of these rates are self-consistently calculated as $\nu_l = \langle\sigma_l v\rangle N_n = \langle\sigma_l v\rangle(N_{n0} - N_e)$, where N_n is the local neutral molecule density depleted from its initial value N_{n0} as the electron density N_e increases, and $\langle\sigma_i v\rangle = \int_0^\infty dv\, f(v)\sigma_i(v)v$ for electron velocity distribution $f(v) = \alpha v^2 exp(-mv^2/2k_BT)$ at temperature T, with normalization constant α. Values of relevant cross sections σ_l are drawn from [112,113] as a function of electron energy (velocity). Equation (A.12) is implemented by using the data underlying Fig. 1(a) of the main text as a 'look-up table' for the heating rate $2U_p(2\nu_{en} + \nu_i)/3$, loss rate $2(\Sigma_l \nu_l \chi_l)/3 + \nu_i T$, and ionization rate ν_i as functions of

temperature. Equation (A.12) is then solved using a first-order Forward Euler scheme with an initial temperature $T(t = 0) = U_p$.

The number density of avalanche breakdown sites N_{sc} is tracked from its initial value as

$$\frac{dN_{sc}}{dt} = \sum_i \nu_{i,MPI}(I)\, N_i \tag{A.14}$$

for tunneling/MPI ionization rate $\nu_{i,MPI}(I)$ of neutral species i (taken to be O_2 and the χ_p~6 eV contaminant [39]) of density $N_i = N_{i,0} - N_{i,sc}$, accounting for prior ionization. We assume that these electrons, released into the laser field, have an initial effective temperature U_p; for a rapid increase in the density of tunneling/MPI generated electrons, this can lead to a lower effective temperature than in the purely collisionally-driven case. Given the time-dependent temperature, the evolution of the effective electron density $N_{e,eff} = N_{sc}V\overline{N_e}$, which we track as a single quantity, is given by

$$\frac{dN_{e,eff}}{dt} = N_{sc}\nu_i V\overline{N_e} + V\overline{N_e}\frac{dN_{sc}}{dt} \;\rightarrow\; N_{sc}\nu_i V\overline{N_e} + \frac{dN_{sc}}{dt}$$

$$= \nu_i N_{e,eff} + \frac{dN_{sc}}{dt} \tag{A.15}$$

where the quantities not defined in this supplement are defined in the main text. To model what is really a spatially inhomogeneous process, we must apply separate physical considerations to each term of Eq. (A.15). The first term, $N_{sc}\nu_i V\overline{N_e}$, tracks the rate of avalanche ionization growth at existing breakdown sites. In the second term, putting $V\overline{N_e} \rightarrow 1$, so that $V\overline{N_e}\, dN_{sc}/dt \rightarrow dN_{sc}/dt$, enables tracking only the contribution of new avalanche seed sites in neutral gas.

The effective transient refractive index is then given by

$$n_{eff} = 1 - \frac{N_{e,eff}}{2N_{cr}} = 1 - \frac{N_{sc}V\overline{N_e}}{2N_{cr}} \quad . \tag{A.16}$$

We note that saturation and depletion can occur either through volume average full single ionization of the gas, $N_{no} = N_{e,eff} = N_{sc}V\overline{N_e}$, or through full single ionization at a single avalanche site, $N_{no} = \overline{N_e}$. Thus, we take the transient residual neutral density during ionization to be

$$N_n = \min(N_{no} - N_{e,eff}, N_{no} - \overline{N_e}), \tag{A.17}$$

for $\overline{N_e} = N_{e,eff}/(N_{sc}(4\pi r_d^3/3))$. Avalanches seeded by aerosols were assumed to start with one electron per aerosol, either provided by existing static charge or by ionization early in the pulse. As discussed above, electron number growth at each aerosol follows $n_e(t) = n_{e,0}e^{\nu_{is}t}$ for $\nu_{is} = 40 \times I[\mathrm{TW/cm^2}]$ $\mathrm{ps^{-1}}$, which continues until the ~10^8 atoms in a ~0.2 μm diameter particle are singly ionized. To make our simulation tractable while still preserving the physics relevant to propagation, we ignore the plasma dynamics of aerosol explosion into the surrounding air: $n_e(t)$ is combined with avalanche in the surrounding air computed with Eqs. (A.13) – (A.15), forming $\overline{N_e} \rightarrow \overline{N_e} + n_e(4\pi r_d^3/3)^{-1}$. Since aerosols avalanche (and saturate) so much more quickly than breakdowns seeded by single electron seeds, they can be considered the dominant source of avalanche when they are present.

Absorption of laser energy density due to laser heating is included in the YAPPE propagation simulations as a laser energy loss rate per unit volume

$$W_{abs} = \frac{2}{3}\left(2U_p\nu_{en} + \nu_i U_p\right)N_{e,eff} \ . \tag{A.18}$$

This energy loss rate is also modelled as a complex polarization:

$$P_{k_\perp}^{abs}(\omega, z) = \ i\frac{n_0}{k}\left\{\frac{W_{abs}}{I}E\right\}_{\omega,k_\perp} \tag{A.19}$$

For plasma generation below saturation, we neglect scattering losses, as discussed in A.2 above.

Bibliography

1. P. A. Franken, A. E. Hill, C. W. Peters, and G. Weinreich, “Generation of Optical Harmonics,” Phys. Rev. Lett. **7**, 118-119 (1961).

2. A. Couairon and A. Mysyrowicz, “Femtosecond filamentation in transparent media,” Phys. Rep. **441**, 47-189 (2007).

3. L. Bergé, S. Skupin, R. Nuter, J. Kasparian, and J.-P. Wolf, “Ultrashort filaments of light in weakly ionized, optically transparent media,” Rep. Prog. Phys. **70**, 1633 (2007).

4. M. Kress, T. Löffler, S. Eden, M. Thomson, and H. G. Rokos, “Terahertz-pulse generation by photoionization of air with laser pulses composed of both fundamental and second-harmonic waves,” Opt. Lett. **29**, 1120–1122 (2004).

5. K. Y. Kim, J. H. Glownia, A. J. Taylor, and G. Rodriguez, “Terahertz emission from ultrafast ionizing air in symmetry-broken laser fields,” Opt. Express **15**, 4577–4584 (2007).

6. K. Y. Kim, A. J. Taylor, J. H. Glownia, and G. Rodriguez, "Coherent control of terahertz supercontinuum generation in ultrafast laser–gas interactions," Nat. Photonics **2**, 605 (2008).

7. S. Tzortzakis, G. Méchain, G. Patalano, Y.-B. André, B. Prade, M. Franco, A. Mysyrowicz, J.-M. Munier, M. Gheudin, G. Beaudin, and P. Encrenaz, “Coherent subterahertz radiation from femtosecond infrared filaments in air,” Opt. Lett. **27**, 1944-1946 (2002).

8. P. B. Corkum, “Plasma perspective on strong-field multiphoton ionization,” Phys. Rev. Lett. **71**, 1994–1997 (1993).

9. O. L. Landen, E. M. Campbell, and M. D. Perry, “X-ray characterization of picosecond laser plasmas,” Opt. Commun. **63**, 253 (1987)

10. D. G. Stearns, O. L. Landen, E. M. Campbell, and J. H. Scofield, “Generation of ultrashort x-ray pulses,” Phys. Rev. A **37**, 1684 (1988)

11. F. Albert, B. B. Pollock, J. L. Shaw, K. A. Marsh, J. E. Ralph, Y.-H. Chen, D. Alessi, A. Pak, C. E. Clayton, S. H. Glenzer, and C. Joshi, "Angular Dependence of Betatron X-Ray Spectra from a Laser-Wakefield Accelerator," Phys. Rev. Lett. **111**, 235004 (2013)

12. S. Corde, K. Ta Phuoc, G. Lambert, R. Fitour, V. Malka, A. Rousse, A. Beck, and E. Lefebvre, “Femtosecond x rays from laser-plasma accelerators,” Rev. Mod. Phys. **85**, 1-48 (2013).

13. G. W. Collins, L. B. Da Silva, P. Celliers, D. M. Gold, M. E. Foord, R. J. Wallace, A. Ng, S. V. Weber, K. S. Budil, R. Cauble, "Measurements of the Equation of State of Deuterium at the Fluid Insulator-Metal Transition," Science **281,** 1178-1181 (1998).

14. M. A. Purvis, V. N. Shlyaptsev, R. Hollinger, C. Bargsten, A. Pukhov, A. Prieto, Y. Wang, B. M. Luther, L. Yin, S. Wang, and J. J. Rocca, "Relativistic plasma nanophotonics for ultrahigh energy density physics," Nat. Phot. **7**, 796-800 (2013).

15. B. A. Remington, R. P. Drake, and D. D. Ryutov, "Experimental astrophysics with high power lasers and Z pinches," Rev. Mod. Phys. **78**, 755-808 (2006)

16. T. Tajima and J. M. Dawson, "Laser Electron Accelerator," Phys. Rev. Lett. **43**, 267-270 (1979).

17. E. Esarey, C. B. Schroeder, and W. P. Leemans, "Physics of laser-driven plasma-based electron accelerators," Rev. Mod. Phys. **81**, 1229-1285 (2009).

18. E. Esarey, P. Sprangle, J. Krall, and A. Ting, "Overview of plasma-based accelerator concepts," IEEE. Trans. Plasma Phys. **24**, 252-288 (1996); P. Sprangle, E. Esarey, A. Ting, and G. Joyce, "Laser wakefield acceleration and relativistic optical guiding," Appl. Phys. Lett. **53** 2146-2148 (1988).

19. A. Macchi, M. Borghesi, and M. Passoni, "Ion acceleration by superintense laser-plasma interaction," Rev. Mod. Phys. **85**, 751-793 (2013).

20. H. Chen, S. C. Wilks, J. D. Bonlie, E. P. Liang, J. Myatt, D. F. Price, D. D. Meyerhofer, and P. Beiersdorfer, "Relativistic Positron Creation Using Ultraintense Short Pulse Lasers," Phys. Rev. Lett. **102**, 105001 (2009).

21. S. Tochitsky, E. Welch, M. Polyanskiy, I. Pogorelsky, P. Panagiotopoulos, M. Kolesik, E. M. Wright, S. W. Koch, J. V. Moloney, J. Pigeon, and C. Joshi, "Megafilament in air formed by self-guided terawatt long-wavelength infrared laser," Nat. Phot. **13**, 41-46 (2019).

22. V. Shumakova, S. Ališauskas, P. Malevich, C. Gollner, A. Baltuška, D. Kartashov, A. M. Zheltikov, A. V. Mitrofanov, A. A. Voronin, D. A. Sidorov-Biryukov, and A. Pugžlys, "Filamentation of mid-IR pulses in ambient air in the vicinity of molecular resonances," Opt. Lett. **43** 2185-2188 (2019).

23. V. Shumakova, S. Ališauskas, P. Malevich, A. A. Voronin, A. V. Mitrofanov, D. A. Sidorov-Biryukov, A. M. Zheltikov, D. Kartashov, A. Baltuška, and A. Pugžlys, "Chirp-controlled filamentation and formation of light bullets in the mid-IR," Opt. Lett. **44**, 2173-2176 (2019).

24. V. Shumakova, P. Malevich, S. Ališauskas, A. Voronin, A. M. Zheltikov, D. Faccio, D. Kartashov, A. Baltuška, and A. Pugžlys, "Multi-millijoule few-cycle

mid-infrared pulses through nonlinear self-compression in bulk," Nat. Commun. **7**, 12877 (2016).

25. A. V. Mitrofanov, A. A. Voronin, M. V. Rozhko, D. A. Sidorov-Biryukov, A. B. Fedotov, A. Pugžlys, V. Shumakova, S. Ališauskas, A. Baltuška, and A. M. Zheltikov, "Self-compression of high-peak-power mid-infrared pulses in anomalously dispersive air," Optica **4**, 1405-1408 (2017).

26. D. Jang, R. M. Schwartz, D. Woodbury, J. Griff-McMahon, A. H. Younis, H. M. Milchberg, and K. Y. Kim, "Efficient terahertz and Brunel harmonic generation from air plasma via mid-infrared coherent control," Optica **6**, 1338-1341 (2019).

27. A. D. Koulouklidis, C. Gollner, V. Shumakova, V. Y. Fedorov, A. Pugžlys, A. Baltuška, and S. Tzortzakis, "Observation of extremely efficient terahertz generation from mid-infrared two-color laser filaments," Nat. Commun. **11**, 292 (2020).

28. A. Englesbe, R. Schwartz, A. Korolov, D. Jang, D. Woodbury, K.-Y. Kim, H. Milchberg, R. Reid, A. Lucero, H. Pohle, S. Kalmykov, K. Krushelnick, A. Schmitt-Sody, and J. Elle, "Microwave Radiation from Single and Two Color Mid-Infrared Laser Produced Plasmas in Air," in Conference on Lasers and Electro-Optics, paper FTh1M.3, San Jose, CA (2019).

29. A. Englesbe, J. Elle, R. Schwartz, A. Korolov, D. Woodbury, D. Jang, K.-Y. Kim, H. Milchberg, R. Reid, A. Lucero, T. Garrett, H. Pohle, R. Phillips, S. Kalmykov, K. Krushelnick, and A. Schmitt-Sody, "Broadband microwave radiation from near and mid-infrared laser produced plasmas in air," in preparation.

30. T. Popmintchev, M.-C. Chen, D. Popmintchev, P. Arpin, S. Brown, S. Ališauskas, G. Andriukaitis, T. Balčiunas, O. D. Mücke, A. Pugzlys, A. Baltuška, B. Shim, S. E. Schrauth, A. Gaeta, C. Hernández-García, L. Plaja, A. Becker, A. Jaron-Becker, M. M. Murnane, and H. C. Kapteyn, "Bright Coherent Ultrahigh Harmonics in the keV X-ray Regime from Mid-Infrared Femtosecond Lasers," Science **336**, 1287-1291 (2012).

31. A. V. Mitrofanov, A. A. Voronin, S. I. Mitryukovskiy, D. A. Sidorov-Biryukov, A. Pugžlys, G. Andriukaitis, T. Flöry, E. A. Stepanov, A. B. Fedotov, A. Baltuška, and A. M. Zheltikov, "Mid-infrared-to-mid-ultraviolet supercontinuum enhanced by third-to-fifteenth odd harmonics," Opt. Lett. **40**, 2068-2071 (2015).

32. N. Beier, T. Nguyen, J. Lin, J. Nees, K. Krushelnick, F. Dollar, "Relativistic short-pulse high harmonic generation at 1.3 and 2.1 μm wavelengths," New J. Phys. **21**, 043052 (2019).

33. D. Haberberger, S. Tochitsky, F. Fiuza, C. Gong, R. A. Fonseca, L. O. Silva, W. B. Mori & C. Joshi, “Collisionless shocks in laser-produced plasma generate monoenergetic high-energy proton beams,” Nat. Phys. **8**, 95-99 (2012).

34. J. Weisshaupt, V. Juvé, M. Holtz, S. Ku, M. Woerner, T. Elsaesser, S. Ališauskas, A. Pugžlys, and A. Baltuška, “High-brightness table-top hard X-ray source driven by sub-100-femtosecond mid-infrared pulses,” Nat. Photonics **8**, 927-930 (2014).

35. Z. Samsonova, S. Höfer, V. Kaymak, S. Ališauskas, V. Shumakova, A. Pugžlys, A. Baltuška, T. Siefke, S. Kroker, A. Pukhov, O. Rosmej, I. Uschmann, C. Spielmann, and D. Kartashov, “Relativistic Interaction of Long-Wavelength Ultrashort Laser Pulses with Nanowires,” Phys. Rev. X **9**, 021029 (2019).

36. D. Woodbury, L. Feder, V. Shumakova, C. Gollner, R. Schwartz, F. Salehi, B. Miao, A. Korolov, A. Pugzlys, A. Baltuska, and H. M. Milchberg, "Laser wakefield acceleration with mid-IR laser pulses," Optics Letters **43**, 1131 (2018).

37. R. M. Schwartz, D. Woodbury, J. Isaacs, P. Sprangle, and H. M. Milchberg. "Remote detection of radioactive material using mid-IR laser-driven electron avalanche," Sci. Adv. **5**, eaav6804 (2019).

38. D. Woodbury, R. M. Schwartz, and H. M. Milchberg, "Measurement of ultralow radiation-induced charge densities using picosecond mid-IR laser-induced breakdown," Optica **6**, 811 (2019).

39. D. Woodbury, R. M. Schwartz, E. Rockafellow, J. K. Wahlstrand, and H. M. Milchberg. "Absolute measurement of laser ionization yield in atmospheric pressure range gases over 14 decades," Phys. Rev. Lett. **124**, 013201 (2020).

40. D. Woodbury, A. Goffin, R. M. Schwartz, J. Isaacs, and H. M. Milchberg. "Self-guiding of long-wave infrared laser pulses mediated by avalanche ionization," submitted for publication. https://arxiv.org/abs/2003.11405

41. G. Fibich and A. L. Gaeta, "Critical power for self-focusing in bulk media and in hollow waveguides," Opt. Lett. **25**, 335-337 (2000).

42. A. Braun, G. Korn, X. Liu, D. Du, J. Squier, and G. Mourou, "Self-channeling of high-peak-power femtosecond laser pulses in air," Opt. Lett. **20**, 73 (1995).

43. D. Strickland and P. B. Corkum, "Resistance of short pulses to self-focusing" J. Opt. Soc. Am. B **11**, 492-497 (1994).

44. Y. E. Geints and A. A. Zemlyanov, “Single and multiple filamentation of multi-terawatt CO2-laser pulses in air: numerical simulations,” J. Opt. Soc. Am. B **31**, 788-797 (2014).

45. P. Panagiotopoulos, P. Whalen, M. Kolesik, and J. V. Moloney, “Super high power mid-infrared femtosecond light bullet,” Nat. Phot. **9,** 543-548 (2015).

46. P. Panagiotopoulos, P. Whalen, M. Kolesik, and J. V. Moloney, “Carrier field shock formation of long-wavelength femtosecond pulses in single-crystal diamond and air,” J. Opt. Soc. Am. B **32,** 1718-1730 (2015).

47. P. Panagiotopoulos, K. Schuh, M. Kolesik, and J. V. Moloney, “Simulations of 10 μm filaments in a realistically modeled atmosphere,” J. Opt. Soc. Am. B **33,** 2154-2161 (2016).

48. S. Eliezer, *The Interaction of High Power Lasers with Plasmas,* (CRC Press, 2002).

49. L.V. Keldysh, “Ionization in the field of a strong electromagnetic wave,” Sov. Phys. JETP **20**, 1307 (1965).

50. S. V. Popruzhenko, V. D. Mur, V. S. Popov, and D. Bauer, “Strong field ionization rate for arbitrary laser frequencies,” Phys. Rev. Lett. **101**, 193003 (2008).

51. K. Schuh, J. Hader, J. V. Moloney, and S. W. Koch, "Influence of many-body interactions during the ionization of gases by short intense optical pulses," Phys. Rev. E **89,** 033103 (2014).

52. K. Schuh, J. Hader, J. V. Moloney, and S. W. Koch, "Influence of optical and interaction-induced dephasing effects on the short-pulse ionization of atomic gases," J. Opt. Soc. Am. B **32,** 1442 (2015).

53. K. Schuh, J. V. Moloney, and S. W. Koch, “Interaction-induced nonlinear refractive-index reduction of gases in the midinfrared regime,” Phys. Rev. E **93,** 013208 (2016).

54. K. Schuh, M. Koleski, J. V. Moloney, and S. W. Koch, “Self-Channeling of High-Power Long-Wave Infrared Pulses in Atomic Gases,” Phys. Rev. Lett. **118,** 063901 (2017).

55. W. L. Kruer, The Physics of Laser Plasma Interactions (Addison-Wesley, Redwood City, Calif., 1988).

56. H. C. Kapteyn, M. M. Murnane, A. Szoke, and R. W. Falcone, "Prepulse energy suppression for high-energy ultrashort pulses using self-induced plasma shuttering," Opt. Lett. **16**, 490-492 (1991).

57. P. Sprangle, C.-M. Tang, and E. Esarey, “Relativistic Self-Focusing of Short-Pulse Radiation Beams in Plasmas,” IEEE Trans. Plasma Sci. **15**, 145-153 (1987).

58. G. Z. Sun, E. Ott, Y. C. Lee, and P. Guzdar, “Self-focusing of short intense pulses in plasmas,” Phys. Fluids **30**, 526 (1987).

59. K. B. Fournier, C. Constantin, J. Poco, M. C. Miller, C. A. Back, L. J. Suter, J. Satcher, J. Davis, and J. Grun, "Efficient Multi-keV X-Ray Sources from Ti-Doped Aerogel Targets," Phys. Rev. Lett. **92**, 165005 (2004).

60. F. Sylla, A. Flacco, S. Kahaly, M. Veltcheva, A. Lifschitz, V. Malka, E. d'Humières, I. Andriyash, and V. Tikhonchuk, “Short intense laser pulse collapse in near-critical plasma,” Phys. Rev. Lett. **110**, 085001 (2013).

61. A. J. Goers, G. A. Hine, L. Feder, B. Miao, F. Salehi, J. K. Wahlstrand, and H. M. Milchberg, "Multi-MeV Electron Acceleration by Subterawatt Laser Pulses," Phys. Rev. Lett. **115**, 194802 (2015).

62. F. Salehi, A. J. Goers, L. Feder, B. Miao, D. Woodbury, and H. M. Milchberg, "Characterization of a 100 micrometer-scale cryogenically cooled gas jet for near-critical density laser-plasma experiments," Rev. Sci. Instr. **90**, 103001 (2019).

63. F. Salehi, A. J. Goers, G. A. Hine, L. Feder, D. Kuk, B. Miao, D. Woodbury, K. Y. Kim, and H. M. Milchberg, "MeV electron acceleration at 1 kHz with < 10mJ laser pulses," Optics Letters **42**, 215 (2017).

64. M. Borghesi, A. J. MacKinnon, L. Barringer, R. Gaillard, L. A. Gizzi, C. Meyer, and O. Willi, "Relativistic Channeling of a Picosecond Laser Pulse in a Near-Critical Preformed Plasma," Phys. Rev. Lett. **78**, 879-882 (1997).

65. J. D. Lawson, “Lasers and Accelerators,” IEEE Trans. Nucl. Sci. **26**, 4217-4219 (1979).

66. P. Mora and T. M. Antonsen, "Electron cavitation and acceleration in the wake of an ultraintense, self-focused laser pulse," Phys. Rev. E **53**, R2068-R2071 (1996)

67. W. Lu, C. Huang, M. Zhou, W. B. Mori, and T. Katsouleas, "Nonlinear Theory for Relativistic Plasma Wakefields in the Blowout Regime," Phys. Rev. Lett. **96**, 165002 (2006).

68. W. Lu, M. Tzoufras, C. Joshi, F. S. Tsung, W. B. Mori, J. Vieira, R. A. Fonseca, and L. O. Silva, “Generating multi-GeV electron bunches using single stage laser wakefield acceleration in a 3D nonlinear regime,” Phys. Rev. ST Accel. Beams **10**, 061301 (2007)

69. N. E. Andreev and V. I. Kirsanov, "Stimulated processes and self-modulation of a short intense laser pulse in the laser wake-field accelerator," Phys. Plasmas **2**, 2573-2582 (1995).

70. P. Sprangle, E. Esarey, J. Krall, and G. Joyce,"Propagation and guiding of intense laser pulses in plasmas," Phys. Rev. Lett. **69**, 2200-2203 (1992).

71. W. B. Mori, C. D. Decker, D. E. Hinkel, and T. Katsouleas, "Raman forward scattering of short-pulse high-intensity lasers," Phys. Rev. Lett. **72**, 1482-1485 (1994).

72. C. A. Coverdale, C. B. Darrow, C. D. Decker, W. B. Mori, K-C. Tzeng, K. A. Marsh, C. E. Clayton, and C. Joshi, "Propagation of Intense Subpicosecond Laser Pulses through Underdense Plasmas," Phys. Rev. Lett. **74**, 4659-4662 (1995).

73. A. Modena, Z. Najmudin, A. E. Dangor, C. E. Clayton, K. A. Marsh, C. Joshi, V. Malka, C. B. Darrow, C. Danson, D. Neely, and F. N. Walsh,"Electron acceleration from the breaking of relativistic plasma waves, " Nature **377**, 606-608 (1995).

74. A. Ting, C. I. Moore, K. Krushelnick, C. Manka, E. Esarey, P. Sprangle, R. Hubbard, H. R. Burris, R. Fischer, and M. Baine, "Plasma wakefield generation and electron acceleration in a self-modulated laser wakefield accelerator experiment," Phys. Plasmas **4**, 1889-1899 (1997).

75. D. Gordon, K. C. Tzeng, C. E. Clayton, A. E. Dangor, V. Malka, K. A. Marsh, A. Modena, W. B. Mori, P. Muggli, Z. Najmudin, D. Neely, C. Danson, and C. Joshi, "Observation of Electron Energies Beyond the Linear Dephasing Limit from a Laser-Excited Relativistic Plasma Wave," Phys. Rev. Lett. **80**, 2133-2136 (1998).

76. S. Bulanov, N. Naumova, F. Pegoraro, and J. Sakai, "Particle injection into the wave acceleration phase due to nonlinear wake wave breaking," Phys. Rev. E **58**, R5257-R5260 (1998).

77. B. Miao, L. Feder, J. Elle, A. J. Goers, D. Woodbury, F. Salehi, J. K. Wahlstrand, and H. M. Milchberg. "Coherent ultra-broadband laser-assisted injection radiation from a laser plasma accelerator," Phys. Rev. E **98**, 043206 (2018).

78. H. Suk, N. Barov, J. B. Rosenzweig, and E. Esarey, "Plasma Electron Trapping and Acceleration in a Plasma Wake Field Using a Density Transition," Phys. Rev. Lett. **86**, 1011-1014 (2001).

79. A. J. Gonsalves, K. Nakamura, C. Lin, D. Panasenko, S. Shiraishi, T. Sokollik, C. Benedetti, C. B. Schroeder, C. G. R. Geddes, J. van Tilborg, J.

Osterhoff, E. Esarey, C. Toth and W. P. Leemans, "Tunable laser plasma accelerator based on longitudinal density tailoring," Nat. Phys. **7**, 862–866 (2011).

80. E. Oz, S. Deng, T. Katsouleas, P. Muggli, C. D. Barnes, I. Blumenfeld, F. J. Decker, P. Emma, M. J. Hogan, R. Ischebeck, R. H. Iverson, N. Kirby, P. Krejcik, C. O'Connell, R. H. Siemann, D. Walz, D. Auerbach, C. E. Clayton, C. Huang, D. K. Johnson, C. Joshi, W. Lu, K. A. Marsh, W. B. Mori, and M. Zhou, "Ionization-Induced Electron Trapping in Ultrarelativistic Plasma Wakes," Phys. Rev. Lett. **98**, 084801(2007).

81. N. Bourgeois, J. Cowley, and S. M. Hooker, "Two-Pulse Ionization Injection into Quasilinear Laser Wakefields," Phys. Rev. Lett. **111**, 155004 (2013).

82. X. L. Xu, Y. P. Wu, C. J. Zhang, F. Li, Y. Wan, J. F. Hua, C.-H. Pai, W. Lu, P. Yu, C. Joshi, and W. B. Mori, "Low emittance electron beam generation from a laser wakefield accelerator using two laser pulses with different wavelengths," Phys. Rev. ST Accel. Beams **17**, 061301 (2014).

83. A. J. Goers, S. J. Yoon, J. A. Elle, G. A. Hine, and H. M. Milchberg, "Laser wakefield acceleration of electrons with ionization injection in a pure N5+ plasma waveguide," Appl. Phys. Lett. **104**, 214105 (2014).

84. W. H. Urbanus, W. van Dijk, S. B. van der Geer, G. J. H. Brussaard, and M. J. van der Wiel, "Front-to-end simulations of the design of a laser wakefield accelerator with external injection," J. Appl. Phys. **99**, 114501 (2006).

85. T. Mehrling, J. Grebenyuk, F. S. Tsung, K. Floettmann, and J. Osterhoff, "Transverse emittance growth in staged laser-wakefield acceleration," Phys. Rev. ST Accel. Beams **15**, 111303 (2012).

86. S. Steinke, J. van Tilborg, C. Benedetti, C. G. R. Geddes, C. B. Schroeder, J. Daniels, K. K. Swanson, A. J. Gonsalves, K. Nakamura, N. H. Matlis, B. H. Shaw, E. Esarey, and W. P. Leemans, "Multistage coupling of independent laser-plasma accelerators," Nature **530**, 190-193 (2016).

87. E. Esarey, R. F. Hubbard, W. P. Leemans, A. Ting, and P. Sprangle, "Electron Injection into Plasma Wakefields by Colliding Laser Pulses," Phys. Rev. Lett. **79**, 2682-2685 (1997).

88. J. Faure, C. Rechatin, A. Norlin, A. Lifschitz, Y. Glinec and V. Malka, "Controlled injection and acceleration of electrons in plasma wakefields by colliding laser pulses," Nature **444**, 737–739 (2006).

89. J. Faure, Y. Glinec, A. Pukhov, S. Kiselev, S. Gordienko, E. Lefebvre, J.-P. Rousseau, F. Burgy, and V. Malka, "A laser–plasma accelerator producing monoenergetic electron beams," Nature **431**, 541-544 (2004).

90. C. G. R. Geddes, C. Toth, J. van Tilborg, E. Esarey, C. B. Schroeder, D. Bruhwiler, C. Nieter, J. Cary, and W. P. Leemans, "High-quality electron beams from a laser wakefield accelerator using plasma-channel guiding," Nature **431**, 538-541 (2004).

91. S. P. D. Mangles, C. D. Murphy, Z. Najmudin, A. G. R. Thomas, J. L. Collier, A. E. Dangor, E. J. Divall, P. S. Foster, J. G. Gallacher, C. J. Hooker, D. A. Jaroszynski, A. J. Langley, W. B. Mori, P. A. Norreys, F. S. Tsung, R. Viskup, B. R. Walton, and K. Krushelnick, "Monoenergetic beams of relativistic electrons from intense laser–plasma interactions," Nature **431**, 535-538 (2004).

92. L.-L. Yu, E. Esarey, C. B. Schroeder, J.-L. Vay, C. Benedetti, C. G. R. Geddes, M. Chen, and W. P. Leemans, "Two-Color Laser-Ionization Injection," Phys. Rev. Lett. **112**, 125001 (2014).

93. G. Hine, "Compact Laser Driven Electron and Proton Acceleration with Low Energy Lasers," PhD Dissertation, University of Maryland (2017).

94. Y. Ma, D. Seipt, A. E. Hussein, S. Hakimi, N. F. Beier, S. B. Hansen, J. Hinojosa, A. Maksimchuk, J. Nees, K. Krushelnick, A. G. R. Thomas, and F. Dollar, "Polarization-Dependent Self-Injection by Above Threshold Ionization Heating in a Laser Wakefield Accelerator," Phys. Rev. Lett. **124**, 114801 (2020).

95. T. P. Wangler, *RF Linear Accelerators, 2nd ed* (Wiley-VHC, 2008).

96. A. Grudiev, S. Calatroni, and W. Wuensch, "New local field quantity describing the high gradient limit of accelerating structures," Phys. Rev. ST Accel. Beams **12**, 102001 (2009).

97. P. D. Maker, R. K. Terhune, and C. M. Savage, in Proc. 3rd Int. Conf. on Quantum Electronics, ed. by P. Grivet and N. Bloembergen (Columbia University Press, 1963) p. 1559.

98. R.G. Meyerand and A. F. Haught, "Gas Breakdown at Optical Frequencies," Phys. Rev. Lett. **2**, 401-403 (1963).

99. Y.B. Zeldovich, Y.P. Raizer, "Cascade Ionization of a gas by a light pulse," JETP **20**, 772-89 (1965). [ZhETF **47**, 1150 (1964)].

100. P. Agostini, G. Barjot, J. Bonnal, G. Mainfray, C. Manus, and J. Morellec, "Multiphoton ionization of hydrogen and rare gases," IEEE J. Quant. Elec. **4**, 667-669 (1968).

101. A. S. Voronov and N. B. Delone, " Many-photon Ionization of the Xenon Atom by Ruby Laser Radiation," JETP **23**, 54-58 (1965).

102. A. M. Perelomov, V. S. Popov, and M. V. Terent'ev, "Ionization of atoms in an alternating electric field," Sov. Phys. JETP **23**, 924 (1966).

103. S. L. Chin, "Direct experimental evidence of multiphoton ionization of impurities as the initiation process of laser-induced gas breakdown," Can. J. Phys. **48,** 1314 (1970).

104. Y.P. Raizer, "Breakdown and heating of gases under the influence of a laser beam," Usp. Fiz. Nauk **87**, 29-64 (1965).

105. V. Phelps, in *Physics of Quantum Electronics*, ed. by P. L. Kelley et al. (McGraw-Hill, New York, 1966), p. 538.

106. N. Kroll and K. M. Watson, "Theoretical study of ionization of air by intense laser pulses," Phys. Rev. A **5**, 1883-1905 (1972).

107. C. G. Morgan, "Laser-induced breakdown of gases," Rep. Prog. Phys. **38,** 621-665 (1975).

108. Yu. P. Raizer, *Laser Induced Discharge Phenomena* (Consultants Bureau, 1977)

109. G. Bekefi, *Principles of Laser Plasmas* (Wiley, 1976).

110. A. D. MacDonald, *Microwave Breakdown in Gases* (Wiley,1966).

111. E. Yablonovitch, "Similarity principles for laser-induced breakdown in gases," Appl. Phys. Lett **23**, 121-122 (1973).

112. Y. Itikawa, "Cross Sections for Electron Collisions with Nitrogen Molecules," J. Phys. Chem. Ref. Data **35**, 31 (2006).

113. Y. Itikawa, "Cross Sections for Electron Collisions with Oxygen Molecules," J. Phys. Chem. Ref. Data **38**, 1 (2009).

114. A. W. Ali, "On Laser Air Breakdown, Threshold Power and Laser Generated Channel Length," NRL Memorandum Report No. 5187 (1983).

115. B. K. Deka, P. E. Dyer, D. J. James, S. A. Ramsden, "Gas breakdown threshold measurements using a pulsed HF/DF laser," Opt. Commun. **19**, 292-296 (1976).

116. A. F. Haught, R. G. Meyerand, and D. C. Smith, in *Physics of Quantum Electronics*, ed. by P. L. Kelley et al. (McGraw-Hill, 1966), p. 509.

117. G. Tomlinson, E. K. Damon, and H. T. Buscher, in *Physics of Quantum Electronics*, ed. by P. L. Kelley et al. (McGraw-Hill, 1966), p. 520.

118. D. E. Lencioni, "The effect of dust on 10.6-μm laser-induced air breakdown," Appl. Phys. Lett. **23,** 12-14 (1973).

119. D. E. Lencioni, "Laser-induced air breakdown for 1.06-μm radiation," Appl. Phys. Lett. **25,** 15-17 (1974).

120. D. C. Smith, "Gas breakdown initiated by laser radiation interaction with aerosols and solid surfaces,"
J. Appl. Phys. **48,** 2217-2225 (1977).

121. H. T. Buscher, R. G. Tomlinson, and E. K. Damon, "Frequency Dependence of Optically Induced Gas Breakdown," Phys. Rev. Lett. **15**, 847-849 (1965).

122. A.J. Alcock, K. Kato, and M.C. Richardson, "New features of laser-induced gas breakdown in the ultraviolet," Opt. Commun. **6,** 342-344 (1972).

123. M. J. Soileau, "Air breakdown by pulsed-laser radiation in the 2.7- and 3.8-mm region," Appl. Phys. Lett. **35**, 309-211 (1979).

124. D. Stricker and J. G. Parker, "Experimental investigation of electrical breakdown in nitrogen and oxygen induced by focused laser radiation at 1.064 mm," J. Appl. Phys. **53**, 851-855 (1982).

125. G. M. Weyl and D. Rosen, "Laser-induced breakdown in argon at 0.35 mm: Theory and experiments," Phys. Rev. A **31**, 2300-2313.

126. J. S. Hummelt and J. E. Scharer, "Excitational energy transfer enhancing ionization and spatial-temporal evolution of air breakdown with UV laser radiation" J. Appl. Phys. **108**, 093305 (2010).

127. V. D. Zvorykin, A. O. Levchenko and N. N. Ustinovskii, “Control of extended high-voltage electric discharges in atmospheric air by UV KrF-laser radiation,” Quantum Electron. **41**, 227-233 (2011).

128. J. Isaacs, C. Miao, and P. Sprangle, “Remote monostatic detection of radioactive material by laser-induced breakdown,” Phys. Plasmas **23,** 033507 (2016)

129. J. Isaacs, D. Woodbury, and P. Sprangle, “Remote detection of radioactive material using optically induced air breakdown ionization,” Proc. SPIE, **11010,** 11010E (2019).

130. J. Isaacs, “The physics of high-intensity laser-matter interactions and applications,” PhD Dissertation, University of Maryland (2019).

131. D. Woodbury, J. Wahlstrand, A. Goers, L. Feder, B. Miao, G. Hine, F. Salehi, and H. Milchberg., "Single-shot measurements of laser-induced avalanche breakdown demonstrating spatial and temporal control by an external source," Presentation CP10.00154. American Physical Society Division of Plasma Physics Meeting, Oct. 2016.

132. F. F. Chen, *Introduction to Plasma Physics and Controlled Fusion* (Plenum Press, 1984).

133. Y. B. Zel'dovich and Y. P. Raizer, *Physics of Shock Waves and High-Temperature Hydrodynamic Phenomena* (Academic Press, 1967).

134. D. Kim, D. Yu, A. Sawant, M. S. Choe, I. Lee, S. G. Kim, and E. Choi, "Remote detection of radioactive material using high-power pulsed electromagnetic radiation," Nat. Commun**. 8**, 15394 (2017).

135. D. Strickland and G. Mourou, "Compression of amplified chirped optical pulses," Opt. Commun. **55**, 447-449 (1985).

136. J. H. Sung, H. W. Lee, J. Y. Yoo, J. W. Yoon, C. W. Lee, J. M. Yang, Y. J. Son, Y. H. Jang, S. K. Lee, and C. H. Nam, "4.2 PW, 20 fs Ti:sapphire laser at 0.1 Hz," Opt. Lett. **42**, 2058-2061 (2017).

137. Y. Chu, X. Liang, L. Yu, Y. Xu, L. Xu, L. Ma, X. Lu, Y. Liu, Y. Leng, R. Li, and Z. Xu, "High-contrast 2.0 Petawatt Ti:sapphire laser system," Opt. Ex. **21**, 29231-29239 (2013).

138. S. Vasilyev, I. Moskalev, M. Mirov, S. Mirov, and V. Gapontsev, "Multi-Watt mid-IR femtosecond polycrystalline Cr^{2+}:ZnS and Cr^{2+}:ZnSe laser amplifiers with the spectrum spanning 2.0–2.6 μm," Opt. Ex. **24**, 1616-1623 (2016).

139. S. Vasilyev, I. Moskalev, V. Smolski, J. Peppers, M. Mirov, V. Fedorov, D. Martyshkin, S. Mirov, and V. Gapontsev, "Octave-spanning Cr:ZnS femtosecond laser with intrinsic nonlinear interferometry," Optica **6**, 126-127 (2019).

140. A. V. Pushkin, E. A. Migal, S. Tokita, Yu. V. Korostelin, and F. V. Potemkin, "Femtosecond graphene mode-locked Fe:ZnSe laser at 4.4 μm," Opt. Lett. **45**, 738-741 (2020).

141. E. Migal, A. Pushkin, B. Bravy, V. Gordienko, N. Minaev, A. Sirotkin, and F. Potemkin, "3.5-mJ 150-fs Fe:ZnSe hybrid mid-IR femtosecond laser at 4.4 μm for driving extreme nonlinear optics," Opt. Lett. **44**, 2550-2553 (2019).

142. A. Schliesser, N. Picque and T. W. Hansch, "Mid-infrared frequency combs," Nat. Phot. **6**, 440-449 (2012).

143. M. Pollnau and S. D. Jackson in *Topics in Applied Physics* Vol. **89** ed. By I. Sorokina and K. Vodopyanov (Springer, 2003) p. 219–255.

144. N. Coluccelli, A. Gambetta, D. Gatti, M. Marangoni, A. D. Lieto, M. Tonelli, G. Galzerano, and P. Laporta, "1.6-W self-referenced frequency comb at 2.06 μm using a Ho:YLF multipass amplifier," Opt. Lett. **36**, 299–2301 (2011).

145. F. Adler and S. A. Diddams, “High-power, hybrid Er:fiber/Tm:fiber frequency comb source in the 2 μm wavelength region,” Opt. Lett. **37**, 1400–1402 (2012).

146. A. V. Pushkin, E. A. Migal, H. Uehara, K. Goya, S. Tokita, M. P. Frolov, Yu. V. Korostelin, V. I. Kozlovsky, Ya. K. Skasyrsky, and F. V. Potemkin, “Compact, highly efficient, 2.1-W continuous-wave mid-infrared Fe:ZnSe coherent source, pumped by an Er:ZBLAN fiber laser,” Opt. Lett. **43**, 5941-5944 (2018).

147. C. C. Wang and G. W. Racette, “Measurement of Parametric Gain Accompanying Optical Difference Frequency Generation,” Appl. Phys. Lett. **6**, 169–171 (1965).

148. R. W. Boyd, Nonlinear Optics (Academic Press, San Diego, 1992).

149. G. Andriukaitis, T. Balčiūnas, S. Ališauskas, A. Pugžlys, A. Baltuška, T. Popmintchev, M.-C. Chen, M. M. Murnane, and H. C. Kapteyn, “90 GW peak power few-cycle mid-infrared pulses from an optical parametric amplifier,” Opt. Lett. **36**, 2755-2757 (2011).

150. R. Trebino and D. J. Kane, “Using phase retrieval to measure the intensity and phase of ultrashort pulses: frequency-resolved optical gating,” J. Opt. Soc. Am. A **10**, 1101-1111 (1993).

151. J. Lin, Y. Ma, R. Schwartz, D. Woodbury, J. A. Nees, M. Mathis, A. G. R. Thomas, K. Krushelnick, and H. Milchberg, “Adaptive control of laser-wakefield accelerators driven by mid-IR laser pulses,” Opt. Lett. **27**, 10912-10923 (2019).

152. S. V. Bulanov, D. V. Dylov, T. Zh. Esirkepov, F. F. Kamenets, D. V. Sokolov, Plasma Phys. Reports **31**, 369 (2005).

153. T. Nakamura, S. V. Bulanov, T. Z. Esirkepov, and M. Kando, “Ion acceleration in a dipole vortex in a laser plasma corona,” Phys. Rev. Lett. **105**, 135002 (2010).

154. M. Kalal, O. Slezak, M. Martinkova, and Y. J. Rhee, “Compact Design of a Nomarski Interferometer and Its Application in the Diagnostics of Coulomb Explosions of Deuterium Clusters,” J. Korean Phys. Soc. **56**, 287-294 (2010).

155. Y. Glinec, J. Faure, A. Guemnie-Tafo, V. Malka, H. Monard, J. P. Larbre, V. De Waele, J. L. Marignier, and M. Mostafavi, "Absolute calibration for a broad range single shot electron spectrometer," Rev. Sci. Instrum. **77**, 103301 (2006).

156. A. Buck, K. Zeil, A. Popp, K. Schmid, A. Jochmann, S. D. Kraft, B. Hidding, T. Kudyakov, C. M. S. Sears, L. Veisz, S. Karsch, J. Pawelke, R. Sauerbrey, T. Cowan, F. Krausz, and U. Schramm, "Absolute charge calibration of

scintillating screens for relativistic electron detection," Rev. Sci. Instrum. **81**, 033301 (2010).

157. M. A. Herráez, M. A. Gdeisat, D. R. Burton, and M. J. Lalor, "Robust, fast, and effective two-dimensional automatic phase unwrapping algorithm based on image decomposition," Appl. Opt. **41**, 7445-7455 (2002).

158. T. D. Arber, K. Bennett, C. S. Brady, A. Lawrence-Douglas, M. G. Ramsay, N. J. Sircombe, P. Gillies, R. G. Evans, H. Schmitz, A. R. Bell, and C. P. Ridgers, "Contemporary particle-in-cell approach to laser-plasma modelling," Plasma Phys. Control. Fusion **57**, 113001 (2015).

159. D. F. Gordon, "Improved Ponderomotive Guiding Center Algorithm," IEEE Trans. Plasma Sci. **35**, 1486 (2007)

160. R. A. Fonseca, L. O. Silva, F. S. Tsung, V. K. Decyk, W. Lu, C. Ren, W. B. Mori, S. Deng, S. Lee, T. Katsouleas, and J. C. Adam, "OSIRIS: A Three-Dimensional, Fully Relativistic Particle in Cell Code for Modeling Plasma Based Accelerators," in *International Conference on Computational Science* (Springer, 2002). p. 342-351.

161. C. Huang, V.K. Decyk, C. Ren, M. Zhou, W. Lu, W. B. Mori, J. H. Cooley, T. M. Antonsen, T. Katsouleas, "QUICKPIC: A highly efficient particle-in-cell code for modeling wakefield acceleration in plasmas," J. Comput. Phys. **217**, 658-679 (2006).

162. C. K. Birdsall, *Plasma Physics via Computer Simulation*, (Taylor and Francis, 2004).

163. M. Geissler, J. Schreiber, and J. Meyer-ter-Vehn, "Bubble acceleration of electrons with few-cycle laser pulses," New J. Phys. **8**, 186 (2006).

164. D. Guénot, D. Gustas, A. Vernier, B. Beaurepaire, F. Böhle, M. Bocoum, M. Lozano, A. Jullien, R. Lopez-Martens, A. Lifschitz, and J. Faure, "Relativistic electron beams driven by kHz single-cycle light pulses," Nat. Photonics **11**, 293 (2017).

165. J. Faure, D. Gustas, D. Guénot, A. Vernier, F. Böhle, M. Ouillé, S. Haessler, R. Lopez-Martens, and A. Lifschitz, "A review of recent progress on laser-plasma acceleration at kHz repetition rate," Plasma Phys. Control. Fusion **61**, 014012 (2019).

166. F. Salehi, M. Le, L. Pascale, and H. M. Milchberg, "Acceleration of low-divergence quasi-mono-energetic electron bunches to MeV-scale energies at 1 kHz with few-cycle laser pulses," YP10.00059, American Physical Society Division of Plasma Physics Meeting, Oct. 2019.

167. F. Salehi, “High Repetition Rate Laser-driven Electron Acceleration to Mega-electronvolt Energies,” PhD Dissertation, University of Maryland (2019).

168. A. F. Lifschitz and V. Malka, “Optical phase effects in electron wakefield acceleration using few-cycle laser pulses,” New J. Phys. **14**, 053045 (2012).

169. B. Beaurepaire, A. Lifschitz, and J. Faure, "Electron acceleration in sub-relativistic wakefields driven by few-cycle laser pulses," New J. Phys. **16**, 023023 (2014).

170. C. G. R. Geddes and Jessica L. Shaw, “Summary of Working Group 1: Laser-Plasma Wakefield Acceleration,” in *2018 IEEE Advanced Accelerator Concepts Workshop (AAC)* (IEEE, 2019).

171. A. Korolov, D. Woodbury, R. Schwartz, and H. M. Milchberg, "Quasi-monoenergetic Electron Beams from Mid-IR Laser Wakefield Acceleration in the Bubble Regime," OSA Frontiers in Optics Laser Science JW3A.5, Washington, D. C., September 2018.

172. P. Kumar, K. Yu, R. Zgadzaj, L. D. Amorim, M. C. Downer, J. Welch, V. N. Litvinenko, N. Vafaei-Najafabadi, and R. Samulyak, “Simulation study of CO2 laser-plasma interactions and self-modulated wakefield acceleration,” Phys. Plasmas **26**, 083106 (2109).

173. P. Musumeci, J. Giner Navarro, J.B. Rosenzweig, L. Cultrera, I. Bazarov, J. Maxson, S. Karkare, H. Padmore, "Advances in bright electron sources," Nuc. Inst. Meth. Phys. Res. A **907**, 209-220 (2018).

174. X. Wang and P. Musumeci, *Report of the Basic Energy Sciences Workshop on the Future of Electron Sources* (US Department of Energy, 2016). https://science.osti.gov/-/media/bes/pdf/reports/2017/Future_Electron_Source_Worskhop_Report.pdf.

175. K. P. Ziock, W. W. Craig, L. Farbis, R. C. Lanza, S. Gallagher, B. K. P. Horn, and N. W. Madden, “Large area imaging detector for long-range, passive detection of fissile material,” IEEE Trans. Nucl. Sci. **51**, 2238-2244 (2004).

176. M. V. Hynes, M. Toolin, B. Harris, J. McElroy, M. S. Wallace, L. J. Schultz, M. Galassi, A. Hoover, M. Mocko, D. Palmer, S. Tornga, D. Wakeford, H. R. Andrews, E. T. H. Clifford, L. Li, N. Bray, D. Locklin, R. Lanza, B. Horn, and D. Wehe, “The Raytheon-SORDS trimordal imager,” Proc. SPIE **7310,** 731003 (2009).

177. S. Zelakiewicz, R. Hoctor, A. Ivan, W. Ross, E. Nieters, W. Smith, D. McDevitt, M. Wittbrodt, and B. Milbrath, “SORIS—A standoff radiation imaging system,” Nucl. Instrum. Methods Phys. Res. A **652**, 5-9 (2011).

178. R. Pöllänen, H. Toivonen, K. Peräjärvi, T. Karhunen, T. Ilander, J. Lehtinen, K. Rintala, T. Katajainen, J. Niemelä, M. Juusela, "Radiation surveillance using an unmanned aerial vehicle," Appl. Radiat. Isot. **67**, 340-344 (2009).

179. X. B. Tang, J. Meng, P. Wang, Y. Cao, X. Huang, L. S. Wen, D. Chen, "Efficiency calibration and minimum detectable activity concentration of a real-time UAV airborne sensor system with two gamma spectrometers," Appl. Radiat. Isot. **110**, 100-108 (2016).

180. T. Hinterhofer, M. Pfennigbauer, A. Ullrich, D. Rothbacher, S. Schraml, M. Hofstätter, "UAV-based LiDAR and gamma probe with real-time data processing and downlink for survey of nuclear disaster locations," Proc. SPIE **10629**, 106290C (2018).

181. R.J. Nemzek, J.S. Dreicer, D.C. Torney, T.T. Warnock, "Distributed sensor networks for detection of mobile radioactive sources," IEEE Trans. Nucl. Sci. **51**, 1693-1700 (2004).

182. F. Ding, G. Song, K. Yin, J. Li, A. Song, "A GPS-enabled wireless sensor network for monitoring radioactive materials," Sens. Actuators A-Phys. **155**, 210-215 (2009).

183. J. R. Wachter and D. A. Cremers, "Determination of Uranium in Solution Using Laser-Induced Breakdown Spectroscopy," Appl. Spectrosc. **41**, 1042-1048 (1987).

184. J. P. Singh, F. Y. Yueh, H. Zhang, and K. P. Karney, "A preliminary study of the determination of uranium, plutonium and neptunium by laser-induced breakdown spectroscopy," Rec. Res. Dev. Appl. Spectrosc. **2**, 59-67 (1999).

185. J. P. Singh and S. N. Thakur, *Laser Induced Breakdown Spectroscopy* (Elsevier, 2007).

186. S. S. Nabiev and L. A. Palkina, "Current Trends in the Development of Remote Methods of Detecting Radioactive and Highly Toxic Substances," in *The Atmosphere and the Ionosphere*, ed. by V. L. Bychkov, G. V. Golubkov, and A. I. Nikitin (Springer, 2014).

187. J. M. Dai, X. F. Lu, J. Liu, I. C. Ho, N. Karpowicz, and X.-C. Zhang, "Remote THz Wave Sensing in Ambient Atmosphere," Terahertz Sci. Technol. **2**, 131-143 (2009).

188. Y. F. Su, R. G. Tonkyn, L. E. Sweet, J. F. Corbey, S. A. Bryan, and T. J. Johnson, "Characterization of uranium ore concentrate chemical composition via Raman spectroscopy," Proc. SPIE **10629**, 106290G (2018).

189. O. Katz, A. Natan, Y. Silberberg, S. Rosenwaks, “Standoff detection of trace amounts of solids by nonlinear Raman spectroscopy using shaped femtosecond pulses,” Appl. Phys. Lett. **92**, 171116 (2008).

190. A. S. Grishkanich, V. G. Bespalov, S. K. Vasiev, A. S. Gusarov, S. V. Kascheev, V. V. Elizarov, and A. P. Zhevlakov, “Monitoring radioactive contamination by hyperspectral lidar,” Proc. SPIE **9486**, 64890X (2015).

191. E. Puckrin and J. M. Thériault, “Passive standoff detection of radiological products by Fourier-transform infrared radiometry,” Opt. Lett. **29**, 1375-1377 (2004).

192. V. L. Granatstein and G. S. Nusinovich, “Detecting excess ionizing radiation by electromagnetic breakdown of air,” J. Appl. Phys. **108**, 063304 (2010).

193. P. Sprangle, B. Hafizi, H. M. Milchberg, G. Nusinovich, and A. Zigler, “Active remote detection of radioactivity based on electromagnetic signatures,” Phys. Plasmas **21**, 013103 (2014).

194. G. S. Nusinovich, P. Sprangle, C. A. Romero-Talamas, and V. L. Granatstein, “Range, resolution and power of THz systems for remote detection of concealed radioactive materials,” J. Appl. Phys. **109**, 083303 (2011).

195. Y. S. Dimant, G. S. Nusinovich, P. Sprangle, J. Penano, C. A. Romero-Talamas, and V. L. Granatstein, “Propagation of gamma rays and production of free electrons in air,” J. Appl. Phys. **112,** 083303 (2012).

196. G. S. Nusinovich, “Remote Detection of Concealed Radioactive Materials by Using Focused Powerful Terahertz Radiation,” J. Infrared Millim. Terahertz Waves **37**, 515-535 (2016).

197. M. L. Huertas, J. Fontan, and J. Gonzalez, “Evolution times of tropospheric negative ions,” Atmos. Environ. **12**, 2351-2362 (1967).

198. V. A. Mohnen, “Discussion of the formation of major positive and negative ions up to the 50 km level,” Pure Appl. Geophys. **84**, 141–151 (1971).

199. M. L. Huertas, J. Fontan, “Formation of stable positive and negative small ions of tropospheric interest,” Atmos. Environ. **16**, 2521–2527 (1982).

200. K. M. Ervin, I. Anusiewicz, P. Skurski, J. Simons, W. C. Lineberger, "The only stable state of O_2^- is the X $^2\Pi_g$ ground state and it (still!) has an adiabatic electron detachment energy of 0.45 eV," J. Phys. Chem. A **107**, 8521–8529 (2003)

201. National Institute of Standards and Technology; http://physics.nist.gov/PhysRefData/Star/Text/ASTAR.html.

202. W. P. Jesse, J. Sadauskis, Ionization in pure gases and the average energy to make an ion pair for alpha and beta particles. Phys. Rev. **97**, 1668–1670 (1955).

203. N. M. Kroll and K. M. Watson, "Multiphoton detachment of negative ions," DARPA Final Technical Report JSR-73-6 (1974).

204. J. C. Rienstra-Kiracofe, G. S. Tschumper, H. F. Schaefer III, S. Nandi, G. B. Ellison, "Atomic and molecular electron affinities: Photoelectron experiments and theoretical calculations." Chem. Rev. **102**, 231-282 (2002).

205. G. F. Gribakin and M. Yu. Kuchiev, "Multiphoton detachment of electrons from negative ions," Phys. Rev. A **55**, 3760-3771 (1997).

206. G. S. Nusinovich, F. Qiao, D. G. Kashyn, R. Pu, and L. S. Dolin. "Breakdown-prone volume in terahertz wave beams," J. Appl. Phys. **113**, 233303 (2013).

207. P. Polynkin and J. V. Moloney, "Optical breakdown of air triggered by femtosecond laser filaments," Appl. Phys. Lett. **99**, 151103 (2011).

208. V. V. Apollonov, L. M. Vasilyak, S. Yu. Kazantsev, I. G. Kononov, D. N. Polyakov, A. V. Saifulin, and K. N. Firsov, "Electric-discharge guiding by a continuous spark by focusing CO_2-laser radiation with a conic mirror," Quantum Electron. **32**, 115 (2002).

209. K. Mansour, M. J. Soileau, and E. W. Van Stryland, "Nonlinear optical properties of carbon-black suspensions," J. Opt. Soc. Am. B **9**, 1100-1109 (1992).

210. H. Tawara, N. Ishida, J. Kikuchi, and T. Doke, "Measurements of the *W* values in argon, nitrogen, and methane for 0.93 to 5.3 MeV alpha particles," Nuc. Instr. Meth. B **29,** 447-455 (1987).

211. A. W. Ali, "Electron Energy Loss Rates in N2, O2, and Air," NRL Memorandum Report 5400 (1984).

212. J. D. Huba, *NRL Plasma Formulary Supported by The Office of Naval Research* (Naval Research Laboratory, 2013).

213. J. Peñano, J. P. Palastro, B. Hafizi, M. H. Helle, and G. P. DiComo, "Self-channeling of high-power laser pulses through strong atmospheric turbulence," Phys. Rev. A **96**, 013829

214. M. H. Helle, G. DiComo, J. Palastro, J. Peñano, J. Elle, and A. Schmitt-Sody, "Nonlinear self-channeling of laser pulses through distributed atmospheric turbulence," in Frontiers in Optics 2017, OSA Technical Digest (online) (Optical Society of America, 2017), paper JTu3A.59.

215. G. P. DiComo, “Nonlinear self-channeling of high-power lasers through turbulent atmospheres,” Doctoral Dissertation, University of Maryland (2018).

216. A. M. Perelomov and V. S. Popov, "Ionization of atoms in an alternating electric field III," Sov. Phys. JETP **25,** 336 (1967).

217. M. V. Ammosov, N. B. Delone, and V. P. Krainov, "Tunnel ionization of complex atoms and of atomic ions in an altemating electromagnetic field," Sov. Phys. JETP **64,** 1191 (1986).

218. V. S. Popov, "Tunnel and multiphoton ionization of atoms and ions in a strong laser field (Keldysh theory)," Phys. Usp. **47,** 855 (2004).

219. S. L. Chin, F. Yergeau, and P. Lavigne, "Tunnel ionisation of Xe in an ultra-intense CO2 laser field (10^{14} W cm^{-2}) with multiple charge creation," J. Phys. B: At. Mol. Phys. **18,** L213 (1985).

220. S. Augst, D. D. Meyerhofer, D. Strickland, and S. L. Chin, "Laser ionization of noble gases by Coulomb-barrier suppression," J. Opt. Soc. Am. B **8,** 858 (1991).

221. A. Talebpour, J. Jang, and S. L. Chin, "Semi-empirical model for the rate of tunnel ionization of N_2 and O_2 molecule in an intense Ti: sapphire laser pulse," Opt. Commun. **163,** 29 (1999).

222. J. K. Wahlstrand, S. Zahedpour, A. Bahl, M. Kolesik, and H. M. Milchberg, Phys. Rev. Lett. **120,** 183901 (2018).

223. A. Sharma, M. N. Slipchenko, M. N. Shneider, X. Wang, K. A. Rahman, and A. Shashurin, Sci. Rep. **8,** 2874 (2018).

224. Y.-H. Chen, S. Varma, T. M. Antonsen, and H. M. Milchberg, "Direct measurement of the electron density of extended femtosecond laser pulse-induced filaments," Phys. Rev. Lett. **105**, 215005 (2010).

225. V. P. Drachev, Y. I. Krasnikov, and P. A. Bagryansky, "Dispersion interferometer for controlled fusion devices," Rev. Sci. Instr. **64**, 1010 (1993).

226. D. Abdollahpour, S. Suntsov, D. G. Papazoglou, and S. Tzortzakis, "Measuring easily electron plasma densities in gases produced by ultrashort lasers and filaments," Opt. Ex. **19**, 16866 (2011)

227. C. O. Laux, T. G. Spence, C. H. Kruger and R. N. Zare, "Optical diagnostics of atmospheric pressure air plasmas," Plasma Sources Sci. Technol. **12**, 125 (2003).

228. M. N. Shneider and R. B. Miles, "Microwave diagnostics of small plasma objects," J. Appl. Phys. **98,** 033301 (2005).

229. V. Shumakova, S. Ališauskas, P. Malevich, C. Gollner, A. Baltuška, D. Kartashov, A. M. Zheltikov, A. V. Mitrofanov, A. A. Voronin, D. A. Sidorov-Biryukov, and A. Pugžlys, "Filamentation of mid-IR pulses in ambient air in the vicinity of molecular resonances," Opt. Lett. **43** 2185-2188 (2019).

230. H. C. van de Hulst, *Light Scattering by Small Particles* (Dover, 1981).

231. A. V. Phelps and L. C. Pitchford, "Anisotropic scattering of electrons by N_2 and its effect on electron transport," Phys. Rev. A **31**, 2932-2949 (1985).

232. B. C. Stuart, M. D. Feit, S. Herman, A. M. Rubenchik, B. W. Shore, and M. D. Perry. "Nanosecond-to-femtosecond laser-induced breakdown in dielectrics," Phys. Rev. B **53**, 1749-1761 (1996).

233. A. B. Langdon, "Nonlinear Inverse Bremsstrahlung and Heated-Electron Distributions," Phys. Rev. Lett. **44**, 575-579 (1980).

234. J. M. Liu, J. S. De Groot, J. P. Matte, T. W. Johnston, and R. P. Drake, "Measurements of inverse bremsstrahlung absorption and non-Maxwellian electron velocity distributions," Phys. Rev. Lett. **72**, 2717-2720 (1994).

235. A. L. Milder, et al., "Evolution of the Electron Distribution Function in the Presence of Inverse Bremsstrahlung Heating and Collisional Ionization," Phys. Rev. Lett. **124**, 025001 (2020).

236. E. M. Wright, S. W. Koch, M. Kolesik, and J. V. Moloney, "Memory effects in the long-wave infrared avalanche ionization of gases: A review of recent progress," Rep. Prog. Phys. **82,** 064401 (2019).

237. X. Gao and B. Shim, "Impact-ionization mediated self-focusing of long-wavelength infrared pulses in gases," Opt. Lett. **44**, 827-830 (2019).

238. P. Felsenthal and J. M. Proud, "Nanosecond-pulse breakdown in gases," Phys. Rev. **139**, A1796-A1804 (1965).

239. Y. Itikawa, *Molecular processes in Plasmas* (Springer, 2007).

240. K. Y. Kim, I. Alexeev, E. Parra, and H. M. Milchberg, "Time-Resolved Explosion of Intense-Laser-Heated Clusters," Phys. Rev. Lett. **90,** 023401 (2003).

241. L. Morawska, A. Afshari, G. N. Bae, G. Buonanno, C. Y. H. Chao, O. Hänninen, W. Hofmann, C. Isaxon, E. R. Jayaratne, P. Pasanen, T. Salthammer, M. Waring, and A. Wierzbicka, "Indoor aerosols: from personal exposure to risk assessment," Indoor Air **23**, 462-487 (2013).

242. S. J. Chen, T. C. Lin, J. H. Tsai, L. T. Hsieh, and J. Y. Cho, "Characteristics of Indoor Aerosols in College Laboratories, "Characteristics of Indoor

Aerosols in College Laboratories," Aerosol Air Qual. Res. **13**, 649-661 (2013).

243. A. F. Vette, A. W. Rea, P. A. Lawless, C. E. Rodes, G. Evans, V. R. Highsmith, and L. Sheldon, "Characterization of Indoor-Outdoor Aerosol Concentration Relationships during the Fresno PM Exposure Studies," Aerosol Sci. Tech. **42**, 118-126 (2019).

244. S. Zahedpour, S. W. Hancock, AND H. M. Milchberg, "Ultrashort infrared 2.5–11 μm pulses: spatiotemporal profiles and absolute nonlinear response of air constituents," Opt. Lett. **44**, 843-846 (2019).

245. J. J. Pigeon, S. Y. Tochitsky, E. C. Welch, and C. Joshi, "Measurements of the nonlinear refractive index of air, N_2 and O_2 at 10 μm using four-wave mixing," Opt. Lett. **41**, 3924–3927 (2016).

246. M. Kolesik and J. V. Moloney, "Nonlinear optical pulse propagation simulation: from Maxwell's to unidirectional equations," Phys. Rev. E **70**, 036604 (2004).

247. D. Arnold, E. Cartier, and D. J. DiMaria, "Acoustic-phonon runaway and impact ionization by hot electrons in silicon dioxide," Phys. Rev. A **45**, 1477-1480 (1992).

248. F. Brunel, "Not-so-resonant, resonant absorption," Phys. Rev. Lett. **59**, 52-55 (1987).

249. M. S. Sherwin, C. A. Schmuttenmaer, and P. H. Bucksbaum, DOE-NSF-NIH Workshop on Opportunities in THz Science (http://www.er.doe.gov/bes/reports/files/THz_rpt.pdf).

250. M. Clerici, M. Peccianti, B. E. Schmidt, L. Caspani, M. Shalaby, M. Giguère, A. Lotti, A. Couairon, F. Légaré, T. Ozaki, D. Faccio, and R. Morandotti, "Wavelength Scaling of Terahertz Generation by Gas Ionization" Phys. Rev. Lett. **110**, 253901 (2013).

251. F. Brunel, "Harmonic generation due to plasma effects in a gas undergoing multiphoton ionization in the high-intensity limit," J. Opt. Soc. Am. B **7**, 521-526 (1990).

252. C. Vicario, B. Monoszlai, and C. P. Hauri, "GV/m Single-Cycle Terahertz Fields from a Laser-Driven Large-Size Partitioned Organic Crystal," Phys. Rev. Lett. **112**, 213901 (2014).

253. Z. Nie, C. H. Pai, J. Hua, C. Zhang, Y. Wu, Y. Wan, F. Li, J. Zhang, Z. Cheng, Q. Su, S. Liu, Y. Ma, X. Ning, Y. He, W. Lu, H. H. Chu, J. Wang, W. B Mori, and C. Joshi, "Relativistic single-cycle tunable infrared pulses

generated from a tailored plasma density structure," Nat. Phot. **8**, 489-494 (2018).

254. C. D'Amico, A. Houard, S. Akturk, Y. Liu, J. L. Bloas, M. Franco, B. Prade, A. Couairon, V. T. Tikhonchuk, and A. Mysyrowicz, "Forward THz radiation emission by femtosecond filamentation in gases: theory and experiment," New J. Phys. **10**, 013015 (2008).

255. A. Englesbe, J. Elle, R. Reid, A. Lucero, H. Pohle, M. Domonkos, S. Kalmykov, K. Krushelnick, and A. Schmitt-Sody, Opt. Lett. **43**, 4953 (2018).

256. T. Garrett, "Generation of RF Radiation by Femtosecond Atmospheric Filaments," Presentation TO7.00015, American Physical Society Division of Plasma Physics Meeting, Oct. 2019.